



OMAR YESID DURAN TRIANA

**NUMERICAL APPROXIMATION OF
RESERVOIR FAULT STABILITY WITH LINEAR
POROELASTICITY**

***APROXIMAÇÃO NUMÉRICA DO PROBLEMA
DE REATIVAÇÃO DE FALHA USANDO
POROELASTICIDADE LINEAR***

**CAMPINAS
2013**



UNIVERSIDADE ESTADUAL DE CAMPINAS
FACULDADE DE ENGENHARIA MECÂNICA
E INSTITUTO DE GEOCIÊNCIAS

OMAR YESID DURAN TRIANA

**NUMERICAL APPROXIMATION OF
RESERVOIR FAULT STABILITY WITH LINEAR
POROELASTICITY**

Supervisor/*Orientador*: Prof. Dr. Philippe Remy Bernard Devloo

***APROXIMAÇÃO NUMÉRICA DO PROBLEMA
DE REATIVAÇÃO DE FALHA USANDO
POROELASTICIDADE LINEAR***

Dissertação de Mestrado apresentada ao Programa de Pós-Graduação em Ciências e Engenharia de Petróleo da Faculdade de Engenharia Mecânica e Instituto de Geociências da Universidade Estadual de Campinas para obtenção do título de Mestre em Ciências e Engenharia de Petróleo na área de Exploração.

MSc Dissertation presented to the Post Graduate Program of the Science and Petroleum Engineering at Mechanical Engineering Faculty and Geosciences Institute of the University of Campinas to obtain a Master's degree in Science and Petroleum Engineering. Area: Petroleum Exploitation.

Este exemplar corresponde à versão final da
Dissertação defendida pelo aluno Omar Yesid
Duran Triana, sob orientação do Prof. Dr.
Philippe Remy Bernard Devloo.

Súpervisor / *Orientador*

CAMPINAS
2013

Ficha catalográfica
Universidade Estadual de Campinas
Biblioteca da Área de Engenharia e Arquitetura
Rose Meire da Silva - CRB 8/5974

D931a Duran Triana, Omar Yesid, 1986-
Aproximação numérica do problema de reativação de falha usando
poroelasticidade linear / Omar Yesid Duran Triana. – Campinas, SP : [s.n.], 2013.

Orientador: Philippe Remy Bernard Devloo.
Dissertação (mestrado) – Universidade Estadual de Campinas, Faculdade de
Engenharia Mecânica e Instituto de Geociências.

1. Poroelasticidade. 2. Método de elementos finitos. 3. Galerkin, Métodos de.
4. Falhas (Geologia). I. Devloo, Philippe Remy Bernard, 1958-. II. Universidade
Estadual de Campinas. Faculdade de Engenharia Mecânica. III. Título.

Informações para Biblioteca Digital

Título em outro idioma: Numerical approximation of reservoir fault stability with linear
poroelasticity

Palavras-chave em inglês:

Poroelasticity

Finite Element Method

Galerkin Method

Faults (Geology)

Área de concentração: Exploração

Titulação: Mestre em Ciências e Engenharia de Petróleo

Banca examinadora:

Philippe Remy Bernard Devloo [Orientador]

Denis José Schiozer

Ramiro Brito Willmersdorf

Data de defesa: 28-02-2013

Programa de Pós-Graduação: Ciências e Engenharia de Petróleo



UNIVERSIDADE ESTADUAL DE CAMPINAS
FACULDADE DE ENGENHARIA MECÂNICA
E INSTITUTO DE GEOCIÊNCIAS

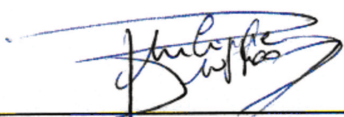
DISSERTAÇÃO DE MESTRADO ACADÊMICO

NUMERICAL APPROXIMATION OF RESERVOIR FAULT STABILITY WITH LINEAR POROELASTICITY

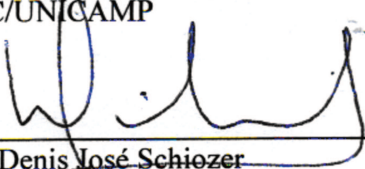
Author/*Autor*: Omar Yesid Duran Triana

Supervisor/*Orientador*: Prof. Dr. Philippe Remy Bernard Devloo

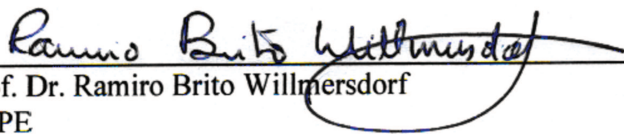
A banca examinadora composta pelos membros abaixo aprovou esta dissertação



Prof. Dr. Prof. Dr. Philippe Remy Bernard Devloo, Presidente
DES/FEC/UNICAMP



Prof. Dr. Denis José Schiozer
DEP/FEM/UNICAMP



Prof. Dr. Ramiro Brito Willmersdorf
UFPE

Campinas, 28 de fevereiro de 2013

To my Family.

*If I have seen farther than others, it
is because I stood on the shoulders of
giants.*

— SIR ISAAC NEWTON

Acknowledgements

At this place I would also like to thank a number of people for their support to this research:

- I thank my advisor Philippe for the opportunity to carry out this challenging Master's degree at Unicamp university. I am especially thankful for his support, friendship, encouragement and his incredible intellectual capability to answer different kind of questions during these great years. Sincerely you are a life example to be followed.
- I also want to thank my LabMeC colleagues: Applied mathematicians: Sônia Gomes, Agnaldo Farias, Jorge Calle, João Gonçalves, Denise de Siqueira; Computer scientist: Raul Baldin and Civil engineers: Cesar Lucci, Diogo Lira Cecilio and Nathan Shauer for his support, encouragement, interest, friendship and shared feeling for computational methods and science.
- I also want to thank:
- Labmec, CEP, DEP.
- Cenpes, Petrobras.
- Anp.

Abstract

Fault reactivation resulting from pore pressure changes may be accompanied by seismic activity, subsidence, well damage and the creation of fluid leakage paths. To ensure acceptable reservoir performance in hydrocarbon production, it is critical to assess the reactivation tendencies of existing faults. In this work, a numerical approximation is presented that allows quasi-static deformation coupled with monophasic flow considering compressible constituents. Two dimensional modeling is carried out using the theory of linear poroelasticity and a new treatment of poroelastic equations defined into a multi-physics data structure. Dimensionless forms of poroelasticity equations are presented and several analytic and semi analytic solutions, as well as poroelastic inclusion theory were reproduced with the proposed implementation in order to validate it. The computational model is used to evaluate the stress changes around and into the reservoir in order to assess the fault reactivation tendency at different scenarios. Fault reactivation tendency resulting from induced stress changes was calculated using the Coulomb failure stress change method for definition of the shear slip potential along pre-existing faults at one specific time associated to pore pressure change. It was found that fault reactivation tendency depends on the reservoir geometry, poroelastic properties of the reservoir and surrounding rocks, reservoir geometry, static friction coefficient, and pore pressure distribution. A numerical study about the accuracy of surrounding material dimensions is presented and several scenarios with different depletion programs were evaluated to determine the influence of the production rates over fault reactivation tendency.

Keywords: Poroelasticity, Finite Element Method, Galerkin Method, Faults (Geology).

Resumo

A reativação de falhas, resultante de variações na pressão de poros, pode ocasionar atividades sísmicas, subsidência, dano nos poços e criação de caminhos de escape dos fluidos contidos nos reservatórios. Para se garantir uma produção de hidrocarbonetos eficiente, mostra-se um fator crítico a avaliação das tendências de reativação das falhas existentes no meio poroso. Neste trabalho, apresenta-se uma aproximação numérica para uma análise de deformação quase-estática com escoamento monofásico, considerando a compressibilidade da rocha e dos fluidos. Um modelo bidimensional foi empregado considerando a teoria de poroelasticidade linear e um novo tratamento da poroelasticidade através de estruturas de dados multifísicos. Formas adimensionais das equações de poroelasticidade são apresentadas, juntamente com a reprodução de diversas soluções analíticas e semi-analíticas das mesmas em semiespaços, com o propósito de se validar o algoritmo desenvolvido. O modelo computacional foi utilizado para avaliar as mudanças de tensão, no reservatório e em suas fronteiras, com o objetivo de se estudar as tendências reativação de falhas em diferentes cenários. As tendências de reativação de falhas, resultantes da indução de variações de tensão na rocha, foram calculadas através do método de variação de tensão de ruptura de Coulomb para a definição das seções com potencial de deslocamento por tensões cisalhante das falhas pre-existentes em tempos específicos, associados com as alterações na pressão de poros. Mostrou-se que a reativação de falhas depende da geometria de reservatório, das propriedades poroelásticas da rocha, coeficiente de atrito e a distribuição da pressão de poros. Um estudo sobre precisão dos cálculos baseado na dimensão do material circundante é apresentada e vários cenários com diferentes programas depleção foram avaliados para determinar a influência das taxas de produção sobre a tendência de reativação das falhas.

Palavras-chave: Poroelasticidade, Método de Elementos Finitos, Galerkin, Métodos de, Falhas (Geologia).

Contents

1	Introduction	1
1.1	Research motivation	1
1.2	Literature review	2
1.2.1	Poroelasticity in reservoir engineering	2
1.2.2	Induced seismicity	2
1.2.3	Continuous Galerkin (CG) method	10
1.3	Research objectives	11
1.4	Outline of dissertation	12
2	Theoretical concepts	13
2.1	Small deformations in porous media	13
2.2	Poroelastic formulation	14
2.2.1	Main assumptions	14
2.2.2	Fluid potential and excess pore pressure	16
2.2.3	Darcy’s law	17
2.2.4	Strong formulation	22
2.2.5	Dimensionless Strong Formulation	24
2.3	Fault Reactivation according to the inclusion theory	26
2.3.1	Main assumptions	27
2.3.2	Theoretical concepts	28
2.3.3	Assessment of fault reactivation	30
2.4	Summary	32
3	Continuous Galerkin Formulation	33
3.1	Weak Formulation	33
3.2	Variational formulation	35
3.2.1	Mass conservation equation	35

3.2.2	Equilibrium Equation	37
3.3	Bilinear Forms	38
3.4	Spatial discretization	39
3.5	Time discretization	42
3.6	Summary	44
4	Implementation and validation	45
4.1	Implementation	45
4.2	Computational Tests	52
4.3	Step load applied to an elastic half space	52
4.4	Mass source injection into a bounded infinite poroelastic medium	62
4.5	Summary	68
5	Fault reactivation	69
5.1	The rectangular reservoir problem	69
5.1.1	Fault reactivation threshold	78
5.1.2	Side burden dimensions	79
5.1.3	Friction coefficient variation	82
5.1.4	Material contrast	82
5.1.5	Tilted reservoir	85
5.1.6	Reservoir geometry	85
5.2	Reservoir with non-constant pressure distribution	85
5.2.1	Reservoir depletion due to one well	85
5.2.2	Reservoir depletion due to injection-production scheme	91
5.3	Summary	98
6	Discussion	99
6.1	Main results	99
6.2	Conclusions	99
6.3	Recommendations for future work	100
A	Dimensionless forms	109
A.1	Computation of dimensionless forms	109
B	Contribute Method	113
B.1	Poroelastic Contribute Method	113
C	GID Mat Template	119
C.1	GID Mat Template	119

List of Figures

1.1	Fault reactivation problem divided in two parts. Upper) Initial problem. Lower) Perturbation problem. Fault inclination θ , and green zones represent reactivated part of fault planes. Source: redraw from Wang (2000).	6
2.1	Definition of excess pore pressure as decomposed total pressure referred to hydrostatic pressure. Source: redraw from Wang (2000).	17
4.1	Schematic flow of data computations and class interactions.	48
4.2	Embedded domain by overlapping areas. Left) Diffusion domain that contains all geometric information and computational information for flow calculations, Right) Elastic domain that contains all geometric information and computational information for elasticity.	49
4.3	Multi-physics view of the poroelastic problem. All the information of each computational element that represent one physical problem is stored and processed by multiphysics elements as the poroelastic elements represented by <i>TPZPoroElastic2d</i> . Left) Computational Elasticity Mesh. Right) Computational Diffusion Mesh.	50
4.4	Geometry generated in GID and its corresponding geometric mesh.	51
4.5	General work flow to solve poroelasticity equations.	52
4.6	Step load applied to a poroelastic half space. Left) Boundary conditions for the poroelastic column. Geometric Mesh with associated materials identifiers (Colors), the blue one (number 1) represents the poroelastic column and the others, the boundary conditions. Center) Mesh for finite poroelastic column, Right) Mesh for Infinite poroelastic column. Source: redraw from Wang (2000).	53
4.7	Dimensionless displacement y direction for semi-infinite column at different dimensionless times. Plot line $((0, 0), (0, -10.0))$. Points represent the numerical solution.	55

4.8	Dimensionless excess pore pressure for semi-infinite column at different dimensionless times. Plot line $((0,0),(0,-10.0))$. Points represent the numerical solution.	56
4.9	Dimensionless displacement y direction for finite column at different dimensionless times along the plot line $((0,0),(0,-1.0))$. Points represent the numerical solution.	57
4.10	Dimensionless excess pore pressure for finite column at different dimensionless times along the plot line $((0,0),(0,-1.0))$. Points represent the numerical solution.	57
4.11	Dimensionless excess pore pressure for finite and semi-infinite columns at $t_D = 0.2$. Plot line $((0,0),(0,-1.0))$	58
4.12	Poroeleastic response of finite column along $0 < y_D < 0.2$ case with incompressible constituents at 10 time steps.	58
4.13	Error norm for excess pore pressure vs different time steps with different time schemes $\xi = \{0.5, 0.6667, 1.0\}$	59
4.14	Error norm for displacement in y direction vs different time steps with different time schemes $\xi = \{0.5, 0.6667, 1.0\}$	60
4.15	Error norm for excess pore pressure vs number of DOF with different refinement levels 0, 1, 2, 3.	60
4.16	Error norm for displacement in y direction vs number of DOF with different refinement levels 0, 1, 2, 3.	61
4.17	Error norm for excess pore pressure vs number of DOF with different polynomial orders $((r^1 = 2, r^2 = 1), r^1 = 3, r^2 = 2), r^1 = 4, r^2 = 3), r^1 = 5, r^2 = 4))$	61
4.18	Error norm for displacement in y direction vs number of DOF with different polynomial orders $((r^1 = 2, r^2 = 1), r^1 = 3, r^2 = 2), r^1 = 4, r^2 = 3), r^1 = 5, r^2 = 4))$	62
4.19	Schematic representation of line mass source.	63
4.20	Geometric mesh with directional refinement at line source. Below) Table shows dimensionless variables corresponding to values in table 4.2.	64
4.21	Dimensionless P_D^{ex} , σ_{Dx} , and σ_{Dy} at $t_D = 0.1$. Plot line $((0,0),(0.2,0))$	66
4.22	\mathbf{u}_D near to injection point at $t_D = 0.1$. Plot line $((1,0),(0,1))$	66
4.23	\mathbf{u}_D far from injection point u_{Dx} at $t_D = 0.1$. $((50,0),(0,50))$	66
4.24	PSC ratio at $t_D = 0.1$. Plot line $((0,0),(1,0))$	67
4.25	PSC ratio at long times $t_D = 10$. Plot line $((0,0),(1,0))$	67
5.1	Rectangular reservoir inclusion and boundary conditions.	69
5.2	Rectangular reservoir geometric mesh.	70

5.3	Arching ratios obtained from arbitrary initial state compared with the zero initial state calculations. Arching ratios normalized by $\frac{(1-2\nu)}{(1-\nu)}$	71
5.4	Horizontal arching ratio for rectangular reservoir computed with LPA. Arching ratio normalized by $\frac{(1-2\nu)}{(1-\nu)}$	72
5.5	Vertical arching ratio for rectangular reservoir computed with LPA. Arching ratio normalized by $\frac{(1-2\nu)}{(1-\nu)}$	72
5.6	Shear arching ratio for rectangular reservoir computed with LPA. Arching ratio normalized by $\frac{(1-2\nu)}{(1-\nu)}$	73
5.7	σ_x contour for rectangular reservoir geometry using STARS. Visualization with Results 3D.	74
5.8	γ_x, γ_y STARS solution comparison with LPA and Hawkes (2009) solution. Plot line ((0,0),(0,-2)).	75
5.9	γ_x, γ_y STARS solution comparison with LPA and Hawkes (2009) solution. Plot line ((-0.5,-1),(0.5,-1)).	75
5.10	Fault reactivation factor for rectangular reservoir geometry, faults inclined 60 degrees. Bottom) λ_{FR} for far offset faults along fault planes. Arching ratio normalized by $\frac{(1-2\nu)}{(1-\nu)}$	76
5.11	λ_{FR} along fault planes. Top) Fault at offset 0. Bottom) Fault at offset 1. λ_{FR} normalized by $\frac{(1-2\nu)}{(1-\nu)}$, ($\lambda_{FR} < 0$ tendency to reactivate).	77
5.12	λ_{FR} along reservoir extension. λ_{FR} normalized by $\frac{(1-2\nu)}{(1-\nu)}$, ($\lambda_{FR} < 0$ tendency to reactivate).	78
5.13	u_{Dy}, u_{Dx} dimensionless displacement as function of dimensionless depth and lateral extension. Plot line ((0,0)(0,20)).	80
5.14	γ_x, γ_y arching ratios comparison with LPA reference solution (Black line in table 5.2). Plot line ((-2,-2)(2,-2)).	80
5.15	γ_x, γ_y lines for different hosting material sizes with $\nu \approx 0.3$	81
5.16	μ_s friction variation effect in zero λ_{FR} contour. Fault reactivation factor normalized by $\frac{(1-2\nu)}{(1-\nu)}$	82
5.17	Stiffness effect on λ_{FR} . Top) Soft side burden. Bottom) Rigid side burden. Values normalized by $\frac{(1-2\nu)}{(1-\nu)}$	83
5.18	Reservoir inclination (45 degrees) effect on λ_{FR} . Fault reactivation factor normalized by $\frac{(1-2\nu)}{(1-\nu)}$	84
5.19	Anticline reservoir geometry effect on λ_{FR} . Fault reactivation factor normalized by $\frac{(1-2\nu)}{(1-\nu)}$	84
5.20	λ_{FR} for early times of unitary production at dimensionless time of $t_D = 0.06$. Bottom) Near offset fault planes. Well location at offset 0.	86
5.21	λ_{FR} for long times of unitary production, dimensionless time of $t_D = 0.09$. Bottom) Near offset faults planes. Well location at offset 0.	87

5.22	λ_{FR} for early times of unitary production at dimensionless time of $t_D = 0.06$. Bottom) Near offset fault planes. Well location at offset -0.4	88
5.23	λ_{FR} for long times of unitary production at dimensionless time of $t_D = 0.2$. Bottom) Near offset fault planes. Well location at offset -0.4	89
5.24	Production strategy to analyze the effect of depletion. Left) case 1. Right) case 2.	91
5.25	λ_{FR} contours at different dimensionless times. Top) $t_D = 0.01$. Bottom) $t_D = 0.02$	93
5.26	λ_{FR} for near offset faults at different dimensionless times. Top) $t_D = 0.01$. Bottom) $t_D = 0.02$	94
5.27	λ_{FR} for fault at offset 0 at different dimensionless times. Top) $t_D = 0.5$. Bottom) $t_D = 0.08$	95
5.28	$\lambda_{FR} = -0.4$ contour at different dimensionless times. Top) $t_D = 0.08$. Bottom) $t_D = 0.09$	96
5.29	λ_{FR} for near offset faults at different dimensionless times. Top) $t_D = 0.08$. Bottom) $t_D = 0.09$	97

List of Tables

2.1	Group of dimensionless variables. Left) Incompressible fluid constituent case. Right) Compressible fluid constituent case.	25
2.2	Fault reactivation tendency sign convention. Opposite case tendency to stabilization. Left) Used for normalized arching ratios (Hawkes, 2009; Germanovich, 2004). Right) Direct form of ΔCFS . Used for LPA computations. In both cases τ sign is inverted for reverse faulting.	31
3.1	Time schemes summarized in terms of different ξ values. Source: Wynne (2000).	43
4.1	Group of dimensionless variables for step load in semi-infinite poroelastic solid.	54
4.2	Model parameters for line mass source solution (Rudnicki, 1986). SI units.	65
5.1	Parameters for rectangular reservoir and side rocks with similar elastic moduli. All these parameters are in SI units. The model geometry has been normalized by R_D	71
5.2	Spatial ratios for different side burden dimensions with $\nu \approx 0.3$	79
5.3	Model parameters for one well production scheme. SI units.	90
5.4	Model parameters for injection/production scheme. SI units.	92
5.5	Model parameters for injection on flanks and production on middle region. SI units.	92
A.1	Step Load one dimensional consolidation matrices. MP matrix of rank 3, P , S set of principal and secondary variables.	110
A.2	Step Load one dimensional consolidation relationship matrix R and definitions of dimensionless group of variables.	110

List of Symbols

α	Biot's (1941) coefficient	20
$\bar{\mathbf{v}}_f$	Darcy average velocity of fluid phase (m s^{-1})	17
$\bar{\sigma}$	Rock compressibility (Pa)	20
\circ	Means reference state. X_\circ indicates references state of X	20
η	Dynamic fluid viscosity (Pa s)	17
γ	Normalized stress arching ratio	30
κ	Diagonal absolute permeability tensor (m^2)	17
λ	First Lamé parameter (Pa)	20
λ_{FR}	Fault reactivation factor	31
λ_u	Undrained first Lamé parameter (Pa)	23
\mathbf{u}	Average displacement of the solid phase (m)	15
\mathbf{v}_f	Interstitial fluid phase velocity (m s^{-1})	15
μ	Second Lamé parameter (Pa)	20
μ_s	Coefficient of friction in the fault plane	30
ϕ	Rock porosity	15
ϕ^*	fluid fraction, also called fluid mass content	19
Φ_H	Hubbert fluid potential (m)	16

ρ_f	Fluid density (kg/m ³)	15
ρ_{solid}	Solid density (kg/m ³)	15
σ	Effective stress (Pa)	30
σ	Total stress (Pa)	23
σ_n	Effective normal stress on the fault plane (Pa)	30
σ_t	Total stress (Pa)	23
τ	Shear stress on the fault plane (Pa)	30
ε_v	Volumetric solid deformation	19
c	Hydraulic diffusivity (m ² /s)	23
C_b	Bulk compressibility (Pa ⁻¹)	21
C_r	Rock compressibility (Pa ⁻¹)	20
C_s	Matrix compressibility (Pa ⁻¹)	21
D	Absolute depth (m)	16
K_b	Bulk modulus of solid matrix with fluid (Pa)	20
K_s	Bulk modulus of solid matrix (Pa)	20
K_u	Undrained bulk modulus of solid matrix (Pa)	30
M	Biot constant (Pa)	21
m_f	Fluid mass (kg)	15
m_{solid}	Solid mass (kg)	15
P^{ex}	Excess pore pressure (Pa)	15
S_e	Storage coefficient (Pa ⁻¹)	23
t	Time (s)	15
V_{vol}	An arbitrary elementary volume (m ³)	15
Z	Depth reference (m)	16
Z_{datum}	Depth datum (m)	16

1. Introduction

1.1 Research motivation

Porous media like rocks are solid skeletons containing pores connected and filled with fluids in different phases (gas, oil and water). The deformation of the solid matrix and the flow of fluids are intrinsically coupled; for practical purposes, it can be neglected, but the manifestation of the pore pressure effect of solid deformation made it an important phenomenon in a number of engineering situations. A good grasp of this physical mechanism can equip engineers with the necessary insight to diagnose the poroelastic effect for their problems on hand. In general, the diffusion of fluid pressure is followed by the deformation of the porous rock and is a time-dependent process. The mathematical theory of linear poroelasticity was first established by Terzaghi (1943) and Biot (1941). From this time forth, poroelasticity has had many important applications in different areas: petroleum engineering, civil engineering and biomedical engineering. Specifically in petroleum engineering, the effective management of underground fluid extraction relies on the trustworthy evaluation of the subsidence of the ground surface, fault reactivation, well damage and the creation of fluid leakage paths in the recent applications. However, linear poroelastic problems that can be solved analytically are limited due to the complex coupled nature of the problem. In particular for reservoir fault reactivation, several analytical and semi-analytical approaches have been developed with several limitations and ideal assumptions.

In practical applications, generally, we have to seek numerical solutions as tools for solving this kind of problems. In the numerical approximation of geomechanical consolidation, the most popular numerical method is the continuous Galerkin (CG) finite element method in particular in commercial finite element packages. In this work, a non-commercial implementation oriented to solve fault reactivation problems by means of the inclusion theory in linear poroelasticity is developed. Consequently, it can be used to model problems with very complex geometries, material contrast, as well as it can exploit the advantages of numerical approximations.

1.2 Literature review

1.2.1 Poroelasticity in reservoir engineering

Muskat, in the 1930's, considered storage effects resulting primarily from fluid expansion and assumed that rocks were considered as an incompressible material at reservoir depths. Fluid expansion, however, could not explain the extra production in the East Texas Oil Field. He deemed the high production to be due to highly compressible gas or water drive mechanism from the reservoir peripheries. Jacob (1940) suggested alternatively that the high production rate was due to the compressibility of sand and clays. Initially, poroelasticity was used in petroleum engineering to understand subsidence, estimate hydrocarbon volumes and predict stresses around boreholes. The subsidence of Goose Creek oil field described by Pratt (1926) was the first conceptual realization of the coupling between large volumes of fluid extraction and large scale mechanical deformation. Since the problem of large groundwater withdrawals from aquifers is identical, Geertsma, who was affiliated with Shell in the Netherlands, studied the effect of pore fluid decline on volumetric changes of rocks (Geertsma, 1957). The groundwater subsidence literature in the 1970's used analytical and numerical techniques introduced by Geertsma and most recently used by Segall to connect hydrocarbon extraction with induced seismicity (Segall, 1987). Poroelasticity research in the 1940's and 1950's was oriented primarily toward rock mechanics. Hughes (1953) made laboratory measurements of pore compressibilities to correct the available pore space at reservoir conditions. Poroelasticity research continues in petroleum engineering and geophysics in the use of hydraulic fracturing as a technique for measuring earth stresses, geomechanical behavior of reservoirs and its interactions with side-burden rocks, faults, and another structural elements (Germanovich, 2004).

1.2.2 Induced seismicity

Injection induced seismicity

Currently, it is widely accepted that fluid injection into the subsurface environment does induce seismicity, in other words the fluid injection can trigger small earthquakes that evidence the induced seismicity (*i.e.*, the in-situ stress changes along an existing fault or fracture of an extremely low seismic magnitude). The most well-known example of injection-induced seismicity is probably given by the earthquakes triggered by fluid injection at the Rocky Mountain Arsenal (RMA), northeast of Denver, Colorado in 1967 (Hsieh and Bredehoeft, 1981). The U.S. Army Corps of Engineers drilled deep injection wells at RMA in 1962 for disposal of contaminated waste water. Waste fluid was injected into a

fractured reservoir in the Precambrian bedrock below the RMA between 1962 and 1966. During this 4-year period, a total of 625 million of liters of waste fluid were disposed off in the wells. Shortly after the injection of fluids started, small earthquakes were detected in the Denver area. There was an apparent correlation between the volume of fluid injected into the well and the number of earthquakes generated. In 1967, one year after the fluid injection was interrupted, there were three major earthquakes in the Denver area. This was attributed to the migration of the pressure front developed (Hsieh and Bredehoeft, 1981). After 1967, the number of earthquakes began to decline and by the 1980's, the swarm of seismic activity had virtually disappeared.

Another example of experimentation with fluid injection-induced seismicity is given by the German Continental Deep Drilling Program (KTB), which was designed to increase the knowledge of crustal stresses based on borehole measurements and to directly test the frictional equilibrium hypothesis by evaluating whether relatively small pore pressure perturbations could trigger micro-earthquakes (Zoback and Harjes, 1997). The injection of 200 m³ of *KBr/KCl* brine into a 70 m open-hole section at the bottom of the 9.1 km main borehole induced almost 400 micro-earthquakes at an average depth of 8.8 km. Most of the earthquakes were determined to be strike-slip events by focal plane mechanisms and had a NNW trending, essentially parallel to the major horizontal compressive stress. The largest induced earthquake, of magnitude $M = 1.2$, occurred 18 h after the beginning of injection (Zoback and Harjes, 1997). The study suggested that many earthquakes were induced by very small pore pressure changes (1 MPa) less than 1 percent more than the surrounding (approximately hydrostatic) pore pressure at depth.

The exploitation of the Romashinskoye oil field, the largest in Europe, located on the south part of the Tatarstan arch (Russia), began in the 1960's using water flooding as a secondary recovery method (Galybin, 1998). Observations showed that there was a time-dependent correlation between the beginning of the water injection and the seismic activity. Based on these observations, Galybin (1998) developed a quantitative mechanical model to address the influence of pore pressure on fault movements. He followed the original work by Hubbert (1959) and used the *Mohr-Coulomb* failure criterion for fault stability. Their model showed that the water flooding method may induce seismic events in historically aseismic regions and increase the magnitude of natural earthquakes in tectonically active regions.

As noted by Nicholson and Wesson (1992), in each of the well-documented examples of injection induced seismicity, there were three common characteristics; first, there was a close geological connection between the fluid injection zones and the earthquake locations; second, the measured or inferred in-situ stress and the measured pore pressure pointed out that the frictional strength along the favorably oriented pre-existing faults was surpassed; and third, there was a clear difference between any previous seismic history and

the induced earthquakes, which are often characterized by swarms of small shallow earthquakes lasting as long as the elevated pore pressures exist. It is now well understood that injection-induced seismicity is caused by the pore pressure increase allowing the inferred stresses in the Earth's crust to overcome the threshold for frictional sliding along favorably oriented pre-existing faults (Nicholson and Wesson, 1992). Since the shear stresses in the poroelastic constitutive relations (Detournay, 1993), are not affected by the pore pressure, it is usually assumed that the pre-existing shear stress is the main driving force for fault slip caused by the shear strength reduction due to the increased pore pressure.

Extraction induced seismicity

Triggered or induced earthquakes, which spatially correlate with areas of massive fluid withdrawal, can be classified into two rather broad categories (Nicholson and Wesson, 1992): (1) shallow and (2) deep induced earthquakes. The former occur near or within the producing zone and exhibit, in general, normal or reverse faulting focal mechanisms (studied in this work). They can be linked to the rapid subsidence and poroelastic strain changes due to the extraction of large volumes of fluid (Segall, 1987). The latter occur near the seismogenic zone base, often show signs of thrust focal mechanism and may be related to stress and/or strain changes due to the unloading effects of the removal of large amounts of fluid from the area undergoing crustal convergence. They are more ambiguous and much larger in magnitude than shallow induced earthquakes, and are much more difficult to separate from the background seismicity.

The first well documented example of shallow induced seismicity correlated with hydrocarbon extraction was probably given by Pratt (1926). In the Goose Creek oil field, in Galveston Bay, south Texas, production began in 1917 at depths ranging from 300 m to 1200 m, and by 1925, there was recorded surface subsidence by as much as 1 m centring over the producing field. Subsidence was accompanied by small earthquakes, and several normal faults developed along the field margins breaking the ground. Since then, in many other cases around the world, it has been possible to identify seismicity correlated with fluid withdrawal.

Probably, the most studied example of extraction-induced seismicity is that of the Lacq gas field where seismic events have been monitored for more than 25 years (Feignier, 1990; Grasso, 1992; Guyoton and Volant, 1992; Segall, 1994; Lahaie and Boyer, 1998). Since the onset of production in 1957, 220109 m³ of gas had been produced by 1995 and the reservoir pressure progressively declined from 66 MPa to 35 MPa in 1969 to 16 MPa in 1987 to 7.5 MPa in 1995 at 3700 m depth. The first seismic event was recorded in 1969, roughly 10 years after the gas exploitation started. Since 1974, when the local seismological network was deployed, more than 1000 seismic events with the largest magnitude ($M = 4.2$) in 1978 have been recorded in a historically aseismic region. More than 90 percent of the

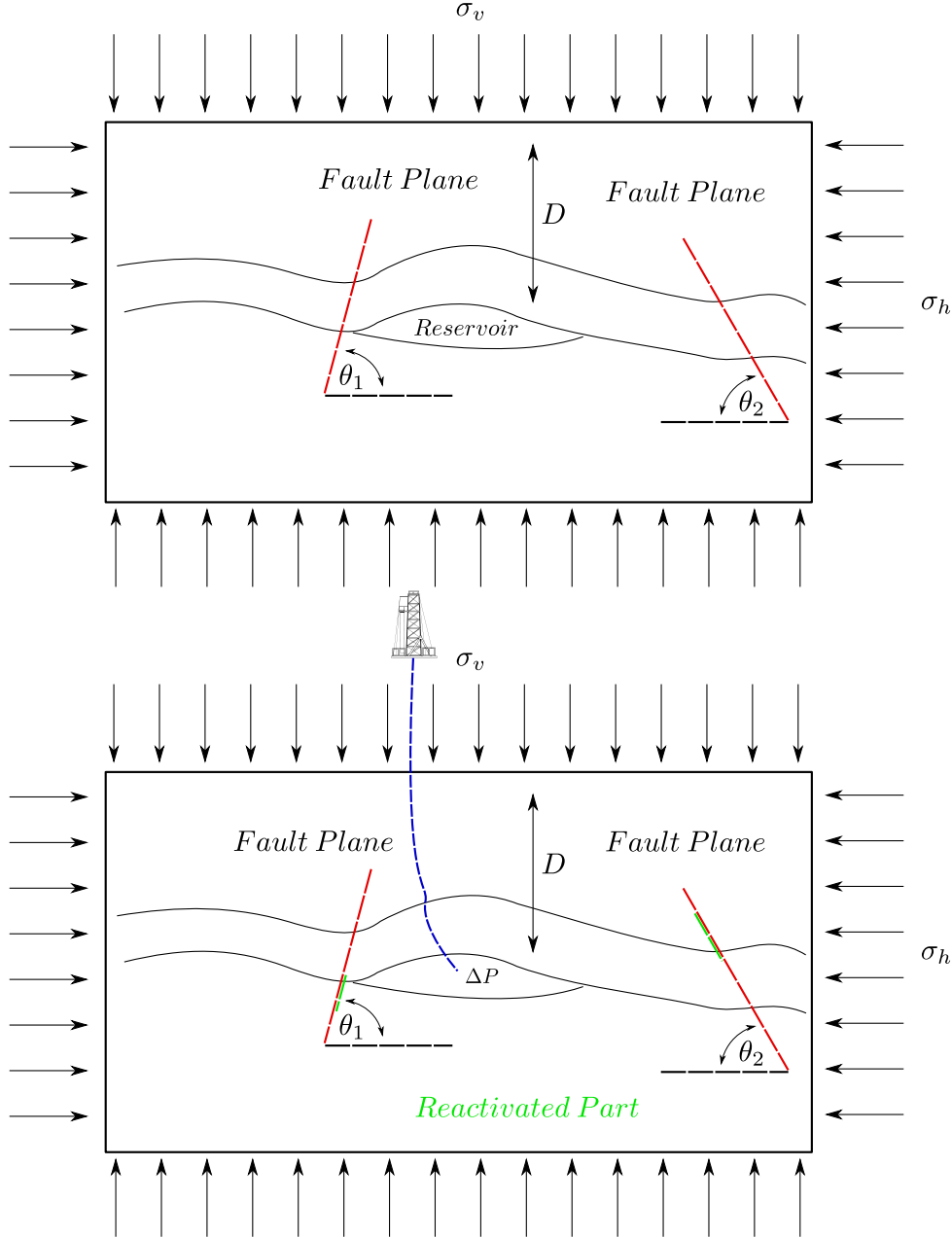
epicentres were located in the hydrocarbon field. Surface subsidence of about 60 mm has been observed over the 40 years of gas production in Lacq field.

Segall (1987) suggested that the poroelastic stressing of the reservoir and surrounding rocks, associated with volumetric contraction of the reservoir material, is responsible for the induced seismicity associated with fluid extraction. He suggested a mechanism of surface deformation and faulting associated with fluid extraction. Pore fluid withdrawal causes reduction in the pore pressure within the reservoir, triggering adjustments of the geological structures to perturbations related to the reservoir response to depletion. According to Segall (1987), poroelastic mechanisms transfer this stress change from the reservoir rock to its surroundings where seismic instabilities occur either above or below the reservoir if the faults are sufficiently pre-stressed.

Existing models of depleting hydrocarbon reservoirs

The increasing number of such cases initiated great interest in studying mechanics of fault reactivation, ground subsidence, reservoir deformation, and in-situ stress changes caused by fluid withdrawal *e.g.* (Geertsma, 1966; Segall, 1987; Teufel, 1991; Morita, 1992; Grasso, 1992; Rudnicki, 1999; Hawkes, 2009). In this section, existing models of depleting hydrocarbon reservoirs are reviewed. In most cases, the reservoir has been treated as a (partially) drained poroelastic inclusion surrounded by an elastic host material. Additionally, with conventional numerical modeling (Kosloff and Scott, 1980; Maillot, 1999; Roest, 1994; Ferronato, 2008), usually two approaches are implemented: (1) the reservoir is modeled as an inclusion with the same material properties as the matrix but with a different pore pressure (Geertsma, 1966; Segall, 1987, 1992, 1994); (2) the reservoir is modeled as a uniformly pressurized homogeneous ellipsoidal inclusion with properties different compared to the surrounding rock (Addis, 1998; Rudnicki, 1999). Figure 1.1 shows a schematic representation of poroelastic inclusion representing the depleted reservoir ΔP and induced stress changes in side burden rocks that can reactivate part of the pre-existent faults (green lines).

Figure 1.1: Fault reactivation problem divided in two parts. Upper) Initial problem. Lower) Perturbation problem. Fault inclination θ , and green zones represent reactivated part of fault planes. Source: redraw from Wang (2000).



Models based on homogeneous formation

The first approach is based on the works by Geertsma (1966) and Segall (1987), who investigated the subsidence caused by oil-reservoir depletion based on elastic continuum

mechanics. Geertsma (1966) treated an isolated volume of reduced pore pressure in a poroelastic half-space with a traction-free surface. He considered a disc-shaped, producing reservoir separated from its fluid-saturated, semi-infinite surroundings by an impermeable barrier. He assumed that the pore pressure distribution is independent of the displacement field and that the pore pressure can be determined by the uncoupled diffusion equation or that it is prescribed from measurements at a given time. Further, assuming that the reservoir and surrounding materials are homogeneous and have the same deformation properties, he analyzed the corresponding poroelastic problem using the concept of strain nucleus in the half-space, as it was introduced in the theory of thermoelasticity. He then computed the subsidence above the disc-shaped reservoir by integrating the nucleus solution (which, essentially, is a Green's function) over the entire reservoir volume. Although, Geertsma (1966) did not apply his model to induced seismicity, he was able to arrive at the important conclusion that the displacement field and subsidence are the result of shrinkage or compaction of the reservoir, which in turn depends upon the reservoir pressure reduction, height of productive interval, rock compressibility, as well as the depth of burial and the lateral extent of the reservoir.

Based on the theory of poroelasticity (Biot, 1941; Rice, 1976; Detournay, 1993; Segall, 1987) developed a model for computing poroelastic stress changes due to fluid extraction for general axisymmetric reservoir geometries and recovered the results of Geertsma (1966) for a thin disk reservoir with the uniform pressure decrease as a special case. As Geertsma (1966), rather than solving for pore pressure distribution, he assumed the pressure within the reservoir is known from the field measurements and reservoir simulations. He further assumed that the hydraulic diffusivity of the rocks surrounding the reservoir was sufficiently low so that the deformation outside the reservoir was not drained. However, he did consider the mechanical coupling between the stress and pore pressure and calculated the undrained pore pressure changes outside the reservoir (*i.e.*, ignoring changes in the fluid content).

Geertsma (1966) and Segall (1987) also assumed that the producing reservoir has the same elastic properties as the surrounding material to which it is perfectly bonded. He derived Green's functions equivalent to Geertsma (1966) approach for a radial pressure source (or sink). Using these Green's functions that are essentially identical to those appearing in similar thermoelastic problems, he was able to model flat reservoirs with arbitrary radial pressure distributions. Modeling Lacq gas field in France, Segall (1992) calculated the poroelastic stresses resulting from production generated decreases in pore pressure and suggested that these perturbed stresses are responsible for earthquakes associated with fluid extraction. However, his calculations showed that the perturbing stresses are only 0.01 MPa, which is at least an order of magnitude smaller than typical stress decrease (0.1 - 10 MPa) associated with earthquakes in nature. Therefore, he concluded that

extraction of fluids in Lacq gas field destabilized only those faults that are already near the frictional instability limit, *i.e.* shear stresses are near to overcome the frictional strength existing on fault planes. Though the stress changes he computed were very small, he did make a comment that steep pressure gradients in pore pressure could lead to local stress concentrations.

the models of Geertsma (1966), Segall (1987) and after Segall (1992) were aimed at accounting for the main reason for stress redistribution around depleted reservoir: the change in reservoir pore pressure. Not only did they consider the stress changes within the reservoir but also in its surrounding material. After that, Segall (1992) also used his model to analyze the onset of fault instability. Both models assumed the elastic properties of the reservoir to be identical to those of the surrounding material. The fact that the material is homogeneous allowed Geertsma (1966) to consider the interaction between the reservoir and the Earth's surface via employing the model of a half-space. Furthermore, because the solution was based on the corresponding Green's function for the homogeneous half-space, it was possible to study non-uniform pressure distributions and non-planar reservoirs (Segall, 1992). Even though, in general, the approach requires numerical computing of improper integrals, it is still analytical by nature and allows for a relatively simple analysis of rather geologically complex cases as, for example Grasso (1992), Hawkes (2009).

Models based on ellipsoidal inhomogeneity

The second approach, by Addis (1998) and Rudnicki (1999), allows for consideration of the additional factor of material heterogeneity, *i.e.*, the difference in the properties between the reservoir and surrounding rocks. Their approach is based on Eshelby's work (Eshelby, 1957) on ellipsoidal inhomogeneity. Addis (1998) and Rudnicki (1999) considered the reservoir to be represented by an ellipsoidal inclusion and the overburden by the host material. Both the reservoir and the overburden were considered homogeneous isotropic poroelastic materials with the properties of the inclusion being different from those of the surrounding material.

The inhomogeneity was assumed to be embedded in an infinite medium. This corresponds to the reservoir for which the depth from the surface is greater than its lateral extent (Rudnicki, 1999). Accordingly, both Addis (1998) and Rudnicki (1999) did not account for the interaction of the depleting reservoir with the free surface. The inhomogeneity or inclusion was assumed to be hydraulically isolated so that its pore pressure could differ from the surrounding material. They also assumed that the reservoir is relatively permeable and conductive so that it has a uniform distribution of pore pressure. Finally, they assumed that no pressure change occurs outside the reservoir or, in other words, they assumed drained deformation of the surrounding rock.

Modelling the reservoir with a homogeneous ellipsoidal inclusion, with different elastic properties and a pore pressure uniform throughout the reservoir (Mura, 1982), allowed Addis (1998) and Rudnicki (1999) to study the effect of various ellipsoidal geometries and property mismatch on alterations of the local stress state inside the reservoir caused by the pore pressure changes. Addis (1998) considered a large flat oblate horizontal reservoir (that is, in the extreme of the infinitesimal aspect ratio) and concluded that the stress-depletion response inside the reservoir decreases with increasing magnitude of Poisson's ratio and decreasing value of Biot's poroelastic parameter of the reservoir material and that the moduli of the reservoir and surrounding rocks have little influence on the stress response inside the reservoir.

Rudnicki (1999) also considered an axisymmetric inhomogeneity, but, in addition to the effect of Poisson's ratio and the shear modulus, he also studied the influence of the aspect ratio of the reservoir on the stress depletion response inside the reservoir. He concluded that as the shape of the reservoir becomes flatter (tending in the limit towards a layered geometry), the axial stress perturbation approaches zero, but the approach is slower for smaller values of Poisson's ratio and the shear modulus of the reservoir material. Further, the strain perturbation within the reservoir approaches to the uniaxial model with the decreasing aspect ratio of the reservoir, but the approach is slower if the shear modulus of the inhomogeneity exceeds that of the surrounding material. In the limit of the infinitesimal aspect ratio, the effect of contrast in the shear modulus becomes insignificant on both the axial and lateral stress perturbations inside the reservoir. However, the influence of Poisson's ratio becomes insignificant only in the case of axial stress perturbation while the lateral stress perturbation can differ by a few times. Rudnicki (1999) further used the calculated stress paths to evaluate whether the stress state is going towards or away from failure on faults within the reservoir.

Segall (1994) also used the inclusion method proposed by Eshelby (1957) to compute the stress changes occurring within hydrocarbon reservoirs, but considered the properties of the reservoir material to be same as the surrounding material. Their analysis showed that if the regional stress is extensional (*i.e.*, normal faulting stress regime), the Biot's coefficient is greater than 0.85, Poisson's ratio is 0.20, the reservoir aspect ratio is 1/26, and the coefficient of friction is smaller than 0.5, then normal faulting is promoted within the reservoir itself due to its depletion. Regardless of these conditions, dilatant fracturing and normal faulting are always stimulated near the edges of the reservoir or near the regions of high-pore pressure gradients at the boundary. In the compressional regional stress environment (*i.e.*, reverse faulting stress regime), reverse faulting is stimulated above and below the level of the reservoir due to reservoir depletion.

Since Addis (1998) and Rudnicki (1999) focused on the stress-depletion response within the reservoir, they did not evaluate the poroelastic deformation and possible fault reac-

tivation outside the reservoir. Nevertheless, although in their model, the reservoir pore pressure was assumed to be uniform throughout and, therefore, they could not analyze the depletion strategies associated with non-uniform distributions of reservoir pore pressure, their work demonstrated that indeed, material inhomogeneity is an important factor (in addition to the changes in the reservoir pore pressure).

1.2.3 Continuous Galerkin (CG) method

In terms of geomechanical modeling many techniques have been developed in order to simulate physical processes such as stress/strain behavior, fluid flow, heat transfer and dynamic loading in complex situations. They are often used to estimate the effects of mining activities on stress/strain behavior of rocks and environmental issues. Many techniques have been developed such as the finite element, finite difference, discrete element, distinct element (Rejeb, 1996) and boundary element methods. For this work the finite element method is chosen and implemented in a C++ code called LPA (Linear Poroelastic Analysis), in order to provide a non-commercial option to study the fault reactivation issues by means of linear poroelasticity.

The most popular numerical techniques for solving poromechanics problems are the continuous Galerkin (CG) finite element methods. The first application of the CG finite element methods to model the flow of compressible fluid in porous elastic media began in 1969 by Wilson (1973). Their finite element formulation was based on Gurtin's variational principle (Gurtin, 1964) and applied to three-dimensional soil consolidation problems. The stability of the CG methods was first briefly commented on Wilson (1973). He pointed out that a very small time step resulted in oscillatory pressure for problems with low permeability. However, he didn't present his unstable results obtained with small time steps. The earliest appropriate use of finite element spaces for consolidation problems is attributed to Hwang (1971). In his numerical study on plane strain consolidation problems, a six node triangle was used to represent a quadratic displacement field and a three node triangle was selected to represent a linear pore pressure field. These proposed finite element spaces happened to represent a stable scheme, which satisfies the Ladyzhenskaya-Babuska-Brezzi (LBB) inf-sup condition (Brezzi, 1991). However, this scheme is not popular in practical applications due to the constraint on approximation spaces which requires complex programming. However using the NeoPZ environment, arbitrary approximation orders can be used for pressure and displacement, consequently LBB condition is easily satisfied. Vermeer and Verruijt (1981) were the first who demonstrated nonphysical pressure oscillations in continuous Galerkin (CG) finite element solutions, which are induced by using small time steps. Their stability analysis was based on a 1-D problem. They showed that there is a lower bound for the time step, dependent

on the order of the finite elements employed, below which spatial oscillations in pressure will occur. A few techniques have been proposed to remove the oscillation in pressure solution obtained by the popular CG methods. An obvious technique is to use a fine mesh or a high order element near the boundary. Indeed, this method can help to alleviate the oscillation. But it is not able to completely remove the oscillation until an extremely fine mesh is used, which is not practical. Sandhu (1977) proposed to use singular elements near the loaded surface. However, the appropriate polynomial order of singular elements could exceed 60 degrees, which could be difficult for computer implementations. In fact these oscillations do not only depend on the LBB condition. They occur for any approximation of parabolic problems. An intensive search for an appropriate stabilizing parameter is required for this stabilized CG method. Since the (LBB) condition is satisfied, it is easy to show that no considerable oscillations in pressure occur in comparison with cheap linear-linear elements; thus a reasonable approximation can be obtained using cubic-quadratic or high order elements for displacement and pressure chosen as state variables.

1.3 Research objectives

The main objective of the research presented in this dissertation is to understand the fundamental mechanisms of fault reactivation induced by oil production using 2D geomechanical modelling of oil reservoirs, as well as to develop the corresponding quantitative numerical implementation. Ideally, any model intended to simulate a physical phenomenon should be calibrated against the real data for practical implementation but this is left for future works. Therefore, the suggested implementation is a simple and robust platform to generate numerical models, that would allow to do parametric analysis and identify the critical issues related to induced reservoir fault reactivation caused by hydrocarbon production, following the next specific objectives:

- To understand fundamental mechanisms of fault reactivation due to reservoir depletion by means of poroelastic effects.
- To develop a simple, robust, and quantitative numerical model for the depletion of a hydrocarbon reservoir.
- To account for both non-uniform pressure distribution within the reservoir and material contrast between reservoir and surrounding rocks.
- To analyze the onset of fault instability caused by the perturbation a known initial stress state.
- To identify the important parameters affecting the fault stability.

The study focuses on the influence of several geomechanical parameters on stress development and fault slip in and around an arbitrary-shaped oil reservoir intersected or not by a normal or reverse faults that are represented with potential slip surfaces in continuous poroelastic media. Attention is given to the development, implementation and quantification methods. Which include arching, normal, shear stress and fault reactivation factor along faults plane. Parameters include reservoir geometry, reservoir size, depth, tilt angle, reservoir shape and surrounding rock properties.

As discussed in the previous section, the existing models based on the approach of a homogeneous formation accounted for the principal reason of stress redistribution around depleted reservoirs, *i.e.* a change in reservoir pore pressure, while those utilizing the approach of ellipsoidal inclusion accounted for another important factor of material inhomogeneity, but considered uniform pressure distribution inside the reservoir. The next natural step is to account for both the non-uniform reservoir pressure and the material inhomogeneity in the model by using this numerical approach.

1.4 Outline of dissertation

A theoretical review of the constitutive equations for mono-phasic poroelastic model is given in Chapter 2. Main assumptions made in the model are discussed. A dimensionless form of the strong formulation is presented in Chapter 2. Also theoretical concepts and a mathematical description of semi-analytical method for fault reactivation using inclusion theory are provided in chapter 2. Through 3, the weak statement and finite element continuous Galerkin formulation is presented. The corresponding computational implementation and validation with some analytical solutions is presented in Chapter 4. Finally fault reactivation tendency caused by the reservoir depletion is analyzed and numerical comparison with STARS Simulator for reservoir geomechanics calculations is given in Chapter 5. The effect of different depletion strategies (*e.g.*, various pressure distributions) as well as of the reservoir rigidity on the onset of fault reactivation are studied. Chapter 6 summarizes results and conclusions obtained in this work and provides some recommendations for future research.

2. Theoretical concepts

2.1 Small deformations in porous media

With the current progress in the mechanics of porous media and non-linear finite element analysis, a finite deformation analysis of coupled problem can be established directly. However, it is still necessary to establish a separate small deformation formulation for comparison and modeling purposes. First, for some simple cases, it is possible to find analytical solutions under the small deformation assumption. The analytical solutions can be used in the validation of the small deformation analysis, as well as in the finite deformation analysis at small strains. Under the finite deformation assumption, it is more difficult (in most cases impossible) to find an analytical solution. Thus, the small deformation analysis provides a good comparison to the finite deformation analysis. Second, the results from the small deformation analysis are usually accurate enough in the small deformation regime, and the amount of computer time required in the small deformation analysis is much less than that of the finite deformation analysis. Thus the small deformation approach is still acceptable and even preferable for engineering problems at small strains. Although the response of near surface earth materials is seldom precisely linear, the theory of linear fluid infiltrated elastic solids has proven to be very useful in studying a variety of geotechnical and geophysical problems. These include soil consolidation (Biot, 1941), hydraulic fracture (Cleary, 1979), and various aspects of earth faulting (Booker, 1974; Rudnicki, 1986).

Even in the small strain regime, there are a number of ways to investigate the transient response of fluid saturated porous media subject to external loading. The problem can be simplified under different assumptions. In some cases, when the permeability of the saturated rock is very small or large, the problem may be simplified by assuming undrained or drained condition. Usually, the undrained condition assumption is valid if the rate of loading is much higher than the diffusion of pore fluid. In this case, very little amount of pore fluid can escape in transient process, the mass content of fluid in each material element remains essentially constant, and there is no relative displacement between the fluid phase and the solid skeleton. On the other hand, if the loading rate is much smaller

than the diffusion rate of the pore fluid, the pore pressure in each material element can be assumed to remain constant at its hydrostatic level, and does not vary with the solid skeleton deformation.

The most direct formulation of governing equations for a linear poroelastic solid were established by Biot (1941), other formulations have been given by Bear (1972), Rice (1976), Cleary (1977), Rudnicki (1986) and Wang (2000). A treatment of the equations based on those works is presented in this section.

2.2 Poroelastic formulation

2.2.1 Main assumptions

The most common and general cases in reality are intermediate. Generally an interaction exists between the solid phase and the fluid phase. The pore fluid flows out during loading, the pore fluid pressure varies with time. To analyze these cases, a mono-phasic continuum model must be formulated to incorporate the effect of the transient flow of the fluid through the porous media.

The following assumptions are introduced in this analysis:

- No inertial effects, *i.e.* a quasi-static deformation process.
- Small deformation regime.
- Isothermal flow.
- The flow is governed by diffusive mass flux.
- Full saturated isotropic solid.
- The permeability tensor is diagonal.
- Compressible rock formation. Fluid flow is characterized by Darcy's law (a thorough study of Darcy's law is given for Bear (1972)). Some assumptions are intrinsically related to Darcy's law:
- Fluid phase is homogeneous and Newtonian.
- No chemical reaction, precipitation or adsorption occurs.
- There is no electro-kinetic effect.

Used sign convention

The sign convention used in this work conforms to the continuum mechanics convention: Tension stress is defined as a positive field.

State variables

For the small deformation analysis, the state of saturated porous media can be fully expressed in the following variables:

- Excess pore pressure, P^{ex} ;
- The average displacement of the solid phase, \mathbf{u} ;

The mass conservation equations of the solid and fluid phases are derived. An arbitrary volume V_{vol} containing solid and fluid phases is considered. Assuming a fully saturated solid, then the volume occupied by the fluid phase (*i.e.* f suffix for fluid phase) is ϕV_{vol} . Let ρ_f , ρ_{solid} represent the mass density of fluid and solid phase of a continuum, respectively. The total mass of fluid contained in arbitrary volume V_{vol} can be written as

$$m_f = \int_{V_{vol}} \rho_f \phi dV_{volume} \quad (2.1)$$

while the total mass of solid contained in the same volume is

$$m_{solid} = \int_{V_{vol}} \rho_{solid} (1 - \phi) dV_{volume} \quad (2.2)$$

The balance of mass for the fluid phase gives

$$\frac{dm_f}{dt} = \int_{V_{vol}} \frac{\partial (\rho_f \phi)}{\partial t} + \nabla \cdot (\rho_f \phi \mathbf{v}_f) dV_{volume} = 0 \quad (2.3)$$

Where \mathbf{v}_f is the interstitial phase velocity. The balance of mass for the solid phase gives

$$\frac{dm_{solid}}{dt} = \int_{V_{vol}} \frac{\partial (\rho_{solid} (1 - \phi))}{\partial t} + \nabla \cdot (\rho_{solid} (1 - \phi) \mathbf{v}_{solid}) dV_{volume} = 0 \quad (2.4)$$

With V_{vol} being arbitrary, the last two equations using the localization theorem given in Gurtin (1981) take the following localized form:

for the fluid phase

$$\frac{\partial (\rho_f \phi)}{\partial t} + \nabla \cdot (\rho_f \phi \mathbf{v}_f) = 0 \quad (2.5)$$

for the solid phase

$$\frac{\partial (\rho_{solid} (1 - \phi))}{\partial t} + \nabla \cdot (\rho_{solid} (1 - \phi) \mathbf{v}_{solid}) = 0 \quad (2.6)$$

2.2.2 Fluid potential and excess pore pressure

In earth sciences *e.g.* reservoir engineering, geology and hydrology, fluid potential at a point is defined as the work required by frictionless process to transport a unit mass of fluid from a state of atmospheric pressure to zero elevation or absolute datum to the point in question D *i.e.* $D = Z_{datum} - Z$. Mathematically the definition of Hubbert Φ_H fluid potential for any fluid (valid for compressible and incompressible fluid Ertekin (2001)) is:

$$\Phi_H = \int_{P_{datum}}^P \frac{1}{\gamma(P)} dP - D \quad (2.7)$$

The potential gradient is obtained from (2.7)

$$\nabla \Phi_H = \nabla \left(\int_{P_{ref}}^P \frac{1}{\gamma(P)} dP - D \right) = \frac{1}{\gamma} \nabla (P - D) \quad (2.8)$$

multiplying the $\nabla \Phi_H$ by γ , the conventional form of the fluid potential is found

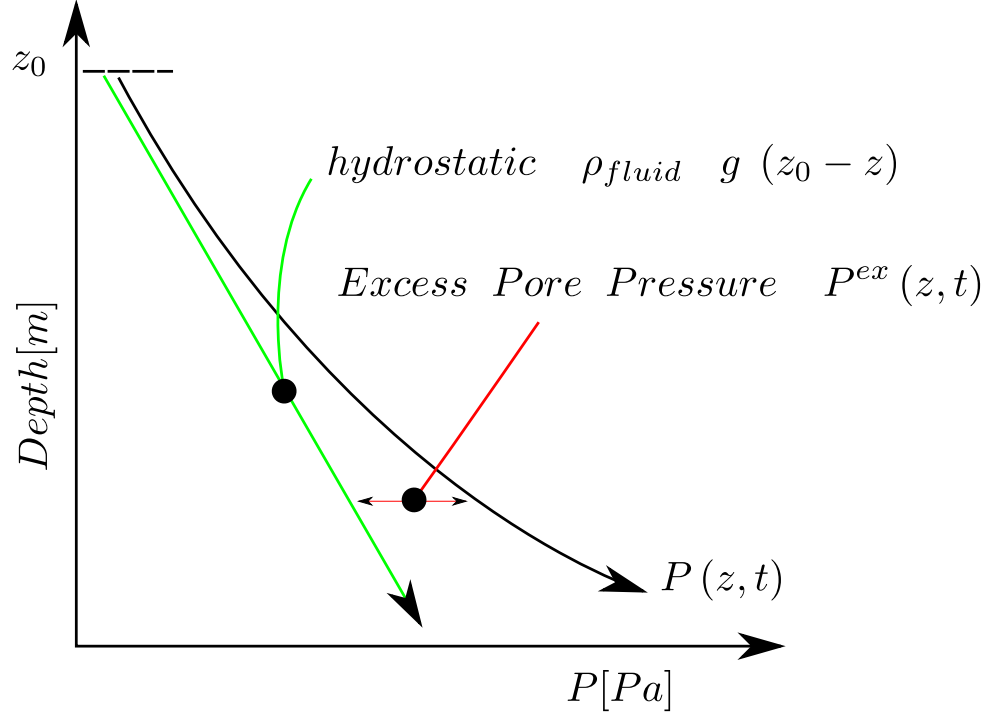
$$\nabla \Phi = \gamma \nabla \Phi_H = \nabla (P - \rho_f g D) \quad (2.9)$$

where $\gamma(P) = \rho_f(P) g$ is the fluid density in terms of pressure per distance usually called *fluid gravity*.

In geomechanics a typical problem is to find fluid pore pressure and displacement response due to applied load or to fluid extraction Wang (2000). If the fluid is static in the initial state, it is possible to decompose the total pressure into the sum of hydrostatic pressure and an excess pore pressure P^{ex} (figure 2.1). Excess pore pressure is the total pore pressure minus hydrostatic pressure. Thus P^{ex} is analogue to fluid potential and can be expressed as:

$$P^{ex} = P - \gamma D \quad (2.10)$$

Figure 2.1: Definition of excess pore pressure as decomposed total pressure referred to hydrostatic pressure. Source: redraw from Wang (2000).



2.2.3 Darcy's law

Darcy's law is an empirical relationship between the flow rate through a porous medium and the potential gradient. The Darcy average velocity of fluid phase $\bar{\mathbf{v}}_f$ is given as:

$$\bar{\mathbf{v}}_f = -\frac{\kappa}{\eta} \nabla \Phi = -\frac{\kappa}{\eta} \nabla P^{ex} \quad (2.11)$$

$$\bar{\mathbf{v}}_{mf} = \mathbf{q}_f = -\rho_f \frac{\kappa}{\eta} \nabla \Phi = -\rho_f \frac{\kappa}{\eta} \nabla P^{ex} \quad (2.12)$$

while $\bar{\mathbf{v}}_f$ is the Darcy velocity, κ is a diagonal absolute permeability tensor.

Darcy's law can be considered an empirical or analytical expression derived from the Navier Stokes equation (*e.g.* derivation is presented on Bear (1972)). In either case, it is still the cornerstone of the contemporary reservoir simulation.

It is important to point out that the mass balance in the petroleum industry really are the volume conservation equations written in terms of volumetric volume factors of each phase; the basis for this mass balance is the volume of each phase at stock-tank conditions. Once the stock tank conditions are specified, the volume balance of the oil, water and gas

may be converted through the phase densities at stock-tank conditions. Taking the fact that Darcy law describes flow with respect to the solid matrix Biot (1941), the macroscopic Darcy velocity can be written as:

$$\begin{aligned}\bar{\mathbf{v}}_f &= \phi(\mathbf{v}_f - \mathbf{v}_{solid}) \\ \phi\mathbf{v}_f &= \bar{\mathbf{v}}_f + \phi\mathbf{v}_{solid}\end{aligned}\quad (2.13)$$

Substituting this in the mass balance equation 2.5 for $\bar{\mathbf{v}}_f$

$$\frac{\partial(\phi\rho_f)}{\partial t} = -\nabla \cdot (\rho_f\bar{\mathbf{v}}_f) - \nabla \cdot (\phi\rho_f\mathbf{v}_{solid}) + q_f \quad (2.14)$$

in terms of $\bar{\mathbf{v}}_{mf}$, the continuity equation became:

$$\frac{\partial(\phi\rho_f)}{\partial t} = -\nabla \cdot (\bar{\mathbf{v}}_{mf}) - \nabla \cdot (\rho_f\mathbf{v}_{solid}) + q_f \quad (2.15)$$

The coupling term in a poroelastic simulation are ϕ and \mathbf{v}_s , they account for the effect of solid deformation on flows. A conventional reservoir simulation is based on the fact that rock deforms very slowly compared to multiphase flow, *i.e.* in equation 2.13 $\mathbf{v}_{solid} \lll \bar{\mathbf{v}}_f$ so $\bar{\mathbf{v}}_f = \phi\mathbf{v}_f$.

Applying the chain rule over equations 2.15 and 2.6:

$$\frac{\partial(\phi\rho_f)}{\partial t} + \nabla \cdot (\bar{\mathbf{v}}_{mf}) + \mathbf{v}_{solid} \cdot \nabla(\phi\rho_f) + \phi\rho_f\nabla \cdot \mathbf{v}_{solid} = q_f \quad (2.16)$$

$$\frac{\partial((1-\phi)\rho_{solid})}{\partial t} + \mathbf{v}_{solid} \cdot \nabla((1-\phi)\rho_{solid}) + (1-\phi)\rho_{solid}\nabla \cdot (\mathbf{v}_{solid}) = 0 \quad (2.17)$$

applying the definition of Lagrangian's total derivative with respect to a moving solid:

$$\frac{D(\cdot)}{Dt} = \frac{\partial(\cdot)}{\partial t} + \mathbf{v}_{solid} \cdot \nabla(\cdot) \quad (2.18)$$

Equations can be written as:

$$\frac{D(\phi\rho_f)}{Dt} + \nabla \cdot \bar{\mathbf{v}}_{mf} + \phi\rho_f\nabla \cdot \mathbf{v}_{solid} = q_f \quad (2.19)$$

$$\frac{D((1-\phi)\rho_{solid})}{Dt} + (1-\phi)\rho_{solid}\nabla \cdot \mathbf{v}_{solid} \quad (2.20)$$

solving for $\nabla \cdot \mathbf{v}_{solid}$

$$\nabla \cdot \mathbf{v}_{solid} = -\frac{1}{(1-\phi)\rho_{solid}} \frac{D((1-\phi)\rho_{solid})}{Dt} \quad (2.21)$$

introducing the solid fraction $1 - \phi = \frac{V_{solid}}{V_{bulk}}$ and since the volume of solids remains constant $\partial \rho_{solid} V_{solid} = (1 - \phi) \partial V_{bulk} = \text{constant}$, is obtained:

$$\begin{aligned}
 \nabla \cdot \mathbf{v}_{solid} &= -\frac{V_{bulk}}{\rho_{solid} V_{solid}} \frac{D(\rho_{solid} V_{solid})}{Dt} \\
 &= \left(-\frac{V_{bulk}}{\rho_{solid} V_{solid}} \right) \left(\frac{\frac{D(\rho_{solid} V_{solid})}{Dt}}{V_{bulk}^2} - \rho_{solid} V_{solid} \frac{D(V_{bulk})}{Dt} \right) \\
 &= \left(-\frac{V_{bulk}}{\rho_{solid} V_{solid}} \right) \left(-\frac{\rho_{solid} V_{solid} \frac{D(V_{bulk})}{Dt}}{V_{bulk}^2} \right) \\
 &= \frac{1}{V_{bulk}} \frac{D(V_{bulk})}{Dt}
 \end{aligned} \tag{2.22}$$

but $\varepsilon_v = \nabla \cdot \mathbf{u} = \frac{\partial V_{bulk}}{V_{bulk}}$, $\mathbf{v}_{solid} = \frac{D\mathbf{u}}{Dt}$ and taking the divergence of this becomes:

$$\nabla \cdot \mathbf{v}_{solid} = \frac{D\nabla \cdot \mathbf{u}}{Dt} \tag{2.23}$$

so that:

$$\frac{D\varepsilon_v}{Dt} = \frac{1}{V_{bulk}} \frac{D(V_{bulk})}{Dt} \tag{2.24}$$

the divergence of solid velocity reflects the rate of bulk volume change, substituting $\nabla \cdot \mathbf{v}_{solid}$ with $\frac{D\varepsilon_v}{Dt}$ in 2.19, the result is:

$$\frac{D(\phi \rho_f)}{Dt} + (\phi \rho_f) \frac{D\varepsilon_v}{Dt} + \nabla \cdot \bar{\mathbf{v}}_{mf} = q_f \tag{2.25}$$

adding and subtracting $\varepsilon_v \frac{D(\phi \rho_f)}{Dt}$

$$\frac{D(\phi(1 + \varepsilon_v) \rho_f)}{Dt} + \nabla \cdot \bar{\mathbf{v}}_{mf} - \varepsilon_v \frac{D(\phi \rho_f)}{Dt} = q_f \tag{2.26}$$

since the last term on the left hand side is small compared to the term $\frac{D(\phi(1 + \varepsilon_v) \rho_f)}{Dt}$

$$\varepsilon_v \frac{D(\phi \rho_f)}{Dt} \lll \frac{D(\phi(1 + \varepsilon_v) \rho_f)}{Dt} \tag{2.27}$$

$\varepsilon_v \frac{D(\phi \rho_f)}{Dt}$ can be neglected. Thus the last equation can be written in a form quite similar to the flow equations in a uncoupled simulation

$$\frac{D(\phi^* \rho_f)}{Dt} + \nabla \cdot \bar{\mathbf{v}}_{mf} = q_f \tag{2.28}$$

where ϕ^* is the so called fluid fraction and is defined as

$$\phi^* = \phi(1 + \varepsilon_v) \tag{2.29}$$

for a poroelastic material with small deformation regime, the total bulk volume V_{bulk} can be approximated by a linear function of ε_v as $V_{bulk} = V_{bulk}^\circ (1 + \varepsilon_v)$ and taking into account this approximation in equation 2.29. The fluid fraction or fluid mass content (Rudnicki, 1986) ϕ^* can be viewed as the system “porosity” relative to the initial under-formed bulk volume V_{bulk}° *i.e.*

$$\phi^* = \phi \frac{V_{bulk}}{V_{bulk}^\circ} = \frac{V_{porous}}{V_{bulk}^\circ} \quad (2.30)$$

Non-deformable porous media or the initial state of deformable porous media implies that the fluid fraction ϕ^* is equal to the true porosity ϕ . However in an uncoupled reservoir model, the contribution of total stress to the fluid fractions is always approximated by the linear function of pore pressure

$$\phi^* = \phi (1 + C_r (P^{ex} - P_o^{ex})) \quad (2.31)$$

with C_r as rock compressibility.

According to Geertsma (1957), the relative porosity variation in a deformed medium is approximated by

$$\frac{d\phi}{\phi} = \left(\frac{1}{\phi} \left(\frac{1}{K_b} - \frac{1}{K_s} \right) - \frac{1}{K_b} \right) (d\bar{\sigma} + dP^{ex}) \quad (2.32)$$

where $\bar{\sigma} = \frac{3\lambda+2\mu}{3}\varepsilon_v - \alpha P^{ex}$ is the mean stress, K_b and K_s are respectively the bulk modulus of solid matrix and solid constituents. The Biot's coefficient α (Biot, 1941) can be measured independently in a jacketed drained test and is associated with K_b and K_s by the following relationship

$$\alpha = \left(1 - \frac{K_b}{K_s} \right) \quad (2.33)$$

If small strain modelling is assumed the porosity ϕ can be approximated from equation 2.32

$$\phi^* = \phi_o + \left(\frac{1}{\phi} \left(\frac{(1 - \phi_o)}{K_b} - \frac{1}{K_s} \right) - \frac{1}{K_b} \right) (\bar{\sigma} + P^{ex}) \quad (2.34)$$

by using $\phi^* = \phi (1 + \varepsilon_v)$ or $\phi = \frac{\phi^*}{(1 + \varepsilon_v)}$, it becomes

$$\phi^* = \phi_o + (C_b - (1 + \phi_o) C_s) P^{ex} + (C_b - C_s) \bar{\sigma} \quad (2.35)$$

or in terms of ε and P^{ex}

$$\phi^* = \phi_o + \alpha \varepsilon_v + \frac{1}{M} P^{ex} \quad (2.36)$$

where the M is Biot's constant defined as

$$\frac{1}{M} = (1 - \alpha)(\alpha - \phi_o)C_b \quad (2.37)$$

C_b and C_s are respectively the bulk compressibility and solid grain compressibility, they are related to K_b and K_s by

$$\begin{aligned} C_b &= \frac{1}{K_b} \\ C_s &= \frac{1}{K_s} \end{aligned} \quad (2.38)$$

if $M > 0$ α lies within the following bounds

$$\phi_o \leq \alpha \leq 1 \quad (2.39)$$

if the solid material is incompressible, $C_s = 0$ and $\alpha = 1$ or $\alpha = \phi_o$ then $\frac{1}{M} = 0$. Finally, a low advective velocity is imposed on the coupled mass balance equation $\frac{\partial(\phi^* \rho_f)}{\partial t} \gg \mathbf{v}_{solid} \cdot \nabla(\phi^* \rho_f)$, that is

$$\frac{D(\phi^* \rho_f)}{Dt} \approx \frac{\partial(\phi^* \rho_f)}{\partial t} \quad (2.40)$$

The physical interpretation of this approximation is that the medium is undergoing deformation but remains stationary. Thus the multiphase flow equation 2.28 coupled with geomechanics can finally be written as

$$\frac{\partial(\rho_f(\phi_o + \alpha \nabla \cdot \mathbf{u} + \frac{1}{M} P^{ex}))}{\partial t} + \nabla \cdot \bar{\mathbf{v}}_{mf} = q_f \quad (2.41)$$

with ϕ^* replaced by equation 2.36. However, in rock mechanics analysis, it is standard to write the coupled equations in terms of total stress and excess pore pressure as

$$\phi^* \frac{\partial(\rho_f)}{\partial t} + \rho_f (C_b - (1 + \phi_o) C_s) \frac{\partial(P^{ex})}{\partial t} + \rho_f (C_b - C_s) \frac{\partial(\bar{\sigma})}{\partial t} + \nabla \cdot \bar{\mathbf{v}}_{mf} = q_f \quad (2.42)$$

The above derivation is based on volume variations, including bulk volume, pore volume and porosity variations. As a result, displacements or stresses explicitly show up in the continuity equations.

Another term that implicitly involves geomechanical effect is the transmissibility term ($\nabla \cdot \bar{\mathbf{v}}_f$) through permeability changes, although rock permeability is generally considered to remain constant in standard reservoir simulations. Permeability-stress coupling, however, is not a direct coupling as in pore volume. It is usually conducted in a stepped manner. One simple approach is to assume that permeability depends on porosity as, for example, according to the Garman-Kozeny relation commonly used in basin simulators. Other

stress-dependent permeability models may also be used, *e.g.* Morita (1992). Here, it is pointed out that pore volume coupling is the primary interest of this work. Permeability-stress coupling and non-linear relations of fluid properties by dependence of pressure are proposed as future works.

In summary the mathematical description for coupling porous flow and geomechanics must account for the following important characteristics of the reservoir system (Osorio, 1992):

1. The multi-component nature of the reservoirs require descriptions for both the pore pressure of fluids and the solid components, so mass and force conservation laws and constitutive relations, which represent the coupling effects must be combined to obtain the fully coupled equations.
2. Pressure depletion, which occurs inside the reservoir induces an extended stress-disturbed region outside the reservoir boundaries. The disturbed region affects the evolution of the stress at the reservoir boundaries. The geomechanical interaction between boundaries and stress state inside the reservoir is a fully coupled process. This indicates that the inclusion of a surrounding environment (over burden, under burden and side burden) is necessary to achieve a realistic modeling of the actual geomechanical boundary conditions. Indeed the surrounding domain needs to be extensive enough to ensure that its boundaries are not perturbed by reservoir production or injections during the time period of interest.

2.2.4 Strong formulation

Returning to the formulation, the coupled mass balance and force equations are written as:

$$\frac{\partial}{\partial t} (\rho_f (\phi_o + \alpha (\nabla \cdot \mathbf{u} - \nabla \cdot \mathbf{u}_o) + S_\epsilon (P^{ex} - P_o^{ex}))) + \nabla \cdot \rho_f \bar{\mathbf{v}}_f = q_f \quad (2.43)$$

where $S_\epsilon = \frac{1}{M}$, and

$$\bar{\mathbf{v}}_f = -\frac{\kappa}{\eta} (\nabla P^{ex}) \quad (2.44)$$

and the corresponding initial and boundary conditions

$$\begin{aligned} & \text{Initial at time } t_o \\ & \left\{ P^{ex} = P_o^{ex} \right. \\ & \text{Boundary on } \partial\Gamma \\ & \left\{ \begin{array}{ll} \bar{\mathbf{v}}_f \cdot \mathbf{n} & \text{on } \partial\Gamma_q \\ P^{ex} & \text{on } \partial\Gamma_{P^{ex}} \end{array} \right. \end{aligned} \quad (2.45)$$

The system is complete with equilibrium equation and linear elastic constitutive behavior:

$$\begin{aligned} \nabla \cdot \sigma_t + \mathbf{b} &= 0 \\ \text{and} \\ \sigma_t &= \mu(\nabla \mathbf{u} + \nabla^T \mathbf{u}) + \lambda \nabla \cdot \mathbf{u} - \alpha (P^{ex}) I \end{aligned} \quad (2.46)$$

defining the corresponding initial and boundary conditions

$$\begin{aligned} &\text{Initial at time } t_o \\ &\begin{cases} P_o^{ex} = P_o^{ex} \\ \mathbf{u} = \mathbf{u}_o \end{cases} \\ &\text{Boundary on } \partial\Gamma \\ &\begin{cases} \sigma \cdot \mathbf{n} & \text{on } \partial\Gamma_{\sigma_t} \\ \mathbf{u} & \text{on } \partial\Gamma_u \end{cases} \end{aligned} \quad (2.47)$$

The mono-phasic flow at reservoir conditions for compressible solid and fluid constituents is given by taking the divergence of linear constitutive equation 2.46. Thus the system becomes:

$$\begin{aligned} (\lambda + \mu) \nabla (\nabla \cdot \mathbf{u}) + \mu \nabla^2 \mathbf{u} - \alpha \nabla P^{ex} + \mathbf{b} &= 0 \\ \alpha \frac{\partial(\nabla \cdot \mathbf{u})}{\partial t} + S_\epsilon \frac{\partial(P^{ex})}{\partial t} - c \nabla^2 P^{ex} &= 0 \end{aligned} \quad (2.48)$$

where the diffusivity (Rudnicki, 1986) is:

$$c = \left\{ \frac{\kappa (\lambda_u - \lambda) (\lambda_u + 2\mu)}{\eta \alpha^2 (\lambda_u + 2\mu)} \right\} \quad (2.49)$$

with the corresponding boundary conditions.

Let Ω be the physical domain and $\partial\Omega$ the boundary of Ω . It can be separated into $\partial\Omega_{diffusion}$ and $\partial\Omega_{elasticity}$:

$$\begin{aligned} \partial\Omega_{elasticity} &= \partial\Gamma_u + \partial\Gamma_{\sigma_t} \\ \partial\Omega_{diffusion} &= \partial\Gamma_{p^{ex}} + \partial\Gamma_q \end{aligned} \quad (2.50)$$

where $\partial\Gamma_u$ is the displacement boundary, $\partial\Gamma_{\sigma_t}$ is the total stress or traction boundary, $\partial\Gamma_P$ is the excess pore pressure boundary, and $\partial\Gamma_q$ is the fluid flux boundary. The displacement boundary condition is

$$\mathbf{u} = \bar{\mathbf{u}} \quad \text{on } \partial\Gamma_u \quad (2.51)$$

where $\bar{\mathbf{u}}$ is the prescribed displacement on surface. The total stress or traction boundary condition on $\partial\Gamma_{\sigma_t}$ is:

$$\sigma_t \cdot \mathbf{n} = \bar{\mathbf{t}} \quad \text{on } \partial\Gamma_{\sigma_t} \quad (2.52)$$

where $\bar{\mathbf{t}}$ denotes the prescribed tractions on one surface and \mathbf{n} denotes the unit normal vector. The excess pore pressure boundary condition is:

$$P^{ex} = \overline{P^{ex}} \quad \text{on} \quad \partial\Gamma_{P^{ex}} \quad (2.53)$$

where $\overline{P^{ex}}$ denotes the prescribed excess pore pressure on surfaces. The fluid flux boundary condition is:

$$-\left(\frac{\kappa}{\eta} \nabla \cdot P^{ex}\right) \cdot \mathbf{n} = \bar{\mathbf{q}} \quad \text{on} \quad \partial\Gamma_q \quad (2.54)$$

where $\bar{\mathbf{q}}$ denotes the prescribed flow normal to surface $\partial\Gamma_q$.

Initial conditions are given in terms of pressure and total stress by:

$$\begin{aligned} P^{ex} &= P_0^{ex} \quad \text{on} \quad \Omega \quad \text{at} \quad t = 0 \\ \sigma_t &= \sigma_{t0} \quad \text{on} \quad \Omega \quad \text{at} \quad t = 0 \end{aligned} \quad (2.55)$$

2.2.5 Dimensionless Strong Formulation

In this section dimensionless forms of poroelasticity are presented to exploit and obtain more general results in the following sections.

Dimensionless Analysis by Using the Pi Theorem

The Buckingham π theorem is key in dimensional analysis. It is the formalization of Rayleigh's method of dimensional analysis. The theorem states that if we have a physically meaningful equation involving a certain number n of physical variables, and these variables are expressible in terms of k independent fundamental physical quantities, then the original expression is equivalent to an equation involving a set of $r = n - k$ dimensionless parameters constructed from the original variables: rewriting the equations in a non-dimensional form. It provides a method for computing sets of dimensionless parameters from the given variables, even if the form of the equation is still unknown. However, the choice of dimensionless parameters is not unique, Buckingham's theorem only provides a way of generating sets of dimensionless parameters, and will not choose the most physically meaningful set (Wong, 1990). Combined with inspection analysis this procedure allows the choice of important quantities that represent the fundamental behavior of one phenomenon.

Using the procedure in Wong (1990), the poroelastic coupled system described by (2.48) with boundary and initial conditions: (2.51), (2.52), (2.53), (2.54), (2.55), are transformed

by the dimensionless group presented in table 2.1 as:

$$\begin{aligned} (\lambda_D + \mu_D) \nabla (\nabla \cdot \mathbf{u}_D) + \mu_D \nabla^2 \mathbf{u}_D - \alpha \nabla P_D^{ex} + \mathbf{b}_D &= 0 \\ \alpha \frac{\partial (\nabla \cdot \mathbf{u}_D)}{\partial t_D} + Sr_D \frac{\partial (P_D^{ex})}{\partial t_D} - \nabla^2 P_D^{ex} &= 0 \end{aligned} \quad (2.56)$$

Table 2.1: Group of dimensionless variables. Left) Incompressible fluid constituent case. Right) Compressible fluid constituent case.

Incompressible	Definition	Compressible	Definition
\mathbf{u}_D	$\frac{\mathbf{u}}{L P_0^{ex}} \frac{(\lambda+2\mu)}{\alpha^2}$	\mathbf{u}_D	$\frac{\mathbf{u}}{L P_0^{ex}} \frac{(\lambda_u-\lambda)}{\alpha^2} \frac{(\lambda+2\mu)}{(\lambda_u+2\mu)}$
λ_D	$\lambda \frac{\alpha^2}{(\lambda+2\mu)}$	λ_D	$\lambda \frac{\alpha^2}{(\lambda_u-\lambda)} \frac{(\lambda_u+2\mu)}{(\lambda+2\mu)}$
μ_D	$\mu \frac{\alpha^2}{(\lambda+2\mu)}$	μ_D	$\mu \frac{\alpha^2}{(\lambda_u-\lambda)} \frac{(\lambda_u+2\mu)}{(\lambda+2\mu)}$
Sr_D	0	Sr_D	$\frac{(\lambda+2\mu)}{(\lambda_u+2\mu)}$
σ_{tD}	$\frac{\sigma_t}{P_0^{ex}}$	σ_{tD}	$\frac{\sigma_t}{P_0^{ex}}$
\mathbf{b}_D	$\mathbf{b} \frac{L}{P_0^{ex}}$	\mathbf{b}_D	$\mathbf{b} \frac{L}{P_0^{ex}}$
P_D^{ex}	$\frac{P_0^{ex}}{P_0^{ex}}$	P_D^{ex}	$\frac{P_0^{ex}}{P_0^{ex}}$
\mathbf{q}_D	$\mathbf{q} \frac{\eta}{\kappa} \frac{L}{\rho_{0fluid} P_0^{ex}}$	\mathbf{q}_D	$\mathbf{q} \frac{\eta}{\kappa} \frac{L}{\rho_{0fluid} P_0^{ex}}$
\mathbf{v}_D	$\mathbf{v} \frac{\eta}{\kappa} \frac{L}{P_0^{ex}}$	\mathbf{v}_D	$\mathbf{v} \frac{\eta}{\kappa} \frac{L}{P_0^{ex}}$
x_D	$\frac{x}{L}$	x_D	$\frac{x}{L}$
t_D	$t \frac{c}{L^2}$	t_D	$t \frac{c}{L^2}$

where $Sr_D = \frac{S_\epsilon}{S}$ with $S_\epsilon < S$, is analog to relative fluid compressibilities at different constraints conditions (Wang, 2000). Using the above relations the constitutive equations take the forms:

Linearly elasticity:

$$\nabla \cdot \sigma_{tD} + \mathbf{b}_D = 0 \quad (2.57)$$

$$\sigma_{tD} = \mu_D (\nabla \mathbf{u}_D + \nabla^T \mathbf{u}_D) + \lambda_D (\nabla \cdot \mathbf{u}_D) \mathbf{I} - \alpha P_D^{ex} \mathbf{I} \quad (2.58)$$

The fluid mass content per unit of porous solid:

$$\phi_D^* - \phi_{oD}^* = (\alpha \nabla \cdot \mathbf{u}_D + Sr_D P_D^{ex}) \quad (2.59)$$

Darcy's law:

$$\mathbf{q}_D = -\nabla P_D^{ex} \quad (2.60)$$

The equation of fluid mass conservation:

$$\nabla \cdot \mathbf{q}_D + \frac{\partial \phi_D^*}{\partial t} = 0 \quad (2.61)$$

The displacement boundary condition:

$$\mathbf{u}_D = \bar{\mathbf{u}}_D \quad \text{on} \quad \partial\Gamma_{u_D} \quad (2.62)$$

The total stress or traction boundary condition on $\partial\Gamma_{\sigma_{tD}}$:

$$\sigma_{tD} \cdot \mathbf{n} = \bar{\mathbf{t}}_D \quad \text{on} \quad \partial\Gamma_{\sigma_{tD}} \quad (2.63)$$

The excess pore pressure boundary condition:

$$P_D^{ex} = \bar{P}_D^{ex} \quad \text{on} \quad \partial\Gamma_{P_D^{ex}} \quad (2.64)$$

The fluid flux boundary condition:

$$-(\nabla \cdot P_D^{ex}) \cdot \mathbf{n} = \bar{\mathbf{v}}_D \quad \text{on} \quad \partial\Gamma_{v_D} \quad (2.65)$$

Initial conditions are given in terms of pressure and total stress:

$$\begin{aligned} P_D^{ex} &= P_{0D}^{ex} \quad \text{on} \quad \Omega \quad \text{at} \quad t_D = 0 \\ \sigma_{tD} &= \sigma_{t0D} \quad \text{on} \quad \Omega \quad \text{at} \quad t_D = 0 \end{aligned} \quad (2.66)$$

There are a variety of dimensionless numbers published in petroleum literature and, based on the flow system, they can be divided in two groups: single-phase and two-phase systems. Normally, single-phase systems are used in well test analysis where inspection analysis enables the transformation into dimensionless space for any given set of given boundary conditions. For two-phase systems, Lake (1990) presents a general method to scale flow through heterogeneous permeable media for an immiscible displacement of oil by water in a two-dimensional, anisotropic, heterogeneous cross section with statistically stationary properties. Gharbi (2002) established a foundation for scaling miscible displacement in three-dimensional reservoirs. These examples illustrate how dimensional forms allow the understanding of essential mechanisms and present the results in a compact form.

2.3 Fault Reactivation according to the inclusion theory

Geological discontinuities such as faults are inherent in most petroleum formations. There are a number of human activities, such as hydrocarbon production, that can sufficiently

alter the in-situ stresses within a period of a few years or even a few months resulting in reactivation and slip of the nearby faults (Hawkes, 2009). Fault reactivation due to reservoir depletion may have various consequences ranging from shearing boreholes drilled to inducing seismicity on faulted zones. Stress state perturbation resulting from subsurface fluid extraction clearly and robustly demonstrates the importance of considering the poroelastic effect. The increasing number of induced seismicity and well damages initiated great interest in studying the mechanics of fault reactivation, ground subsidence, reservoir deformation, and in-situ stress changes caused by fluid withdrawal (Germanovich, 2004). In most cases the reservoir has been treated as a partially drained poroelastic inclusion surrounded by an elastic host material. Usually to solve this problem in the literature, three approaches can be considered:

1. The reservoir is modelled by an inclusion with a rather arbitrary pore pressure distribution but with the same material properties as the surrounding rock matrix.
2. The reservoir is modelled as a uniformly pressurized homogeneous ellipsoidal inclusion with different material properties compared to the surrounding rock.
3. Numerical approximations as: finite difference, finite elements, or boundary elements procedures, are used to model the phenomenon.

The first approach is based on a homogeneous formation and accounts for the main reason for stress redistribution around depleted reservoirs, *i.e.*, a change in the reservoir pore pressure. The second approach, utilizing an ellipsoidal inclusion, accounts for another important factor of material inhomogeneity, but considers uniform pressure distribution inside the reservoir.

The third approach, used in this work, is relatively flexible, but when modeling large domains with complex geometries, unreliable solutions can be obtained if conventional numeric techniques are used. In addition, with numerical modeling, it is possible to calculate different material contrast and different production programs. Using the suggested implementation, the challenge is to obtain a reasonable approximation without extreme refinements and large simulations times.

2.3.1 Main assumptions

The following simplifying assumptions are made for the semi-analytical approach given in Hawkes (2009) and Germanovich (2004):

1. Plane strain conditions. This means the third normal stress is expressed as function of the other ones and pore pressure excess.

2. The reservoir can interact with the earth surface, having the same elastic moduli as side burden rocks.
3. Side burden rocks are under the drained limit.
4. Linear poroelastic behavior of reservoir and side burden rocks.
5. The initial in-situ stress state is known.
6. Ideal cohesion on the reservoir boundaries.
7. Fault gouge obeys the Mohr-Coulomb failure criterion.
8. Thin pre-existing faults. Mechanically, faults don't exist, they represent potential slip surfaces.

Note that, before the onset of slip, the presence of the fault does not affect the stress state around the reservoir. In this respect, mechanically, the fault does not exist before the slip initiates and only represents a potential slip surface rather than a displacement discontinuity affecting the state of stress.

2.3.2 Theoretical concepts

An inclusion is defined as a sub-domain Ω in domain D , where the arbitrary strains referred as eigenstrain $\epsilon^*(\mathbf{x})$ (Mura, 1982; Hawkes, 2009) is given in Ω and is zero in $D - \Omega$, this strain field can be thought as internal strains that would be caused by different mechanisms, including poroelastic, poroelastoplastic and thermal changes in a unbounded body free of external forces and surface constraints. The elastic moduli in Ω and $D - \Omega$ are the same, assumption (2). The remaining domain $D - \Omega$ is called the elastic matrix. In his well-known papers on this subject, Eshelby (1957) showed that the inclusion problem is equivalent to solving equations of elastic equilibrium for a homogeneous body with a known body force distribution. For such bodies, the equations of elastic equilibrium are solved using the elastic static Green functions (Mura, 1982).

The Green function $\mathbf{G}(\mathbf{x}, \mathbf{x}')$ gives the magnitude of the displacement in the \mathbf{x}_i direction at point x when a unit body force in the \mathbf{x}_j direction is applied at point x' to an elastic medium under plane strain conditions into half space assumption (1), (2), (3) and (4). In the Green function method, the displacement \mathbf{u} and stress field σ due to eigenstrain $\epsilon^*(\mathbf{x})$ in the inclusion is given as:

$$\mathbf{u} = \oint_{\Omega} C_{jlmn} \epsilon_{mn}^*(\mathbf{x}') \mathbf{G}_{ij,l}(\mathbf{x} - \mathbf{x}') d\mathbf{x}' \quad (2.67)$$

$$\epsilon = -\frac{1}{2} \oint_{\Omega} C_{jlmn} \epsilon_{mn}^* (\mathbf{x}') \{ \mathbf{G}_{ik,lj} (\mathbf{x} - \mathbf{x}') + \mathbf{G}_{jk,li} (\mathbf{x} - \mathbf{x}') \} d\mathbf{x}' \quad (2.68)$$

$$\sigma (\mathbf{x}) = -C_{ijkl} \left\{ \oint_{\Omega} C_{pqmn} \epsilon_{mn}^* (\mathbf{x}') \mathbf{G}_{kp,ql} (\mathbf{x} - \mathbf{x}') d\mathbf{x}' + \epsilon_{kl}^* (\mathbf{x}') \right\} \quad (2.69)$$

where $\epsilon^* (\mathbf{x}) = 0$ for $\mathbf{x} \in D - \Omega$, $C_{ijkl} = \lambda \delta_{ij} \delta_{kl} + \mu (\delta_{ik} \delta_{jl} + \delta_{il} \delta_{jk})$.

Since $\epsilon^* (\mathbf{x})$ is discontinuous on the boundary of the inclusion $\partial\Omega$, some quantities may also be discontinuous on the boundary. However the displacement and the inter-facial tractions across the boundary must be continuous, *i.e.* assumption (6) that is:

$$\Delta \mathbf{u}_{\partial\Omega} = \mathbf{u}_{out} - \mathbf{u}_{in} \quad (2.70)$$

$$\Delta \sigma_{\partial\Omega} \cdot \mathbf{n} = \{ \sigma_{out} - \sigma_{in} \} \cdot \mathbf{n} \quad (2.71)$$

Eshelby (1957) showed that, for an ellipsoidal inclusion in a full-space, the strain and stress field are uniform for all interior points. In the case of dilatational eigenstrain (*i.e.*, the tendency of the inclusion would be to expand or contract isotropically, as would be the case for poroelastic or thermoelastic strains in an isotropic medium), $\epsilon^* (\mathbf{x}) = \epsilon^C (\mathbf{x}) I$, with I representing the identity matrix, thus equations 2.67, 2.68 and 2.69 are reduced to:

$$\mathbf{u} (\mathbf{x}) = - (2\mu + 3\lambda) \oint_{\Omega} \epsilon^C (\mathbf{x}') \mathbf{G}_i^D (\mathbf{x}, \mathbf{x}') d\mathbf{x}' \quad (2.72)$$

$$\epsilon (\mathbf{x}) = -\frac{1}{2} (2\mu + 3\lambda) \oint_{\Omega} \epsilon^C (\mathbf{x}') \{ \mathbf{G}_{ik,lj} (\mathbf{x} - \mathbf{x}') + \mathbf{G}_{jk,li} (\mathbf{x} - \mathbf{x}') \} d\mathbf{x}' \quad (2.73)$$

$$\sigma (\mathbf{x}) = - (2\mu + 3\lambda) \oint_{\Omega} \epsilon^C (\mathbf{x}') \mathbf{G}_{ij}^S (\mathbf{x}, \mathbf{x}') d\mathbf{x}' + \sigma^* (\mathbf{x}') \quad (2.74)$$

where $\sigma^* (\mathbf{x}) = (2\mu + 3\lambda) \delta_{ij} \epsilon^C (\mathbf{x})$ is the eigenstress at point x , and $\mathbf{G}_i^D (\mathbf{x}, \mathbf{x}') = \mathbf{G}_{ij,l} (\mathbf{x} - \mathbf{x}')$ and $\mathbf{G}_{ij}^S (\mathbf{x}, \mathbf{x}') = \mu (\mathbf{G}_{ip,pj} (\mathbf{x} - \mathbf{x}') + \mathbf{G}_{jp,pi} (\mathbf{x} - \mathbf{x}')) + \lambda (\mathbf{G}_{kp,pk} (\mathbf{x} - \mathbf{x}')) \delta_{ij}$ respectively, are influence and stress functions for dilatation (Segall, 1987; Hawkes, 2009).

It is possible to consider a reservoir as an inclusion if it has the same material properties as the surrounding rock, and the eigenstrains are defined as the dilatational strains that would be caused by changes in pore pressure excess ΔP^{ex} or temperature ΔT inside the reservoir if it was unbounded. The values of dilatational eigenstrain for these conditions, respectively, are:

$$\epsilon^C (\mathbf{x}) = \frac{1}{3} \left(\frac{\alpha \Delta P^{ex} (\mathbf{x})}{K_u} \right) = \frac{\alpha \Delta P^{ex} (\mathbf{x})}{(2\mu + 3\lambda)} \quad (2.75)$$

$$\epsilon^C(\mathbf{x}) = \beta \Delta T(\mathbf{x}) \quad (2.76)$$

where K_u is the undrained bulk modulus and β is the linear coefficient of thermal expansion.

The treatment of a reservoir as an inclusion also requires the assumption that no pressure or temperature change occurs in the surrounding rocks; *i.e.*, there is no hydraulically driven flow, no heat transfer, and fully drained loading occurs. Inclusion theory allows the consideration of reservoirs of arbitrary shape. A useful result of the treatment of the dimensionless equations is the possibility to use LPA in linear thermal stress calculations, since in the dimensionless form of poroelastic and thermoelastic equations are mathematically equal.

2.3.3 Assessment of fault reactivation

Stress arching ratios

The ratio of the change in total stress to the change in pore pressure within the reservoir has been referred to as the stress arching ratio. Normalized stress arching ratios are defined by Hawkes (2009) and are slightly more generalized for poroelastic analysis, since they results from the stresses and homogeneous excess pore pressure change combination, and are expressed as follows:

$$\gamma = \frac{\Delta \sigma}{\alpha \Delta P^{ex}} \quad (2.77)$$

when γ and ΔP^{ex} are defined σ is directly determine using 2.77.

Coulomb failure stress change ΔCFS

The Coulomb Failure Stress (CFS) is defined as follows :

$$CFS = \tau - \mu_s \sigma_n \quad (2.78)$$

where τ and σ_n respectively are, shear and effective normal stress on the fault plane, μ_s is the coefficient of friction in the fault plane (*i.e.*, the tangent of the fault friction angle normally between $0.4 < \mu_s < 0.8$ for several brittle rocks (Hawkes, 2009)). A fault plane is activated when CFS is equal to or greater than zero. In a production or injection scenario, where in stress changes have been induced, the change in CFS is:

$$\Delta CFS = \Delta \tau - \mu_s \Delta \sigma_n \quad (2.79)$$

The sign of $\Delta\tau$ is positive when it points in the same direction as the initial shear stress on the plane. The sign of $\Delta\sigma_n$ is negative for an increase in compressive stress. As such, a positive ΔCFS indicates a tendency towards fault reactivation. Earthquake-induced ΔCFS values as small as 0.1 MPa have been found to induce seismic activity in faulted settings evidencing fault reactivation where initial CFS values are close to zero (Segall, 1992; Guyot and Volant, 1992; Rudnicki, 1999; Ferronato, 2008; Hawkes, 2009). In order to achieve a more general, dimensionless characterization of fault reactivation risk, a parameter called fault reactivation factor Hawkes (2009) is defined here as follows:

$$\lambda_{FR} = \frac{\Delta CFS}{\alpha \Delta P^{ex}} = \frac{\Delta\tau}{\alpha \Delta P^{ex}} - \mu_s \frac{\Delta\sigma_n}{\alpha \Delta P^{ex}} = \frac{\Delta\gamma_{shear}}{\alpha \Delta P^{ex}} - \mu_s \frac{\Delta\gamma_n}{\alpha \Delta P^{ex}} \quad (2.80)$$

Fault Reactivation calculations

Following Hawkes (2009), effective stress changes or normalized stress arching ratios can be calculated as follow:

- Given a ΔP^{ex} calculate σ using the equation 2.74.
- Calculate γ and λ_{FR} over a fault plane (straight lines in this work) by applying a stress rotation over required angles.
- Using the sing of λ_{FR} convention, evaluate which planes are reactivated.

To define fault reactivation calculation, it is necessary to solve the normal and shear stress or arching ratios along fault plane inclined θ degrees counter-clockwise from x axis, then calculate λ_{FR} or ΔCFS to define the tendency to reactivate. The reactivation is given for the sign convention in table 2.2

Table 2.2: Fault reactivation tendency sign convention. Opposite case tendency to stabilization. Left) Used for normalized arching ratios (Hawkes, 2009; Germanovich, 2004). Right) Direct form of ΔCFS . Used for LPA computations. In both cases τ sign is inverted for reverse faulting.

λ_{FR}	$\Delta P^{ex} < 0$	$\Delta P^{ex} > 0$	ΔCFS	<i>sign</i>	τ
Normal faulting	$\lambda_{FR} < 0$	$\lambda_{FR} > 0$	Normal faulting	$\Delta CFS > 0$	$\tau > 0$
Reverse faulting			Reverse faulting		$\tau < 0$

2.4 Summary

In this chapter, a displacement-pressure (also called u - p formulation) mono phasic and dimensionless poroelastic formulation was presented. The basic assumptions and constitutive relations of the continuum theory were described. The governing equations consist of the balance of mass equations and the balance of momentum equations for each phase. Detailed derivations of these governing equations were presented. The equations finally became a mono phasic poroelastic system used for subsequent analyses. Also, mathematical approximation of fault reactivation is given by means of inclusion theory, a formulation that is going to be used in chapter 5 to compare against LAP calculations.

3. Continuous Galerkin Formulation

3.1 Weak Formulation

Abstract spaces and bilinear forms

Here are defined some function spaces and bilinear forms for variational and finite element formulations:

$L^2(\Omega)$: Hilbert space of square integrable scalar valued functions defined in Ω . Its inner product is defined as

$$(f_1, f_2) = \int_{\Omega} f_1 \cdot f_2 d\Omega \quad (3.1)$$

and the corresponding norm is

$$\|f\|_{L^2} = (f, f)^{\frac{1}{2}} \quad (3.2)$$

$D^{|\zeta|}(\Omega)$: partial derivatives of function f with order $\zeta = (\zeta_1, \zeta_2, \dots, \zeta_n)$. This definition is detailed in some applied mathematics books *e.g.* Greenberg (1978) as

$$D^{|\zeta|}(\Omega) = \frac{\partial}{\partial x_1^{\zeta_1} \partial x_2^{\zeta_2} \dots \partial x_n^{\zeta_n}} (f_1, f_2)^{\frac{1}{2}} \quad (3.3)$$

with

$$|\zeta| = \zeta_1 + \zeta_2 + \dots + \zeta_n \quad (3.4)$$

where $n = 2$ or 3

$H^m(\Omega)$: Hilbert space of order m , with definition

$$H^m(\Omega) = \left\{ f \in L^2(\Omega), \forall |\zeta| \leq m, D^{|\zeta|} f \in L^2(\Omega) \right\} \quad (3.5)$$

with norm

$$\|f\|_m = \left(\sum_{|\zeta| \leq m} \|D^{|\zeta|} f\|_{L^2(\Omega)}^2 \right)^{\frac{1}{2}} \quad (3.6)$$

and semi-norm

$$|f|_m = \|\partial^m f\|_{L^2(\Omega)} \quad (3.7)$$

$H_0^1(\Omega)$: Hilbert space of order 1, with definition

$$H_0^1(\Omega) = \{f \in H^1(\Omega), f = 0 \text{ on } \partial\Omega\} \quad (3.8)$$

let's define the base function spaces to approximate each state variable

V : function space of displacement field \mathbf{u} , defined by

$$V = \{f \in H^1(\Omega), f = u_D \text{ on } \partial\Omega_1\} \quad (3.9)$$

W : function space of excess pore pressure field, defined by

$$W = \{f \in H^1(\Omega), f = P_D^{ex} \text{ on } \partial\Omega_2\} \quad (3.10)$$

$V_h^{r^1}$: continuous piecewise polynomial finite element space of V with degree r^1 $W_h^{r^2}$: continuous piecewise polynomial finite element space of W with degree r^2

Please note from the above definitions in this implementation that is possible to have a arbitrary polynomial orders.

$a(\mathbf{u}, \mathbf{v})$: bilinear form on V corresponding to the elasticity equation defined by

$$a(u, v) = \int_{\Omega} \{\lambda (\nabla \cdot \mathbf{u}) (\nabla \cdot \mathbf{v}) + 2\mu \epsilon(\mathbf{u}) \cdot \epsilon(\mathbf{v})\} d\Omega \quad (3.11)$$

$$a(u, v) = \int_{\Omega} \left\{ \lambda (\nabla \cdot \mathbf{u}) (\nabla \cdot \mathbf{v}) + 2\mu \left(\frac{1}{2} (\nabla \mathbf{u} + \nabla^T \mathbf{u}) \right) \cdot \left(\frac{1}{2} (\nabla \mathbf{v} + \nabla^T \mathbf{v}) \right) \right\} d\Omega \quad (3.12)$$

$b(u, v)$: bilinear form on W corresponding to the diffusion equation defined by

$$b(u, v) = \int_{\Omega} \rho \frac{\kappa}{\mu} \nabla u \cdot \nabla v d\Omega \quad (3.13)$$

Please note that the constitutive bilinear form depend on the constitutive material behavior *i.e.* a linear poroelastic material composed by linear elasticity and Darcy's law

$\|\mathbf{u}\|_{E_a}$: energy norm related to elasticity defined by

$$\|\mathbf{u}\| = \{a(\mathbf{u}, \mathbf{u})\}^{\frac{1}{2}} \quad (3.14)$$

$\|P^{ex}\|_{E_b}$: energy norm related to diffusion problem defined by

$$\|P^{ex}\|_{E_b} = \{b(P^{ex}, P^{ex})\}^{\frac{1}{2}} \quad (3.15)$$

3.2 Variational formulation

Based on the strong formulation of poroelasticity defined in 2.56, and corresponding initial and boundary conditions, the weak statement for this work is obtained with the follow steps:

1. Multiply by admissible members of V for equilibrium equation and W for the mass conservation equation. These members contract the equations to a scalar.
2. Integrate these equations over all the domain Ω .
3. Apply the divergence theorem in order to progressively weaken the smoothness requirements of the strong solution.
4. Insert the corresponding constitutive equations, in this case the linear elasticity and Darcy's law.
5. Finally rewrite the weak statements in terms of the bilinear forms already defined.

3.2.1 Mass conservation equation

By multiplying the mass conservation equation by $w \in W$ and integrating over all spatial domain, the following equation is obtained

$$\int_{\Omega} \left(\frac{\partial \phi_D^*}{\partial t} + \nabla \cdot \mathbf{q}_D \right) w \, \partial\Omega = 0 \, \partial\Omega \quad (3.16)$$

Green's Theorem states that:

$$\int_{\Omega} (\nabla \cdot \eta) \, \partial\Omega = \int_{\Gamma} (\eta \cdot \mathbf{n}) \, \partial\Gamma \quad (3.17)$$

where η is a vectorial function, it can be expressed as the product of two functions $\eta = u\mathbf{v}$, and the last expression becomes

$$\int_{\Omega} (\nabla \cdot (u\mathbf{v})) \partial\Omega = \int_{\Gamma} ((u\mathbf{v}) \cdot \mathbf{n}) \partial\Gamma \quad (3.18)$$

the left hand side expands to give:

$$\int_{\Omega} (u\nabla \cdot \mathbf{v} + \mathbf{v} \cdot \nabla u) \partial\Omega = \int_{\Gamma} (u\mathbf{v} \cdot \mathbf{n}) \partial\Gamma \quad (3.19)$$

this is an integration by parts; thus using this correspondences $u \implies w$ and $\mathbf{v} \implies \bar{\mathbf{v}}_o$ into $\int_{\Omega} (\nabla \cdot \rho_o \bar{\mathbf{v}}_o) w \partial\Omega$ result in

$$\int_{\Omega} (\nabla \cdot \mathbf{q}_D) w \partial\Omega = - \int_{\Omega} (\mathbf{q}_D) \cdot \nabla w + \int_{\Gamma} (w (\mathbf{q}_D) \cdot \mathbf{n}) \partial\Gamma \quad (3.20)$$

inserting this results in 3.16

$$\int_{\Omega} \left(\frac{\partial \phi_D^*}{\partial t} \right) w \partial\Omega - \int_{\Omega} (\mathbf{q}_D \cdot \nabla w) \partial\Omega + \int_{\Gamma} (w (\mathbf{q}_D) \cdot \mathbf{n}) \partial\Gamma = 0 \quad (3.21)$$

Introducing $q_{D \text{ normal}} = (\mathbf{q}_D) \cdot \mathbf{n}$, the boundary term may be split into two parts and expressed as

$$\int_{\Gamma} w q_{D \text{ normal}} \partial\Gamma = \int_{\Gamma_{\text{Dirichlet}}} w q_{D \text{ normal}} \partial\Gamma + \int_{\Gamma_{\text{Neuman}}} w q_{D \text{ normal}} \partial\Gamma \quad (3.22)$$

without any loss of generality, let's set w to zero only over $\Gamma_{\text{Dirichlet}}$. Substituting in 3.21 the final expression is

$$\int_{\Omega} \left(\frac{\partial \phi_D^*}{\partial t} \right) w \partial\Omega - \int_{\Omega} (\mathbf{q}_D) \cdot \nabla w + \int_{\Gamma_{\text{Neuman}}} w q_{D \text{ normal}} \partial\Gamma = 0 \quad (3.23)$$

inserting equation 2.60 into 3.23

$$\int_{\Omega} \left(\frac{\partial \phi_D^*}{\partial t} \right) w \partial\Omega + \int_{\Omega} (\nabla P_D^{ex}) \cdot \nabla w + \int_{\Gamma_{\text{Neuman}}} w q_{D \text{ normal}} \partial\Gamma = 0 \quad (3.24)$$

Please note that the above form only involves first derivatives of quantities instead of the second derivatives in the original differential equation. This leads to weaker conditions to define the solutions to this problem and thus the notion of a weak form is established.

3.2.2 Equilibrium Equation

By multiplying the equilibrium equation 2.57 by $\mathbf{v} = v_1 \mathbf{e}_1 + v_2 \mathbf{e}_2$ with $\mathbf{v} \in V$ and integrating over all spatial domain, the following equation is obtained

$$\int_{\Omega} (\nabla \cdot \sigma_{tD} + \mathbf{b}_D) \cdot \mathbf{v} \, d\Omega = 0 \quad (3.25)$$

$$\int_{\Omega} (\nabla \cdot \sigma_{tD}) \cdot \mathbf{v} \, d\Omega + \int_{\Omega} \mathbf{b}_D \cdot \mathbf{v} \, d\Omega = 0 \quad (3.26)$$

Considering the divergence theorem applied to vectorial quantity as the dot product of the total stress tensor σ_{tD} and the trial or test function \mathbf{v} , $\sigma_{tD} \cdot \mathbf{v}$ and knowing $\nabla \cdot (\mathbf{S}^T \mathbf{v}) = \mathbf{S} \cdot \nabla \mathbf{v} + \mathbf{v} \cdot \nabla \cdot (\mathbf{S})$ (Gurtin, 1981) the following results in:

$$\int_{\Omega} \nabla \cdot (\sigma_{tD} \cdot \mathbf{v}) \, d\Omega = \int_{\Gamma} (\sigma_{tD} \cdot \mathbf{v}) \cdot \mathbf{n} \, \partial\Gamma \quad (3.27)$$

knowing that σ_{tD} is a symmetric tensor, by expanding the left-hand side, the result is:

$$\int_{\Omega} \sigma_{tD} \cdot \nabla \mathbf{v} \, d\Omega + \int_{\Omega} \mathbf{v} \cdot \nabla \cdot \sigma_{tD} \, d\Omega = \int_{\Gamma} (\sigma_{tD} \cdot \mathbf{v}) \cdot \mathbf{n} \, \partial\Gamma = 0 \quad (3.28)$$

$$\int_{\Omega} \sigma_{tD} \cdot \nabla \mathbf{v} \, d\Omega + \int_{\Omega} \nabla \cdot \sigma_{tD} \cdot \mathbf{v} \, d\Omega = \int_{\Gamma} (\sigma_{tD} \cdot \mathbf{v}) \cdot \mathbf{n} \, \partial\Gamma = 0 \quad (3.29)$$

$$\int_{\Omega} \nabla \cdot \sigma_{tD} \cdot \mathbf{v} \, d\Omega = - \int_{\Omega} \sigma_{tD} \cdot \nabla \mathbf{v} \, d\Omega + \int_{\Gamma} (\sigma_{tD} \cdot \mathbf{n}) \cdot \mathbf{v} \, \partial\Gamma \quad (3.30)$$

By substituting in the weak form, the result is

$$- \int_{\Omega} \sigma_{tD} \cdot \nabla \mathbf{v} \, d\Omega + \int_{\Gamma} (\sigma_{tD} \cdot \mathbf{n}) \cdot \mathbf{v} \, \partial\Gamma + \int_{\Omega} \mathbf{b}_D \cdot \mathbf{v} \, d\Omega = 0 \quad (3.31)$$

By separating the integration over Γ into integrations surface domains the action of surface tractions over the boundary Γ_{Neuman} and with displacement conditions over the remaining boundary $\Gamma_{Dirichlet}$

$$- \int_{\Omega} \sigma_{tD} \cdot \nabla \mathbf{v} \, d\Omega + \int_{\Gamma_{Neuman}} (\sigma_{tD} \cdot \mathbf{n}) \cdot \mathbf{v} \, \partial\Gamma + \int_{\Gamma_{Dirichlet}} (\sigma_{tD} \cdot \mathbf{n}) \cdot \mathbf{v} \, \partial\Gamma + \int_{\Omega} \mathbf{b}_D \cdot \mathbf{v} \, d\Omega = 0 \quad (3.32)$$

recognizing that $\mathbf{v} = 0$ on $\Gamma_{Dirichlet}$

$$\int_{\Gamma_{Neuman}} (\sigma_{tD} \cdot \mathbf{n}) \cdot \mathbf{v} \, \partial\Gamma = \int_{\Gamma_{Neuman}} T_{nD} \cdot \mathbf{v} \, \partial\Gamma \quad (3.33)$$

$$-\int_{\Omega} (\sigma_{tD} \cdot \nabla \mathbf{v}) d\Omega + \int_{\Gamma_{Neuman}} (\sigma_{tD} \cdot \mathbf{n}) \cdot \mathbf{v} \partial\Gamma + \int_{\Omega} \mathbf{b}_D \cdot \mathbf{v} d\Omega = 0 \quad (3.34)$$

and please note that since the stress is symmetric

$$\begin{aligned} \sigma_{tD} \cdot \nabla \mathbf{v} &= \frac{1}{2} (\sigma_{tD} + \sigma_{tD}^T) \cdot \nabla \mathbf{v} \\ &= \frac{1}{2} (\sigma_{tD}) \cdot \nabla \mathbf{v} + \frac{1}{2} (\sigma_{tD}^T) \cdot \nabla \mathbf{v} \\ &= \frac{1}{2} (\sigma_{tD}) \cdot \nabla \mathbf{v} + \frac{1}{2} (\sigma_{tD}) \cdot \nabla^T \mathbf{v} \\ &= \sigma_{tD} \cdot \left(\frac{1}{2} (\nabla \mathbf{v} + \nabla^T \mathbf{v}) \right) \\ &= \sigma_{tD} \cdot \epsilon(\mathbf{v}) \end{aligned} \quad (3.35)$$

it means

$$-\int_{\Omega} \sigma_{tD} \cdot \epsilon(\mathbf{v}) d\Omega + \int_{\Gamma_{Neuman}} (\sigma_{tD} \cdot \mathbf{n}) \cdot \mathbf{v} \partial\Gamma + \int_{\Omega} \mathbf{b}_D \cdot \mathbf{v} d\Omega = 0 \quad (3.36)$$

by inserting the linear elastic constitutive equation

$$-\int_{\Omega} (\lambda_D (\nabla \cdot \mathbf{u}_D) + 2\mu_D \epsilon(\mathbf{u}_D)) \cdot \epsilon(\mathbf{v}) d\Omega + \int_{\Gamma_{Neuman}} (\sigma_{tD} \cdot \mathbf{n}) \cdot \mathbf{v} \partial\Gamma + \int_{\Omega} \mathbf{b}_D \cdot \mathbf{v} d\Omega = 0 \quad (3.37)$$

by inserting the linear poroelastic constitutive equation

$$\begin{aligned} -\int_{\Omega} (\lambda_D (\nabla \cdot \mathbf{u}_D) + 2\mu_D \epsilon(\mathbf{u}_D)) \cdot \epsilon(\mathbf{v}) d\Omega + \int_{\Omega} (\alpha (P_D^{ex}) I \cdot \nabla \mathbf{v}) d\Omega \\ + \int_{\Gamma_{Neuman}} (\sigma_{tD} \cdot \mathbf{n}) \cdot \mathbf{v} \partial\Gamma + \int_{\Omega} \mathbf{b}_D \cdot \mathbf{v} d\Omega = 0 \end{aligned} \quad (3.38)$$

3.3 Bilinear Forms

In terms of bilinear forms the previously defined equations 3.24 and 3.38 become

$$\left(\alpha \frac{\partial (\nabla \cdot \mathbf{u}_D)}{\partial t_D}, w \right) + \left(S r_D \frac{\partial (P_D^{ex})}{\partial t_D}, w \right) + b(P_D^{ex}, w) = \hat{q}_D(w) \quad (3.39)$$

$$a(\mathbf{u}_D, \mathbf{v}) - \alpha(P_D^{ex}, \nabla \mathbf{v}) = \hat{b}_D(\mathbf{v}) \quad (3.40)$$

where

$$\hat{q}_D(w) = \int_{\Gamma_{Neuman}} w q_D n \partial\Gamma + \int_{\Omega} w q_D \partial\Omega \quad (3.41)$$

$$\hat{b}_D(\mathbf{v}) = \int_{\Gamma_{Neuman}} (\sigma_{tD} \cdot \mathbf{n}) \cdot \mathbf{v} \partial\Gamma + \int_{\Omega} \mathbf{b}_D \cdot \mathbf{v} d\Omega \quad (3.42)$$

The statement of variational formulation for poroelasticity is described as find $\{\mathbf{u}_D(\mathbf{x}_D, t_D), P_D^{ex}(\mathbf{x}_D, t_D)\} \in V \times W$ such that:

$$\begin{aligned} \left(\alpha \frac{\partial(\nabla \cdot \mathbf{u}_D)}{\partial t_D}, w \right) + \left(Sr_D \frac{\partial(P_D^{ex})}{\partial t_D}, w \right) + b(P_D^{ex}, w) &= \hat{q}_D(w) \quad \forall w \in W \\ a(\mathbf{u}_D, \mathbf{v}) - \alpha(P_D^{ex}, \nabla \mathbf{v}) &= \hat{b}_D(\mathbf{v}) \quad \forall \mathbf{v} \in V \end{aligned} \quad (3.43)$$

with the initial conditions

$$\begin{aligned} P_D^{ex} &= P_{0D}^{ex} \quad \text{on } \Omega \text{ at } t_D = 0 \\ \mathbf{u} &= \mathbf{u}_{0D} \quad \text{on } \Omega \text{ at } t_D = 0 \end{aligned} \quad (3.44)$$

and boundary conditions included in equations 3.41 and 3.42 for Neumann

$$\begin{aligned} q_{D \text{ normal}} &= \bar{\mathbf{q}}_D \cdot \mathbf{n} \quad \text{on } \Gamma_{Neuman} \\ \sigma_{D \text{ normal}} &= \sigma_{tD} \cdot \mathbf{n} \quad \text{on } \Gamma_{Neuman} \end{aligned} \quad (3.45)$$

for Dirichlet

$$\begin{aligned} P_o &= P_{inlet} / outlet \quad \text{on } \Gamma_{Dirichlet} \\ \mathbf{u} &= \mathbf{u}_{constrains} \quad \text{on } \Gamma_{Dirichlet} \end{aligned} \quad (3.46)$$

3.4 Spatial discretization

Based on the statement of variational formulation given in 3.43 the semi-discrete continuous Galerkin finite element approximation for poroelasticity is given as follow:

Find $\{\mathbf{u}_{hD}(\mathbf{x}_D, t_D), P_{hD}^{ex}(\mathbf{x}_D, t_D)\} \in V_h^{r^1} \times W_h^{r^2}$ such that:

$$\left(\alpha \frac{\partial(\nabla \cdot \mathbf{u}_D)}{\partial t_D}, w_h \right) + \left(Sr_D \frac{\partial(P_D^{ex})}{\partial t_D}, w_h \right) + b(P_D^{ex}, w_h) \quad (3.47)$$

where

$$\hat{q}_D(w_h) = \int_{\Gamma_{Neuman}} w_h q_{Dn} \partial\Gamma + \int_{\Omega} w_h q_D \partial\Omega \quad (3.48)$$

$$\hat{b}_D(\mathbf{v}_h) = \int_{\Gamma_{Neuman}} (\sigma_{tD} \cdot \mathbf{n}) \cdot \mathbf{v}_h \partial\Gamma + \int_{\Omega} \mathbf{b}_D \cdot \mathbf{v}_h d\Omega \quad (3.49)$$

with the initial conditions

$$\begin{aligned} P_D^{ex} &= P_{0D}^{ex} \quad \text{on } \Omega \text{ at } t_D = 0 \\ \mathbf{u} &= \mathbf{u}_{0D} \quad \text{on } \Omega \text{ at } t_D = 0 \end{aligned} \quad (3.50)$$

and boundary conditions included in 3.48 and 3.49 for Neumann

$$\begin{aligned} q_{D \text{ normal}} &= \bar{\mathbf{q}}_D \cdot \mathbf{n} \quad \text{on } \Gamma_{Neuman} \\ \sigma_{D \text{ normal}} &= \sigma_{tD} \cdot \mathbf{n} \quad \text{on } \Gamma_{Neuman} \end{aligned} \quad (3.51)$$

for Dirichlet

$$\begin{aligned} P_o &= P_{inlet / outlet} \quad \text{on } \Gamma_{Dirichlet} \\ \mathbf{u} &= \mathbf{u}_{constrains} \quad \text{on } \Gamma_{Dirichlet} \end{aligned} \quad (3.52)$$

for application of finite element method, it is necessary to introduce shape functions for primary variables $\mathbf{u}_{hD}(\mathbf{x}_D, t_D)$, and $\mathbf{P}_{hD}^{ex}(\mathbf{x}_D, t_D)$ interpolated by unknown node values $\bar{\mathbf{u}} = \{u_1, u_2, u_3\}$ and \bar{p} as follows:

base function for displacements

$$\mathbf{u}_{hD}(\mathbf{x}_D, t_D) = \sum_{i=1}^{nodes} u_{1i} \Psi_i^u \mathbf{e}_1 + \sum_{i=1}^{nodes} u_{2i} \Psi_i^u \mathbf{e}_2 + \sum_{i=1}^{nodes} u_{3i} \Psi_i^u \mathbf{e}_3 \quad (3.53)$$

base function for excess pore pressure

$$P_{hD}^{ex}(\mathbf{x}_D, t_D) = \sum_{i=1}^{nodes} \bar{p}_i \Psi_i^P \quad (3.54)$$

and the test functions

$$\mathbf{v}_h(\mathbf{x}, t) = \sum_{i=1}^{nodes} v_{1j} \Psi_i^v \mathbf{e}_1 + \sum_{i=1}^{nodes} v_{2j} \Psi_i^v \mathbf{e}_2 + \sum_{i=1}^{nodes} v_{3j} \Psi_i^v \mathbf{e}_3 \quad (3.55)$$

$$w_h(\mathbf{x}, t) = \sum_{i=1}^{nodes} w_j \Psi_i^w \quad (3.56)$$

where the node values of equations 3.55 and 3.56 *i.e.* v_1, v_2, v_3 and w are arbitrary. The use of continuous Galerkin method is given from continuous piecewise polynomial finite element base and test functions such that belong to the same approximation space H^1 . For simplicity we can set

$$\begin{aligned} v_{1l} &= 1 \quad \text{and} \quad v_{1j} = 0 \quad \text{for } j \neq l \\ v_{2l} &= 1 \quad \text{and} \quad v_{2j} = 0 \quad \text{for } j \neq l \\ v_{3l} &= 1 \quad \text{and} \quad v_{3j} = 0 \quad \text{for } j \neq l \\ w_l &= 1 \quad \text{and} \quad w_j = 0 \quad \text{for } j \neq l \end{aligned} \quad (3.57)$$

inserting this expressions (3.53), (3.54), (3.55) and (3.56) into (3.47), it yields:

$$\begin{aligned}
& - \int_{\Omega} (\lambda_D (\nabla \cdot \mathbf{u}_{hD}) + 2\mu_D \epsilon(\mathbf{u}_{hD})) \cdot \epsilon(\mathbf{v}_h) \, d\Omega + \int_{\Omega} (\alpha P_{hD}^{ex} I \cdot \nabla \mathbf{v}_h) \, d\Omega \\
& + \int_{\Gamma_{Neuman}} (\sigma_{tD} \cdot \mathbf{n}) \cdot \mathbf{v}_h \, \partial\Gamma + \int_{\Omega} \mathbf{b}_D \cdot \mathbf{v}_h \, d\Omega = 0 \quad (3.58)
\end{aligned}$$

$$\begin{aligned}
& \int_{\Omega} \left(\frac{\partial (\alpha \nabla \cdot \mathbf{u}_{hD})}{\partial t} \right) w_h \, \partial\Omega + \int_{\Omega} \left(\frac{\partial (S_{rD} P_{hD}^{ex})}{\partial t} \right) w_h \, \partial\Omega + \int_{\Omega} (\nabla (P_{hD}^{ex})) \cdot \nabla w_h \\
& + \int_{\Gamma_{Neuman}} w_h q_{D \, normal} \, \partial\Gamma + \int_{\Omega} w_h q_D \, \partial\Omega = 0 \quad (3.59)
\end{aligned}$$

Integral terms can be written in form of matrices operations as:

Linear strain operator

$$K_{elasticity} \, \bar{\mathbf{u}} = \int_{\Omega} (\lambda_D (\nabla \cdot \mathbf{u}_{hD}) + 2\mu_D \epsilon(\mathbf{u}_{hD})) \cdot \epsilon(\mathbf{v}_h) \, d\Omega \quad (3.60)$$

Coupling matrix

$$Q_c \, \bar{\mathbf{p}} = \int_{\Omega} (\alpha P_{hD}^{ex} I \cdot \nabla \mathbf{v}_h) \, d\Omega \quad (3.61)$$

Force right hand term

$$F^u = \int_{\Gamma_{Neuman}} (\sigma_{tD} \cdot \mathbf{n}) \cdot \mathbf{v}_h \, \partial\Gamma + \int_{\Omega} \mathbf{b}_D \cdot \mathbf{v}_h \, d\Omega \quad (3.62)$$

For diffusion problem

$$Q_c^T \frac{d\bar{\mathbf{u}}}{dt_D} = \int_{\Omega} \left(\frac{\partial (\alpha \nabla \cdot \mathbf{u}_{hD})}{\partial t_D} \right) w_h \, \partial\Omega \quad (3.63)$$

Compressibility matrix

$$S \frac{d\bar{\mathbf{p}}}{dt_D} = \int_{\Omega} \left(\frac{\partial (S_{rD} P_{hD}^{ex})}{\partial t_D} \right) w_h \, \partial\Omega \quad (3.64)$$

Permeability matrix

$$H \, \bar{\mathbf{p}} = \int_{\Omega} (\nabla (P_{hD}^{ex})) \cdot \nabla w_h \quad (3.65)$$

Mass right hand term

$$F^p = \int_{\Gamma_{Neuman}} w_h q_{D \, normal} \, \partial\Gamma + \int_{\Omega} w_h q_D \, \partial\Omega \quad (3.66)$$

obtaining the follow semi-discrete continuous galerkin system

$$\begin{bmatrix} K_{elasticity} & -Q_c \\ Q_c^T & S + H \end{bmatrix} \begin{bmatrix} \bar{\mathbf{u}} \\ \bar{\mathbf{p}} \end{bmatrix} = \begin{bmatrix} F^u \\ F^p \end{bmatrix} \quad (3.67)$$

3.5 Time discretization

Since the discretization in space has been carried out, the system 3.67 represent a set of ordinary differential equations in time. For convenience the equations are written in the following form:

$$\begin{bmatrix} K_{elasticity} & -Q_c \\ 0 & H \end{bmatrix} \begin{bmatrix} \bar{\mathbf{u}} \\ \bar{\mathbf{p}} \end{bmatrix} + \begin{bmatrix} 0 & 0 \\ Q_c^T & S \end{bmatrix} \frac{d}{dt_D} \begin{bmatrix} \bar{\mathbf{u}} \\ \bar{\mathbf{p}} \end{bmatrix} = \begin{bmatrix} F^u \\ F^p \end{bmatrix} \quad (3.68)$$

Finite differences in time are used for the solution of the initial value problem. Consider the follow equation:

$$H \frac{d\mathbf{x}}{dt} + C\mathbf{x} = F \quad (3.69)$$

The discretization in time is carried out by the generalized trapezoidal method (Wynne, 2000). This is an implicit method, and for the approximation of

$$\begin{aligned} \left(\frac{d\mathbf{x}}{dt} \right)_{n+\xi} &= \frac{(\mathbf{x}_{n+1} - \mathbf{x}_n)}{\Delta t_D} \\ \mathbf{x}_{n+\xi} &= (1 - \xi) \mathbf{x}_n + \xi \mathbf{x}_{n+1} \end{aligned} \quad (3.70)$$

where Δt_D is the time step length, \mathbf{x}_n and \mathbf{x}_{n+1} , are the state vectors at times t_{Dn} and t_{Dn+1} , and ξ is a parameter which has limits $0 \leq \xi \leq 1$. The value of ξ may be obtained from the numerical properties of the scheme in Table 3.1.

Application of this procedure to equation 3.68 and multiplying by -1 the set of the equations corresponding to diffusive problem, the symmetry is restored

$$\begin{aligned} & \begin{bmatrix} K_{elasticity} & -Q_c \\ -Q_c^T & -S - \xi \Delta t_D H \end{bmatrix}_{n+\xi} \begin{bmatrix} \bar{\mathbf{u}} \\ \bar{\mathbf{p}} \end{bmatrix}_{n+1} \\ & + \begin{bmatrix} 0 & 0 \\ Q_c^T & S - (1 - \xi) \Delta t_D H \end{bmatrix}_{n+\xi} \begin{bmatrix} \bar{\mathbf{u}} \\ \bar{\mathbf{p}} \end{bmatrix}_n = \begin{bmatrix} F^u \\ \Delta t_D F^p \end{bmatrix}_{n+\xi} \end{aligned} \quad (3.71)$$

In Wynne (2000) is proved that $\xi \geq \frac{1}{2}$ is corresponding to unconditionally stable methods in time.

The first matrix on (3.71) represents the stiffness and the second one represents the mass contribution to poroelastic problem. If the initial condition of poroelasticity corresponds

Table 3.1: Time schemes summarized in terms of different ξ values. Source: Wynne (2000).

ξ value		Time Scheme
$\xi =$	0	Euler forward finite difference method
$\xi =$	1	Backward finite difference method
$\xi =$	0.5	Crank-Nicolson finite difference method
$\xi =$	0.6667	Zienkiewicz Galerkin method
$\xi =$	$1 + \left(\frac{1}{\Delta t_D} - \frac{1}{\ln(1+\Delta t_D)} \right)$	Sanhu logarithmic method
$\xi =$	$1 + \left(\frac{t_k}{t_{k+1}-t_k} - \frac{1}{\ln\left(1+\frac{t_{k+1}-t_k}{t_k}\right)} \right)$	Hwang logarithmic method

to undrained conditions, the initial solution corresponds to solving the elastic problem, and the pressure field is dependent on the volumetric deformation of the solid matrix. Thus the initial system leads to

$$\begin{bmatrix} K_{elasticity} & -Q_c \\ Q_c^T & S + \xi \Delta t_D H \end{bmatrix} \begin{bmatrix} \bar{\mathbf{u}} \\ \bar{\mathbf{p}} \end{bmatrix} = \begin{bmatrix} F^u \\ \Delta t_D F^p \end{bmatrix}_{n+\xi} \quad (3.72)$$

But if incompressible constituents are present and diffusion terms do not exist, the compressibility matrix and permeability matrix lead to zero diagonal terms in 3.72, consequently, the matrices to be solved are identical to incompressible elasticity. In such cases, there are limitations for the approximating functions and the Babuska-Brezzi convergence condition must be satisfied to avoid non-physical oscillations.

The perturbation problem presented in Figure 1.1 is solved by the system (3.71), where it is important to point out that stiffness and mass global matrices (3.73) are calculated once time as well as the solution of the global system. Thus, the iterative process is reduced to update the global load vector (3.74) as the product between the solution vector at time n and the global mass matrix, plus the constant load vector representing the mass flux and the body forces (right term in (3.74)), and finally by multiplying by the inverse of the stiffness matrix, the solution vector at time $n + \xi$ is obtained. This implies that the time step Δt_D is held constant for the entire calculation.

$$\begin{aligned} \text{Stiffness} & \quad \begin{bmatrix} K_{elasticity} & -Q_c \\ -Q_c^T & -S - \xi \Delta t_D H \end{bmatrix}_{n+\xi} \\ \text{Mass Matrix} & \quad \begin{bmatrix} 0 & 0 \\ Q_c^T & S - (1 - \xi) \Delta t_D H \end{bmatrix}_{n+\xi} \end{aligned} \quad (3.73)$$

$$Load\ Vector_{n+\xi} = - \begin{bmatrix} 0 & 0 \\ Q_c^T & S - (1 - \xi) \Delta t_D H \end{bmatrix}_{n+\xi} \begin{bmatrix} \bar{\mathbf{u}} \\ \bar{\mathbf{p}} \end{bmatrix}_n + \begin{bmatrix} F^u \\ \Delta t_D F^p \end{bmatrix}_{n+\xi} \quad (3.74)$$

3.6 Summary

The derivation of the weak formulation and its respective continuous Galerkin (CG) form of poroelastic monophasic flow is presented in terms of bilinear forms, thus the corresponding solution of these equations were described in terms of displacement and excess pore pressure as state variables of the problem. The discrete form of the equations represents a set of ordinary differential equations in time. Finite differences were used to approximate the temporal variable in an implicit matrix and fully coupled formulation with different time schemes.

4. Implementation and validation

4.1 Implementation

The finite element method was selected to implement the formulation represented by the matrix systems 3.73 and 3.74. One of its capabilities is modeling complex geometries and using different polynomial orders to approximate the state variables. However, the use of this technique represents relative complex challenges from the computational point of view. This complexity is related to integral calculations, boundary conditions, the need to use different polynomial orders and different elements types in the same computational mesh. It is possible to overcome these computational complexities by using object oriented programming. In object oriented programming, data processing is given by the interaction of objects that can compute and interchange data to solve one specific problem.

In an object oriented environment, classes represent entities describing data and set of actions for designing applications and computer programs. When one set of data is determined, the actions to be executed over this set are determined only under the class rules. The use of classes is reflected through objects generated from them; thus one object can be viewed as an independent machine with a distinct role or responsibility. When one object is generated its actions (or methods) on data are closely associated with it. Thus instead of programming one set of routines to solve a problem, it is possible to generate objects that interact between them to solve the same problem.

The cornerstone of object oriented programming is the reuse of classes already developed and tested in different problems. This favors the quick development of new functionalities of an existing system to solve another type of problem, since the programmer is focused on implementing the needed code without thinking about all the possible modifications. It decreases the possibilities of errors that can alter the normal functionality of the system. In object oriented environments to solve partial differential equations with finite elements; matrices, vectors, solvers, nodes, geometric and computational elements are treated as objects that interact under several rules. This implementation, *LPA*, was developed using the NeoPZ environment Devloo (2009) and new classes were implemented to solve the formulation in question.

NeoPZ description

NeoPZ environment is an object oriented C++ library for the development of finite element programs (Devloo, 2009), maintained by the LabMeC staff at Unicamp and accessible from Google Code. The main characteristic of the NeoPZ environment is the strong separation between geometry modelling, definition of the interpolation space and definition of the variational statement used to approximate the physical problem. This approach offers user a generic environment where the re-usability of implemented finite element algorithms is maximized, for instance:

- One dimensional geometric element which uses a mapping in cylindrical coordinates is implemented . Using this, rings or helicoidal springs can be approximated without error in the geometrical map.
- Hierarchical shape functions have been defined for the computational elements. Consequently, all finite element approximations using NeoPZ can make use of high order interpolation functions, independently of the underlying variational statement.
- H-adaptivity has been implemented, both at the level of the geometric and computational grid. At the computational grid level, compatibility constraints are computed between elements which have common sides at a different level. As a result, all finite element models implemented in PZ can use adaptive grids.
- Any new model, represented by some partial differential equation can be introduced by adding a class derived from the TPZMaterial class. After the variational statement has been implemented, it can be approximated by C0 finite elements of any interpolation order, using adapted grids if desired.

LPA description

Linear poroelastic analysis LPA is composed of several C++ classes already implemented in NeoPZ (TPZGeomesh, TPZCompMesh, TPZMultiphysicsElement). In addition, the class TPZPoroElastic2d was developed to compute the poroelastic contribution based on the weak statement previously presented as well as others for geometry processing and analytical functions (TPZReadGIDGrid). The LPA is based on three principal classes TPZGeomesh, TPZCompMesh and TPZPoroElastic2d, which involve finite element computations. Operations like generation of geometries, matrix and solution calculations are considered out of these classes, since they are not an essential part of finite elements procedures.

The main program can be described by several steps as follows:

- Generate the geometry that represents the description of nodes, elements and materials identifiers.
- Using the geometric information two computational meshes are created one for elasticity, another for the diffusion problem.
- Based on these meshes, the Poroelastic mesh (overlapping of diffusive and elastic domains is generated (see Figure 4.2), by using the class *TPZPoroElastic2d*.
- Compute the contribution for each computational element and assemble the global stiffness and load vector
- Do time calculations and print the required data at each time.

TPZGeomesh

The class *TPZGeomesh* implements a geometric mesh for the NeoPZ environment. It provides services for description of geometric elements: one, two and three-dimensional elements can be used. Several classes derived from *TPZGeomesh* are used to store the necessary data in the geometric information such as nodes, elements, material identifiers as well as node coordinates, elements sides and jacobian calculations for isoparametric elements. All this information is needed to compute global stiffness and load vector arrays.

TPZCompMesh

The class *TPZPoroElastic2d* defines the interpolation space and the integration over each element. It has the information required to compute the stiffness and load vector arrays for each boundary and domain elements. The computational mesh is like a repository of computational elements, nodes and material objects that define the way the calculations are done. In this work the class *TPZPoroElastic2d* controls how to compute the contribution over each computational element. *TPZCompMesh* also contains the current solution of the mesh and an element wise solution vector.

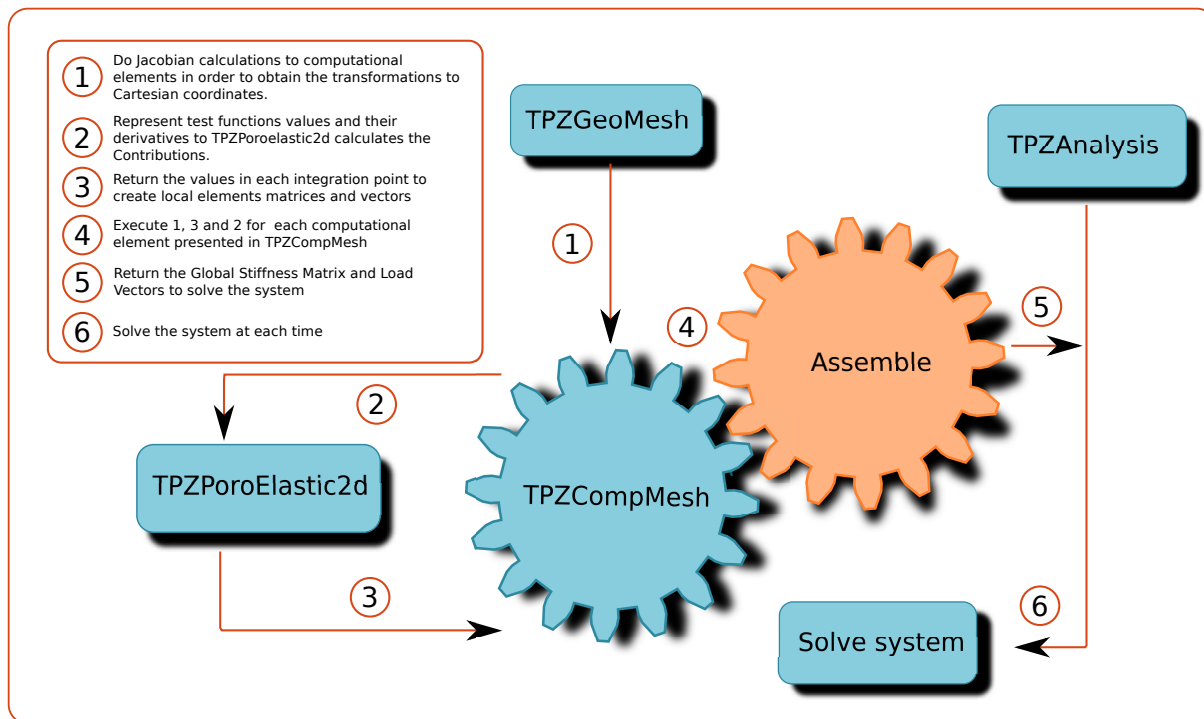
TPZPoroElastic2d

The class *TPZPoroElastic2d* is the most important in LPA computations because it represents the mathematical description of the poroelastic problem defined previously, and in particular it contains one method called *contribute* that represents the weak statement and how the poroelastic contributions of each elements are done. Detailed description of this method is given in the appendix B.1. Algorithms 1, 2, 3 and 4 explain the code lines

of contribute method and their relationships with the mathematical expressions developed in chapter 3.

In *TPZPoroElastic2d* the element contributions are computed using basis and weight functions and their corresponding derivatives according to the bilinear forms given in chapter 3. This basis and weight functions values are provided for the computational mesh into *TPZCompMesh* class. Figure 4.1 represents how the element information is processed between the objects generated by each class.

Figure 4.1: Schematic flow of data computations and class interactions.

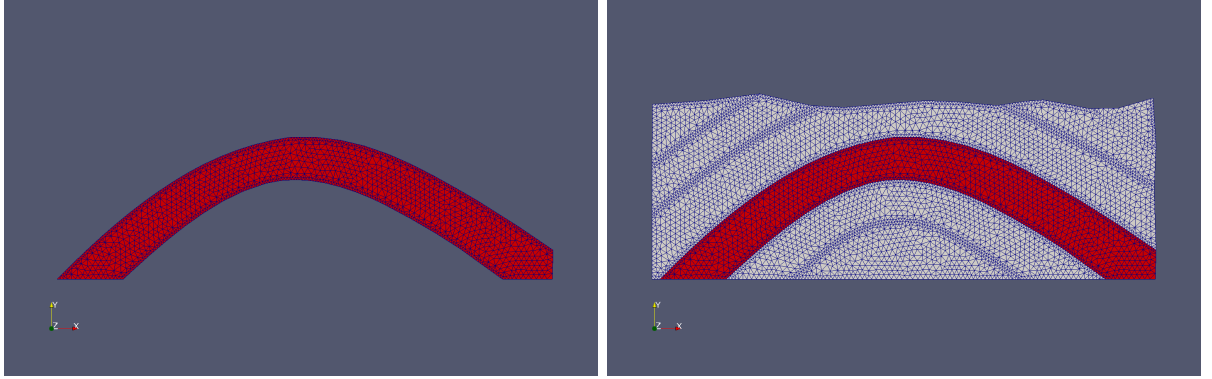


Multiphysics point of view

The concept of multi-physics simulations into NeoPZ is very different from other known finite element implementations. Multiphysics meshes and classes have been validated on approximations using HDiv flux-pressure interaction. In this work, coupled flow through porous media modeled by linear poroelasticity is validated, contributing to NeoPZ's multiphysics branch. In a general form a multiphysic mesh is composed of the information given in each material domain that represents one specific state variable. Thus it is necessary to define different domains with geometric information to calculate the respective basis and weight functions presented in the finite element formulations. Figure 4.2 shows

how it is possible to define different domains and to compose the poroelastic domain (red domain) embedded in an elastic matrix with conforming meshes.

Figure 4.2: Embedded domain by overlapping areas. Left) Diffusion domain that contains all geometric information and computational information for flow calculations, Right) Elastic domain that contains all geometric information and computational information for elasticity.

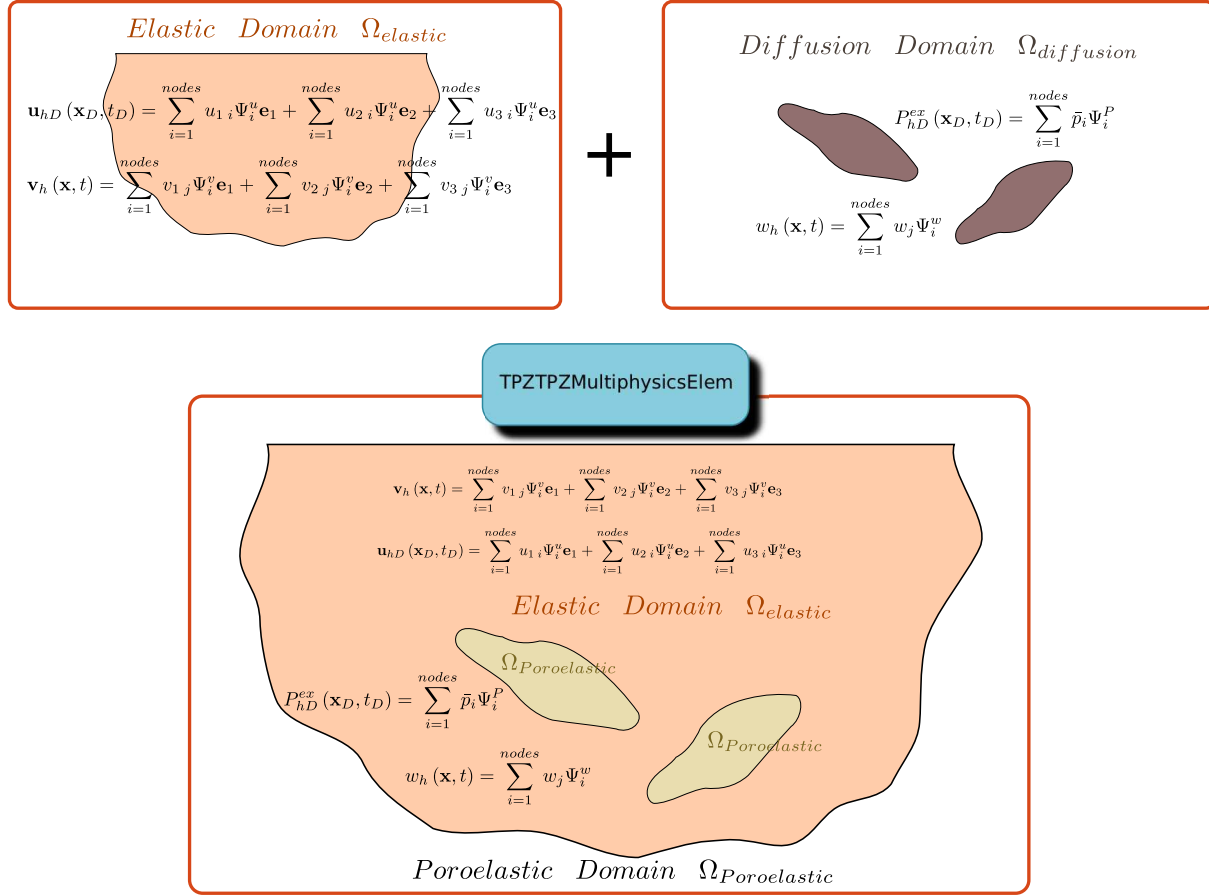


In finite element approximations of systems of partial differential equations, it is customary to associate the same weight function to each state variable. For instance, in two-dimensional elasticity the same weight function is associated with the horizontal and vertical displacements. In most of finite element approximations, the number of state variables associated with each shape function is constant. In these cases, the number of state variables can be a value associated with geometric meshes. In multiphysics problems, the number of state variables can vary according to the physical quantity being represented. For instance, in numerical approximations of flow through porous media, two (or three) state variables are associated with the shape functions which approximate the displacements of the porous matrix and a single shape function is associated with the pressure variable. In NeoPZ there exists one entity that contains the information about the shape functions called *connect*. Each *connect* keeps track of the number of state variables associated with its weight function and consequently it is used to model poroelastic inclusions, by combining the geometric information for each weight function in each domain intersection, *i.e.* one computational mesh can be viewed as an independent 2D plane of information that combine the multiphysics classes (see Figure 4.3) with other computational domains, as *TPZPoroElastic2d* that merges the intersecting meshes information, following mathematical statements of linear poroelasticity.

Also it is very important to point out that once the variational statement of a multiphysics problem, for example thermo-poroelasticity, is defined, it can be implemented via the procedure explained in appendix B. Figure 4.3 represents the associated basis and weight

functions with each computational mesh, thus the *TPZCompMesh* and *TPZPoroElastic2d* classes have the required data to calculate the contribution of each element.

Figure 4.3: Multi-physics view of the poroelastic problem. All the information of each computational element that represent one physical problem is stored and processed by multiphysics elements as the poroelastic elements represented by *TPZPoroElastic2d*. Left) Computational Elasticity Mesh. Right) Computational Diffusion Mesh.



Geometry Generation using GID

In this section, the process to generate the geometry using GID is described. GID is a universal, adaptive and user-friendly pre and post-processor for numerical simulation in science and engineering. It has been designed to cover all the common needs in the numerical simulations field from pre to post-processing: geometrical modeling, effective definition of analysis data, meshing, data transfer to analysis software, as well as the visualization of numerical results. It was chosen for preprocessing the geometry, because

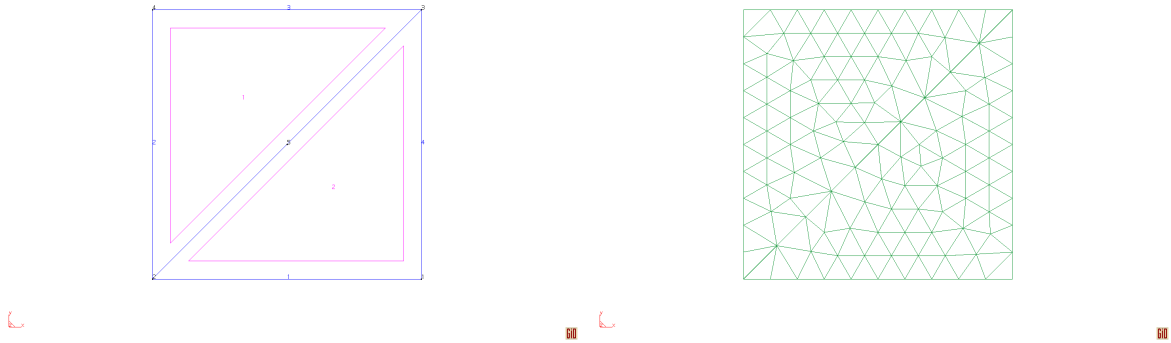
it can be easily adapted to the problem requirements. For LPA geometric input a customized material template was defined in order to associate the material identifiers with the geometric elements (Algorithm 5).

Geometry generation can be done by command line or graphical user interface (GUI). For the quick generation of meshes, the GUI method is preferred, but to generate a model for parametric analysis the command line is preferred. Basically, geometry generation is divided into four steps:

- Open a new project, then select a problem and type `ansys55plane`, by following Menu / Data / Problem Type / `ansys55` / `ansys55plane`.
- Save under any name and close the program.
- In the folder of the GID project, replace the content of the `*.mat` file by Algorithm 5.
- Open the project and generate your own geometry associating the materials identifiers.

Finally once the geometry is generated, it is exported to a `*.dump` file that contains all the information of the geometric mesh and the associated materials.

Figure 4.4: Geometry generated in GID and its corresponding geometric mesh.



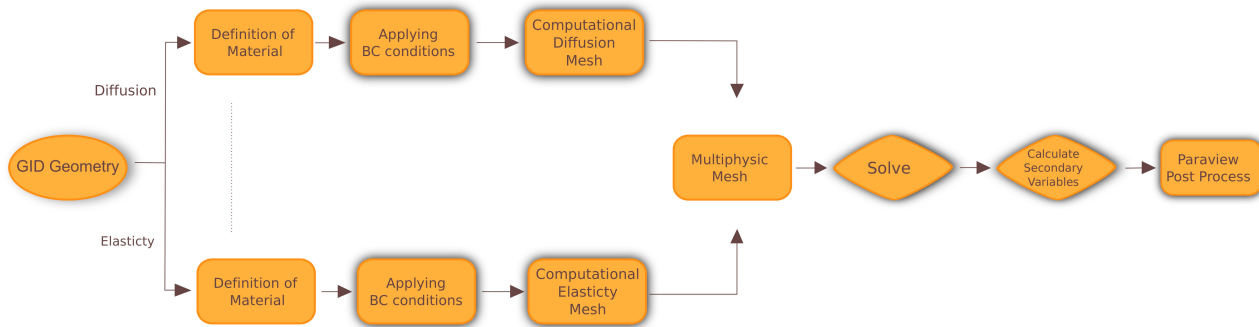
Xml control file

Extensible Language (XML) is a set of rules for encoding documents in machine readable form. XML is a popular format for sharing data on internet. Websites that frequently update their content, such as news sites or blogs, often provide an XML feed so that external programs can keep abreast of content changes. Uploading and parsing XML data is a common task for network-connected apps. TinyXML is a simple, small, C++

XML parser that can be easily integrated into other programs. In brief, TinyXML parses an XML document, and builds from that a Document Object Model (DOM) that can be read, modified, and saved. Xml files control LPA computations. All the cases and tests presented here have one GID **.dump* and **.xml* files that define the control of the simulation and the simulation times to print information.

In summary, to implement a strong formulation using NeoPZ environment, the attention is concentrated on coding the corresponding weak formulation in NeoPZ code lines. Weak forms of linear poroelasticity were translated to NeoPZ syntax as shown in Appendix B.1. Figure 4.5 shows a simple work flow to generate computational models with LPA; the information is processed from the geometry created in GID and exported to **.dump* files, then converted for LPA to geometric and computational meshes and the simulation behavior is defined by **.xml* files. The simulation results are post-processed using **.vtk* files in Paraview.

Figure 4.5: General work flow to solve poroelasticity equations.



4.2 Computational Tests

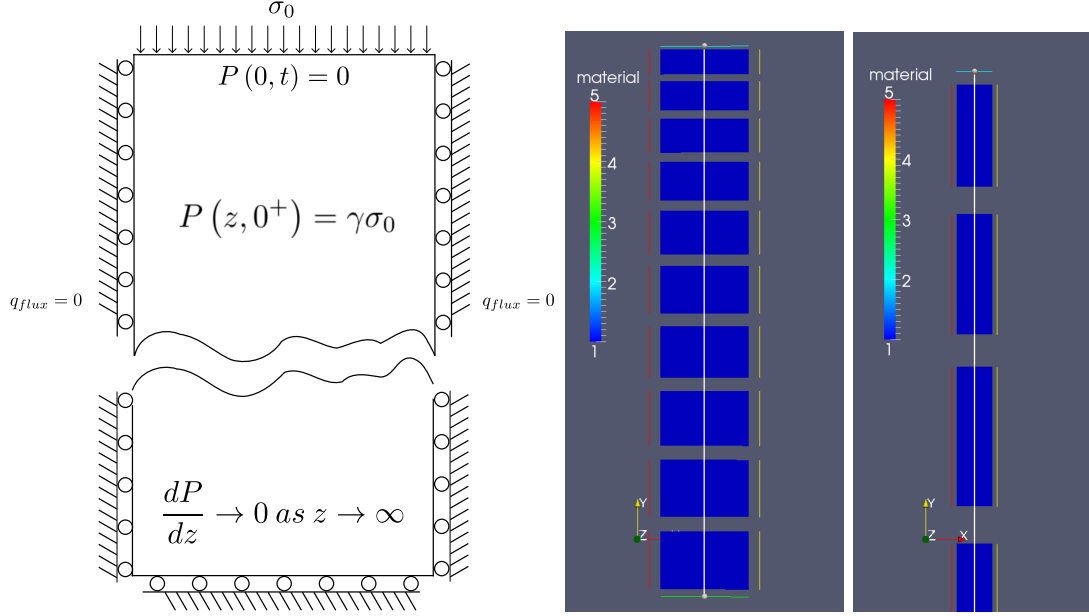
In order to demonstrate the code validity, two different problems with analytical solutions are presented:

1. Step load applied to infinite and finite columns.
2. Mass source injection into a bounded infinite poroelastic medium.

4.3 Step load applied to an elastic half space

The sudden application of a uniform surface load by permeable piston is the natural consolidation problem. When a burial history occurs in a very short time relative to fluid diffusion it can be modeled as a step change in vertical load as shown in Figure 4.6.

Figure 4.6: Step load applied to a poroelastic half space. Left) Boundary conditions for the poroelastic column. Geometric Mesh with associated materials identifiers (Colors), the blue one (number 1) represents the poroelastic column and the others, the boundary conditions. Center) Mesh for finite poroelastic column, Right) Mesh for Infinite poroelastic column. Source: redraw from Wang (2000).



Semi-Infinite poroelastic column

Initial and boundary conditions

The problem is to find the excess pore pressure $P^{ex}(y, t)$, and vertical displacement, $\mathbf{u}(y, t)$, after a uniform downward load $-\sigma_{t0}$ is suddenly applied at $t = 0$ on $y = 0$ of a vertical infinite column that is constrained laterally for two non flux boundaries. The vertical load is held constant with time, and the top surface is drained $P^{ex}(0, t) = 0$. Mechanical equilibrium requires that the suddenly applied surface load $-\sigma_{t0}$ be transmitted instantaneously throughout the column. This constant vertical stress at all depths induces an excess pore pressure $P^{ex} = \gamma\sigma_{t0}$ at all depths and at different times.

Dimensionless expressions

Using the same procedure for dimensionless forms of poroelastic problem and inserting the dimensionless groups of table 4.1 in the equations given in Wang (2000), the following analysis results are obtained:

Table 4.1: Group of dimensionless variables for step load in semi-infinite poroelastic solid.

Symbol	Definition
\mathbf{u}_D	$\frac{\mathbf{u}}{L P_0^{ex}} \frac{(\lambda_u - \lambda)}{\alpha^2} \frac{(\lambda + 2\mu)}{(\lambda_u + 2\mu)}$
c_{mD}	$cm P_0^{ex}$
P_D^{ex}	$\frac{P^{ex}}{P_0^{ex}}$
\mathbf{v}_D	$\mathbf{v} \frac{\eta}{\kappa} \frac{L}{P_0^{ex}}$
z_D	$\frac{z}{L}$
\mathbf{u}_{zD}	$\frac{\mathbf{u}_z}{L}$
t_D	$t \frac{L^2}{c}$

Excess pore pressure

The governing equation and initial and boundary conditions for excess pore pressure are mathematically identical to the heat diffusion problem (Figure 4.6). In one specific conditions of one-dimensional problem, uniaxial strain with constant vertical stresses, the uncoupled homogeneous pore pressure diffusion equation is obtained as:

$$P_D^{ex}(y_D, t_D) = \text{erfc}\left(\frac{y_D}{2\sqrt{t_D}}\right) \quad (4.1)$$

at dimensionless argument $\frac{y_D}{2\sqrt{t_D}} = 1.0$ the excess pore pressure has declined about 15 percent from initial state. Based on this criterion, an estimate of the time it takes for the surface pressure to propagate diffusively to depth y_D is given by $t_D = \frac{y_D^2}{4}$.

Displacement

An infinite column length means that the initial vertical displacement at the surface is infinite in response to sudden application of the load. However the time-dependent displacements of the surface y_D of the infinite column is finite and is given as.

$$\mathbf{u}_{yD}(y_D, t_D) = \left(\frac{2\sqrt{t_D} e^{-\frac{y_D^2}{4t_D}}}{\sqrt{\pi}} - y_D \text{erfc}\left(\frac{y_D}{2\sqrt{t_D}}\right) \right) \mathbf{1}_y \quad (4.2)$$

Darcy velocity

$$\mathbf{v}_{yD}(y_D, t_D) = -\frac{e^{-\frac{y_D^2}{4t_D}}}{\sqrt{\pi}\sqrt{t_D}} \mathbf{1}_y \quad (4.3)$$

Numerical results

The geometric mesh is composed of 10 quadrilateral elements with cubic-quadratic orders (displacements $r^1 = 3$ and excess pore pressure $r^2 = 2$) representing a column with finite length of $L = 10.0$ (see Figure 4.6 right side). Assuming incompressible rock and fluid constituents, simulation time of 1 and time step $\Delta t_D = 0.001$, figures 4.7 and 4.8 show the evolution of excess pore pressure and displacement at different dimensionless times. A good approximation is obtained using cubic-quadratic elements.

Figure 4.7: Dimensionless displacement y direction for semi-infinite column at different dimensionless times. Plot line $((0, 0), (0, -10.0))$. Points represent the numerical solution.

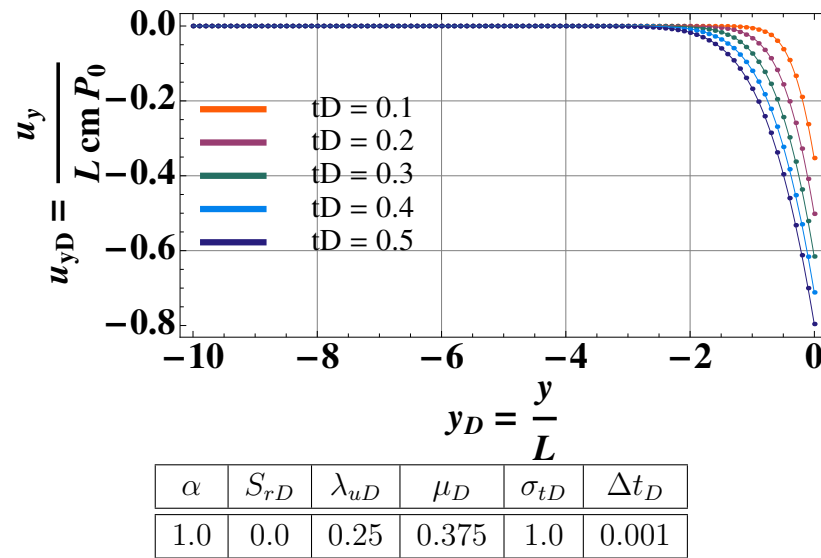
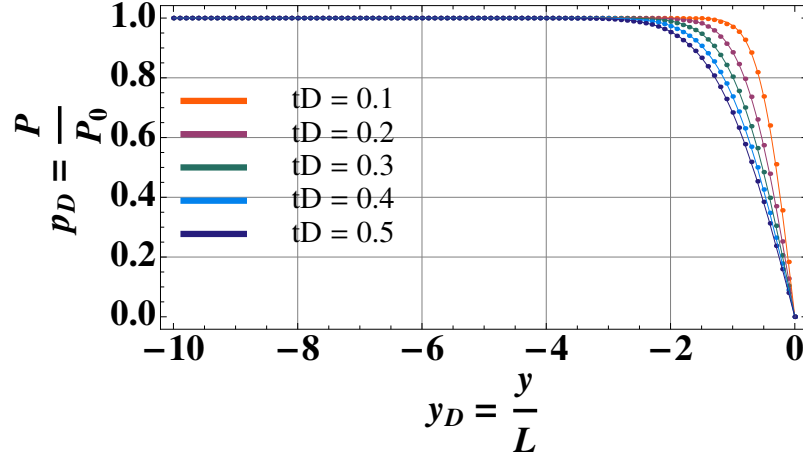


Figure 4.8: Dimensionless excess pore pressure for semi-infinite column at different dimensionless times. Plot line $((0, 0), (0, -10.0))$. Points represent the numerical solution.



Finite poroelastic column

In Terzaghi's classical consolidation test the poroelastic column is finite *i.e.* $L = 1.0$. A constant stress $-\sigma_t$ is applied suddenly on the surface $z = 0$ of a fluid saturated sample of length L . This problem is analogue to a semi-infinite column with the same boundary condition and step load. Dimensionless forms of these equations are given by Korsawe and Starke (2006) as:

Pore Pressure Excess

$$P_D^{ex}(y_D, t_D) = \sum_{n=0}^{\infty} \left(\frac{2}{M} \sin(M \cdot x_D) \exp^{-M^2 t_D} \right) \quad (4.4)$$

Displacement

$$u_{yD}(y_D, t_D) = 1 - x_D - \sum_{n=0}^{\infty} \left(\frac{2}{M} \cos(M \cdot x_D) \exp^{-M^2 t_D} \right) \quad (4.5)$$

Darcy velocity

$$v_D(y_D, t_D) = - \sum_{n=0}^{\infty} \left(2 \cos(M \cdot x_D) \exp^{-M^2 t_D} \right) \quad (4.6)$$

where $M = \frac{1}{2}\pi(2n+1)$. These expressions are compatible with the variables defined in Table 2.1.

Numerical results

An excellent fit is obtained for the state variables shown in figures 4.9 and 4.10.

Figure 4.9: Dimensionless displacement y direction for finite column at different dimensionless times along the plot line $((0, 0), (0, -1.0))$. Points represent the numerical solution.

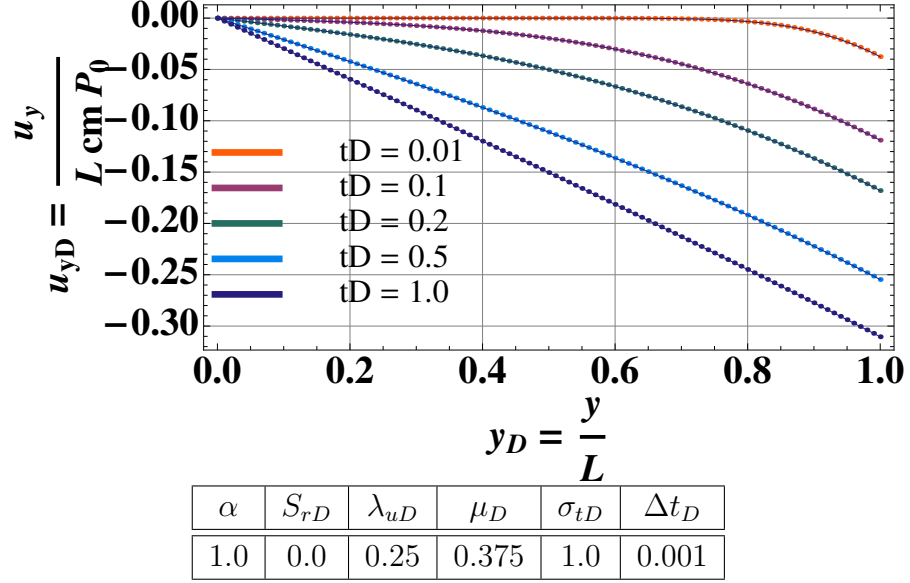
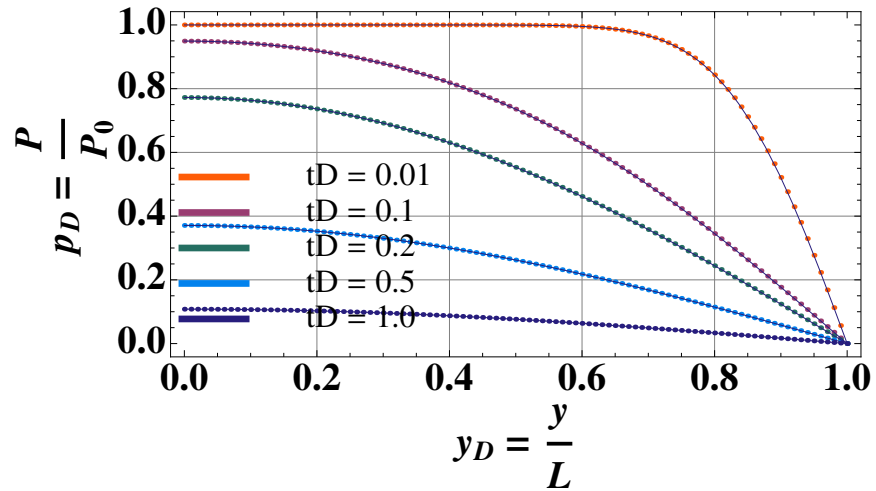


Figure 4.10: Dimensionless excess pore pressure for finite column at different dimensionless times along the plot line $((0, 0), (0, -1.0))$. Points represent the numerical solution.



The solution of Korsawe and Starke (2006) is described by equation 4.1 for $t_D < 0.04$. For t_D greater than this limit the effect of the impermeable boundary is observed in figure 4.11, because limited mass in the finite column doesn't support pressure for long times. Consequently a fast draw down is observed in relation to infinite behavior.

Figure 4.11: Dimensionless excess pore pressure for finite and semi-infinite columns at $t_D = 0.2$. Plot line $((0, 0), (0, -1.0))$.

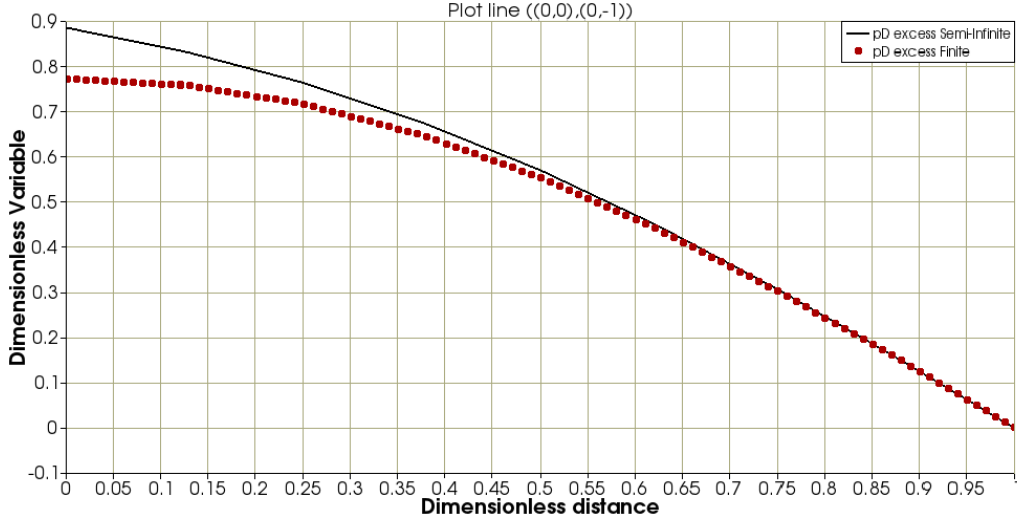
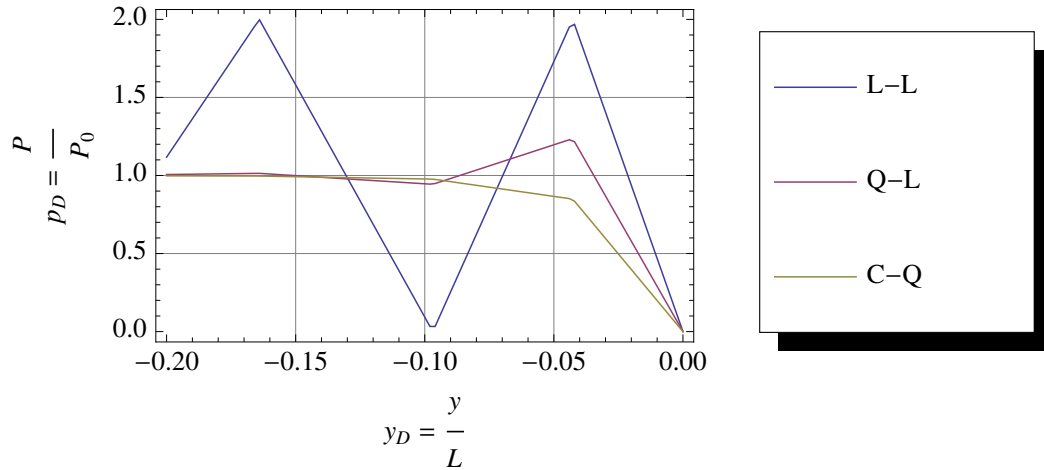


Figure 4.12: Poroelastic response of finite column along $0 < y_D < 0.2$ case with incompressible constituents at 10 time steps.



α	S_{rD}	λ_{uD}	μ_D	σ_{tD}	Δt_D
1.0	0.0	0.25	0.375	1.0	1.10^{-10}

The figure 4.12 shows pressure oscillations generated by using linear-linear (L-L or ($r^1 = 1$, $r^2 = 1$)) and quadratic-linear (Q-L) elements when undrained initial response with incompressible constituents is approximated. Please note that for cubic-quadratic (C-Q) elements no oscillation was observed. C-Q or higher order elements are used over the calculations in chapter 5.

Convergence rate in time approximation

The Crank-Nicolson ($\xi = 0.5$) finite difference scheme has second-order approximation. Consequently $\xi = 0.5$ has the best answer in terms of error norm $\|error\| = \|U_n - U_{an}\|$ for each state variable with time step decrease as shown in Figures 4.13 and 4.14. In general $\xi = 0.5$ will be used to calculate poroelastic responses in chapter 5.

$$\|error\| = \left(\int_{\Omega} error^2 d\Omega \right)^{\frac{1}{2}} \quad (4.7)$$

Another consideration is the Courant–Friedrichs–Lewy condition (CFL condition) that relates the time step size with the size of the discrete parts (elements). Normally, if an explicit numeric scheme is used, the CFL must be equal to 1 to obtain convergence. The implicit scheme used here is less sensitive to numerical instability and so larger values of CFL may be tolerated.

Figure 4.13: Error norm for excess pore pressure vs different time steps with different time schemes $\xi = \{0.5, 0.6667, 1.0\}$.

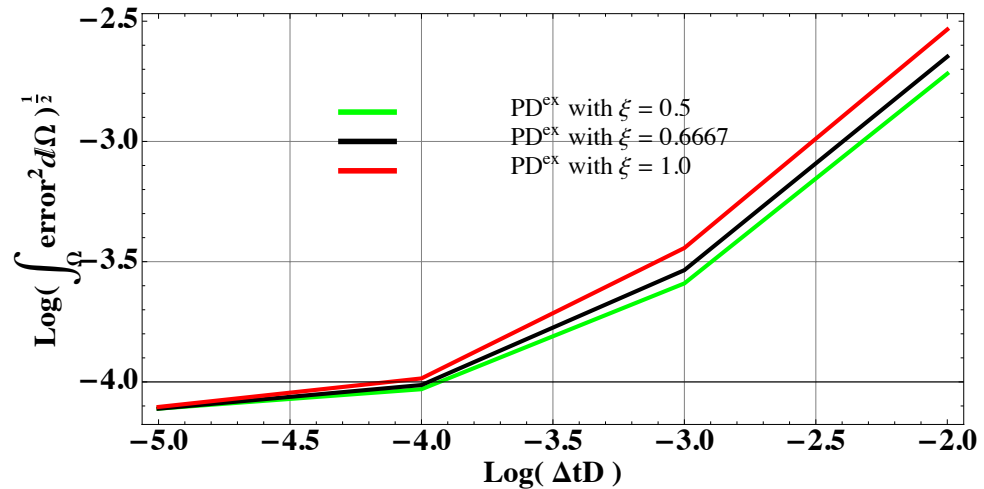
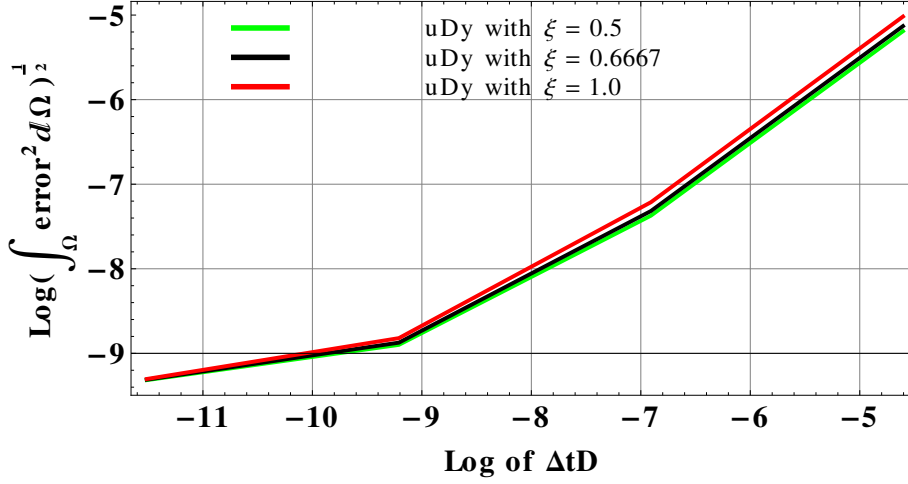


Figure 4.14: Error norm for displacement in y direction vs different time steps with different time schemes $\xi = \{0.5, 0.6667, 1.0\}$.



Convergence rate with different DOF

The error norm is computed for spatial discretization refinement and polynomial order increase, and both cases reflect an increase in the numbers of degrees of freedom. Starting from a base mesh, spatial refinement or level of refinement are built by dividing each element into four elements. Figures 4.15 and 4.16 show how the error norm decreases with progressive refinement.

Figure 4.15: Error norm for excess pore pressure vs number of DOF with different refinement levels 0, 1, 2, 3.

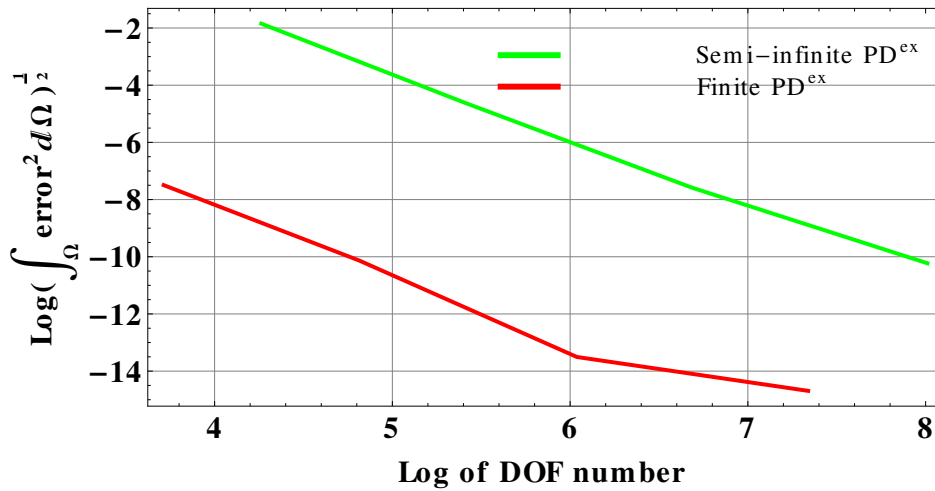
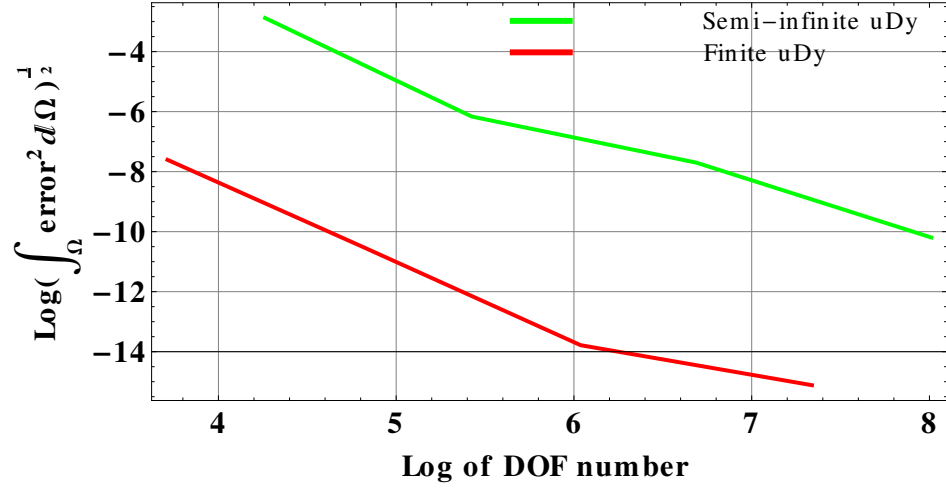


Figure 4.16: Error norm for displacement in y direction vs number of DOF with different refinement levels 0, 1, 2, 3.



Figures 4.17 and 4.18 show fast convergence with increment in polynomial order in comparison with spatial refinement. Using $(r^1 = 4, r^2 = 3)$ or $(r^1 = 5, r^2 = 4)$ with coarse meshes, it is possible to obtain reasonable approximations, this is expected with approximation of smooth solutions.

Figure 4.17: Error norm for excess pore pressure vs number of DOF with different polynomial orders $((r^1 = 2, r^2 = 1), (r^1 = 3, r^2 = 2), (r^1 = 4, r^2 = 3), (r^1 = 5, r^2 = 4))$.

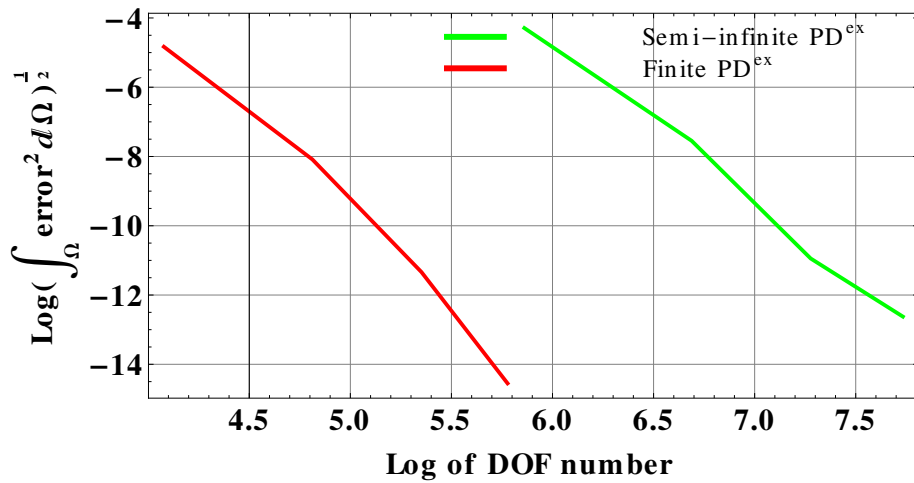
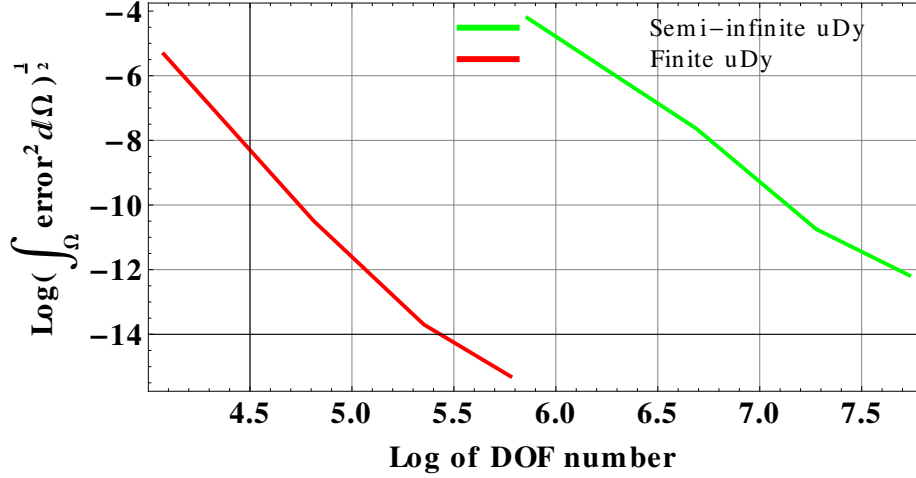


Figure 4.18: Error norm for displacement in y direction vs number of DOF with different polynomial orders $((r^1 = 2, r^2 = 1), (r^1 = 3, r^2 = 2), (r^1 = 4, r^2 = 3), (r^1 = 5, r^2 = 4))$.



4.4 Mass source injection into a bounded infinite poroelastic medium

Analytic expressions

In order to validate 2D calculations, the analytical solution by Cleary (1979) was presented. It was corrected by Rudnicki (1986), and it calculates the poroelastic response under plain strain condition to constant fluid mass injection/production into a bounded infinite poroelastic medium (figure 4.19).

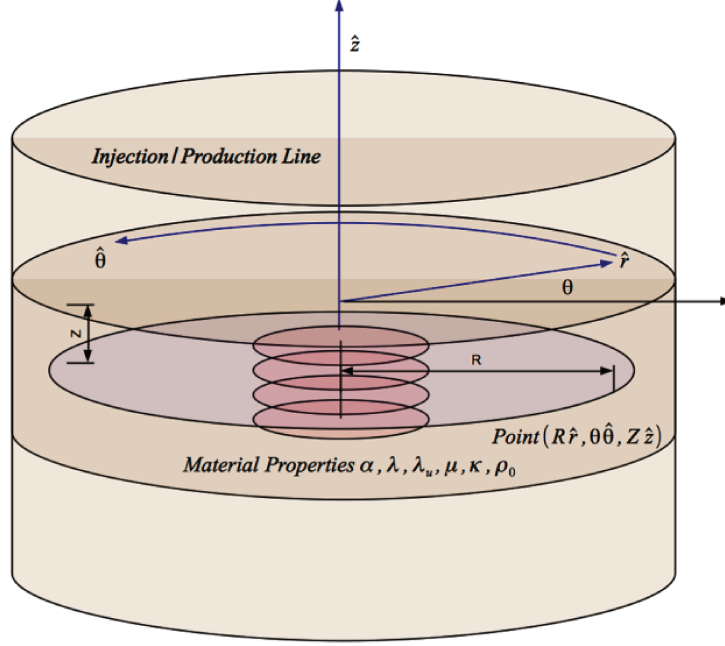
Solutions for continuous fluid mass injection rate q per unit of length L_{line} can be obtained by the superposition of the solution of instantaneous injection of a amount of fluid Q at one time (Rudnicki, 1986). As a result of this superposition, fluid mass change is

$$m(r, t) = \frac{q}{4\pi c} E_1\left(\frac{r^2}{4ct}\right) \quad (4.8)$$

where

$$E_1(z) = \int_z^\infty s^{-1} e^{-s} ds \quad (4.9)$$

Figure 4.19: Schematic representation of line mass source.



for small values of this argument $E_1(z) \approx -\varrho - \ln(z)$, where $\varrho = 0.57721$ is Euler's constant. The expressions for the displacement, excess pore pressure, and effective stress are

$$\mathbf{u} = \frac{q\alpha}{8\pi\rho_{fluid}\frac{\kappa}{\eta}(\lambda + 2\mu)} \left\{ \left(\frac{4ct}{r^2} \right) \left[1 - e^{-\frac{r^2}{4ct}} \right] + E_1 \left(\frac{r^2}{4ct} \right) \right\} \{x \mathbf{1}_x + y \mathbf{1}_y\} \quad (4.10)$$

$$P^{ex} = \frac{q}{4\pi\rho_{fluid}\frac{\kappa}{\eta}} E_1 \left(\frac{r^2}{4ct} \right) \quad (4.11)$$

$$\sigma = \frac{q\alpha\mu}{4\pi\rho_{fluid}\frac{\kappa}{\eta}(\lambda + 2\mu)} \left\{ (I - 2 \mathbf{1}_r \otimes \mathbf{1}_r) \left(\frac{4ct}{r^2} \right) \left[1 - e^{-\frac{r^2}{4ct}} \right] - I E_1 \left(\frac{r^2}{4ct} \right) \right\} \quad (4.12)$$

$$\sigma_t = \frac{q\alpha\mu}{4\pi\rho_{fluid}\frac{\kappa}{\eta}(\lambda + 2\mu)} \left\{ (I - 2 \mathbf{1}_r \otimes \mathbf{1}_r) \left(\frac{4ct}{r^2} \right) \left[1 - e^{-\frac{r^2}{4ct}} \right] \right\} \quad (4.13)$$

Dimensionless forms of these equations result from the use of the group of dimensionless variables given in Table 2.1.

Pressure stress coupling ratio PSC

During fluid injection into reservoirs or depletion from reservoirs pressure perturbations occur. Repeated measurements of stress and pore pressure during the depletion of oil fields

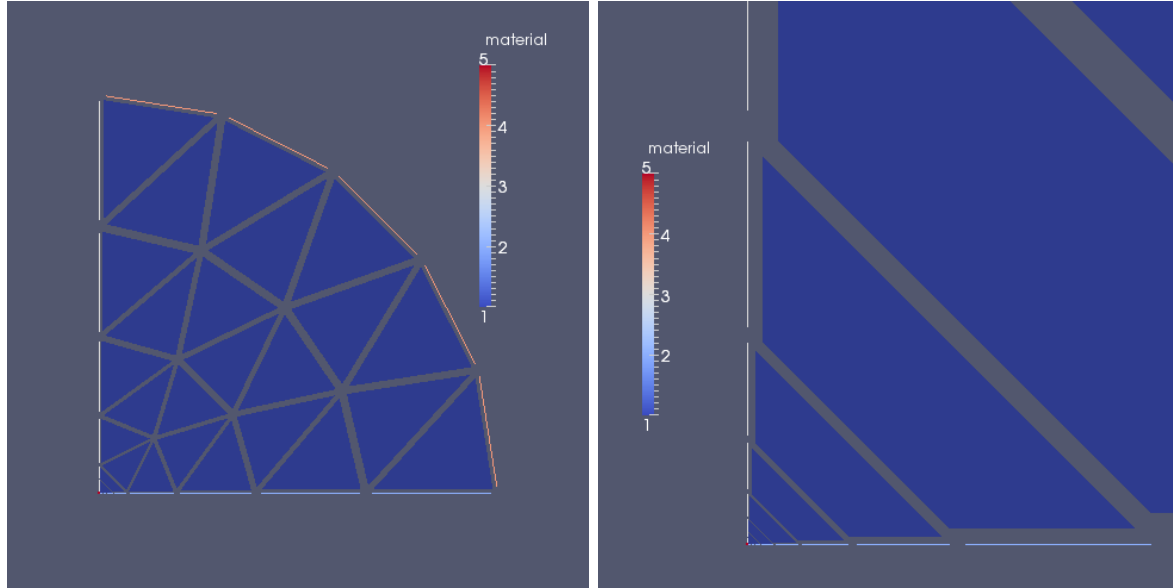
show that excess pore pressure ΔP^{ex} and horizontal stress changes are coupled. Heidbach (2010) mathematically showed the maximum value of $\frac{\Delta \sigma}{\Delta P^{ex}}$ PSC ratio from the long-term limit. By knowing the initial pore pressure and stress field, the spatio-temporal evolution of excess pore pressure and horizontal stress changes caused by fluid injection/production from mass sources is:

$$\frac{\Delta \sigma}{\Delta P^{ex}} = \frac{\alpha \mu}{(\lambda + 2\mu)} I \quad (4.14)$$

This means that for long times of constant fluid injection/production the excess pore pressure and the stresses rise a constant changes for each volume of fluid removed from the rock, thus areas with considerable long times of average constant injection or production may be near to this long term, if the rock behavior is assumed linear.

Initial and boundary conditions

Figure 4.20: Geometric mesh with directional refinement at line source. Below) Table shows dimensionless variables corresponding to values in table 4.2.



α	S_{rD}	λ_D	μ_D	$\sigma_{tD\ n}$	P_D^{ex}	q_D	ξ	Δt_D
0.7	0.790984	1.00818	0.668069	0	0	1.0	0.5	$1.0 \cdot 10^{-5}$

Figure 4.20 shows the setup of the 2D plane quarter-domain FE-model. The problem has 2 planes of symmetry. Heidbach (2010) uses the parameters presented in table 4.2. Initial conditions are assumed zero and boundary conditions are:

- An injection point (red point) located at the center *e.g.* intersection of symmetry lines
- Symmetry lines have non flux and null displacements in x direction for blue line and y direction for withe line.
- Far field contour is a free normal stress and drained condition (red line).

Here, a zero dimensional element is used (Point element located in corner, see Figure 4.20) to represent the mass line source. For this problem the dimensionless time step is small due to the need to compare secondary variables, in other words, it is indispensable to have a good match in state variables (excess pore pressure and displacements). The spatio-temporal evolution of PSC was computed for long times. Heidbach (2010) computed the poroelastic response of Rudnicki (1986) three-dimensional solution with a homogeneous 2D axis-symmetric FE model and solved the poroelasticity equations using a commercial software package ABAQUS / StandardTM. Similarly, this modeling was based on a 2D version of Rudnicki (1986) analytic solution under plane strain conditions, modeled with LPA.

For long times $t_D = 10.0$, 2D solutions converge to the same PSC ratio of tangential stresses in 3D solutions $\frac{\alpha\mu}{(\lambda+2\mu)} = \frac{\alpha(1-2\nu)}{2(1-\nu)}$ (Heidbach, 2010). This limit is one half of the radial stress limit. Assuming $a = 0.7$ and $\nu = 0.3$, the PSC ratio for long times is equal to 0.2 (figure 4.25).

Table 4.2: Model parameters for line mass source solution (Rudnicki, 1986). SI units.

q $\left[\frac{kg}{s}\right]$	ρ_{fluid} $\left[\frac{kg}{m^3}\right]$	λ_u $[Pa]$	λ $[Pa]$	μ $[Pa]$	α	L $[m]$	$\frac{\kappa}{\eta}$ $\left[\frac{m^2}{Pa \cdot s}\right]$	P_0^{ex} $[Pa]$
20.0	1000.0	$13.4 \cdot 10^9$	$8.3 \cdot 10^9$	$5.5 \cdot 10^9$	0.7	$25 \cdot 10^3$	$1.11 \cdot 10^{-11}$	$\frac{q}{\rho_f \frac{\kappa}{\eta} L_{line}}$

Numerical Results

Figures 4.21, 4.22, 4.23 and 4.25 show a comparison between numerical and analytical excess pore pressure, stresses and PSC ratio distributions along different plot lines. Computed excess pore pressure, stress distributions and PSC ratios fit the analytical solutions.

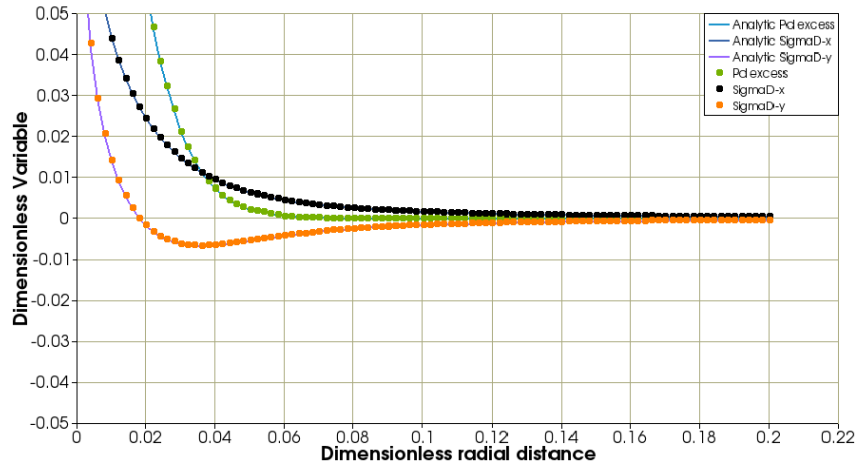
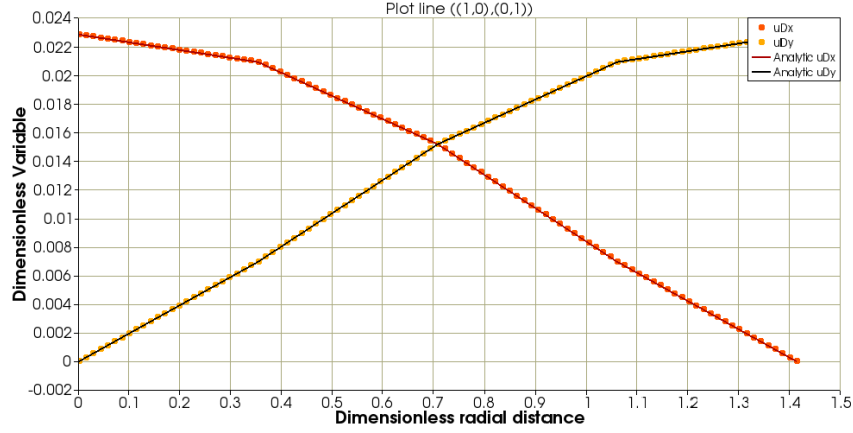
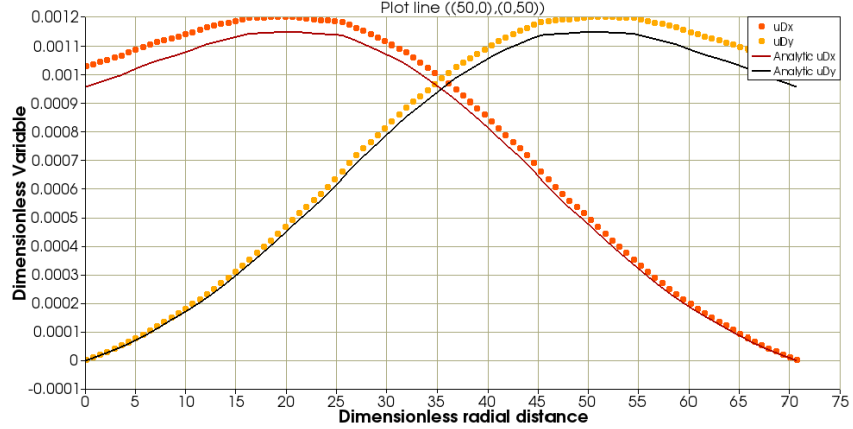
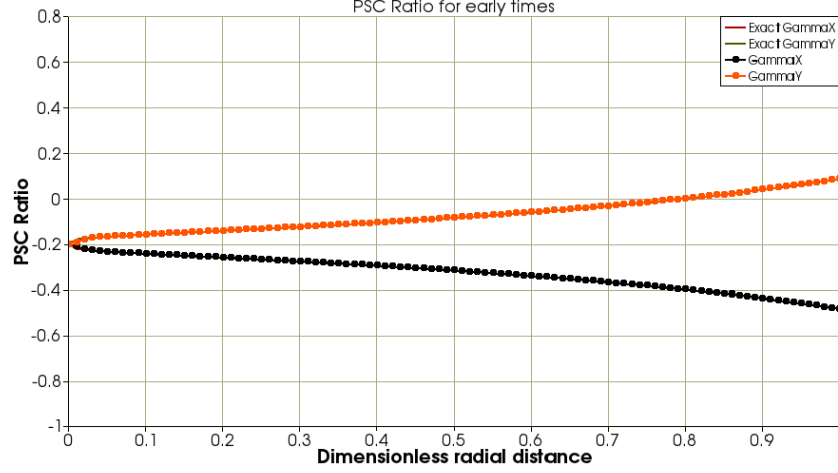
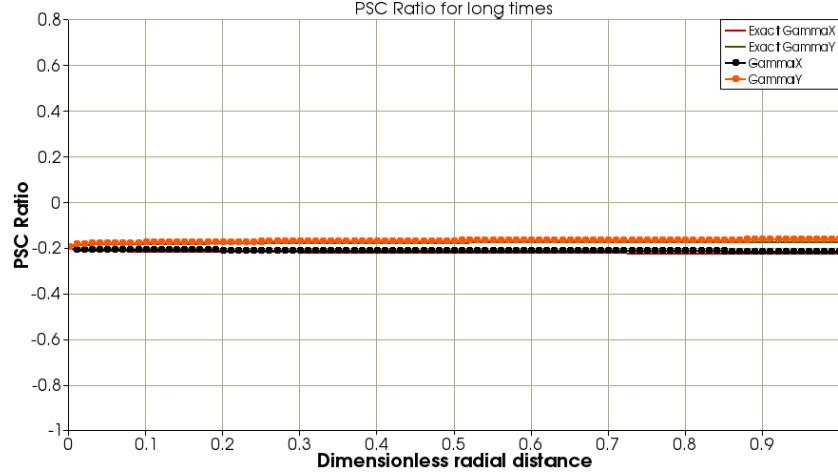
Figure 4.21: Dimensionless P_D^{ex} , σ_{Dx} , and σ_{Dy} at $t_D = 0.1$. Plot line $((0,0),(0.2,0))$.Figure 4.22: u_D near to injection point at $t_D = 0.1$. Plot line $((1,0),(0,1))$.Figure 4.23: u_D far from injection point u_{Dx} at $t_D = 0.1$. $((50,0),(0,50))$ 

Figure 4.24: PSC ratio at $t_D = 0.1$. Plot line $((0,0),(1,0))$.Figure 4.25: PSC ratio at long times $t_D = 10$. Plot line $((0,0),(1,0))$.

Close to the injection point excess pore pressure is larger than the stress changes. With increasing distance to the injection, point excess pore pressure decreases more rapidly than the stress changes. This leads to an intersection point of the pore pressure profile with the σ_x profile. The location of this intersection point depends on the duration of injection. The y direction stress changes, *i.e.* σ_y along the x direction, even become slightly negative before converging towards zero with distance, this means that the induced total stress change is compressive. For two-dimensional LPA approximation, figure 4.23 shows that the numerical results fit those values at the injection point, and diverge with the increase in distance from the point source. In addition calculations in displacements are overestimated from $x_D > 1.0$, since the numerical approximation uses an unbounded elastic to model an infinite bounded domain. Analytical long-term limit of PSC ratio of

0.2 is obtained with the two-dimensional solution for radial stresses as in Heidbach (2010) for tangential stresses.

4.5 Summary

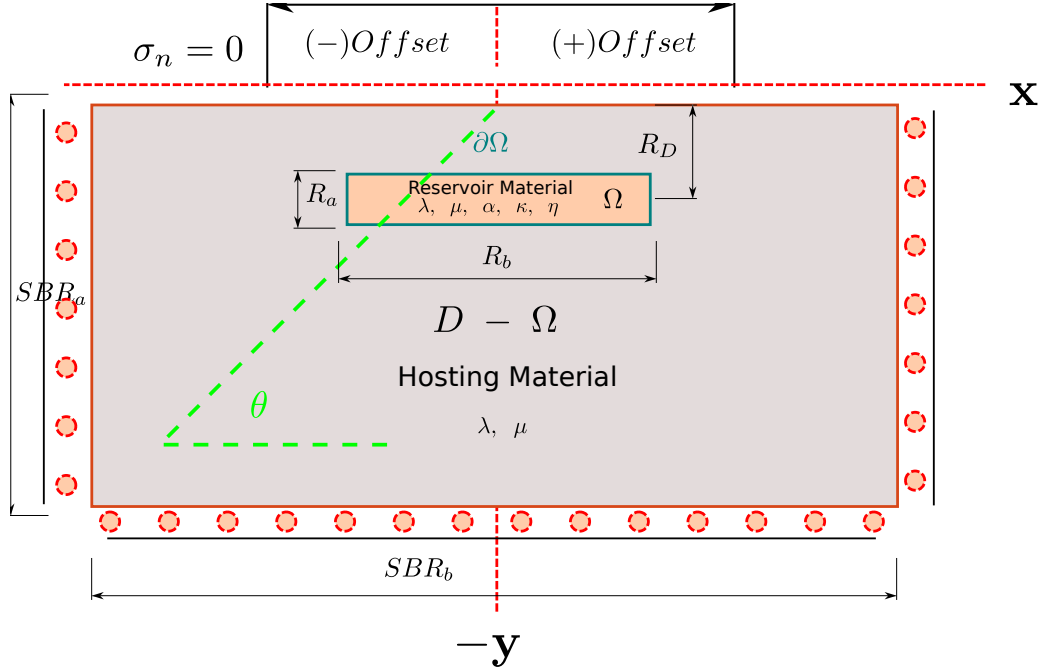
In this chapter, a brief description for the NeoPZ environment and LPA implementation was shown. LPA was based on three principal classes that interact to solve a poroelastic problem with the finite element procedures given in chapter 3. A multiphysics point of view was inherited from NeoPZ. LPA validation was presented in terms of 1D and 2D dimensional modeling and error norm charts were given for one-dimensional cases showing the convergence of LPA to analytic solutions, validating the implementation.

5. Fault reactivation

In this section, a series of calculations are presented to illustrate the problem of reactivation and its corresponding numerical approximation with the suggested implementation, showing several advantages over analytical approaches. Also, the effect of various parameters as reviewed in chapter 1 is shown.

5.1 The rectangular reservoir problem

Figure 5.1: Rectangular reservoir inclusion and boundary conditions.



Consider the rectangular reservoir presented in figure 5.1, where R_a , R_b , SBR_a , SBR_b , represent respectively: reservoir thickness, reservoir extension, and side burden rock di-

mensions. R_D is the reservoir depth measured from surface to reservoir top plus one half R_a . The rectangular inclusion is depleted $\pm\Delta P^{ex}$ (*e.g.* $\Delta P^{ex} < 0$ represents oil production) for all $x \in \Omega$ (*e.g.* homogeneous excess pore pressure distribution). Mechanical conditions for side burden rocks are zero normal stress at surface $\sigma_n = 0$, lateral boundary displacements in x direction are zero, bottom boundary displacements in y direction are zero. The problem is to find the stress changes due to reservoir depletion with the corresponding boundary conditions.

Comparison of LPA computations with other numerical approximation (STARS simulator) are given in the next section by contrasting with equation 2.74 representing the solution given in Hawkes (2009).

LPA Calculations

Using the material properties given in Table 5.1 and $\Delta P^{ex} < 0$ (*e.g.* depletion) and the computational mesh presented in figure 5.2, the calculations of γ due to poroelastic inclusion (blue color) are compared with results obtained using STARS.

Figure 5.2: Rectangular reservoir geometric mesh.

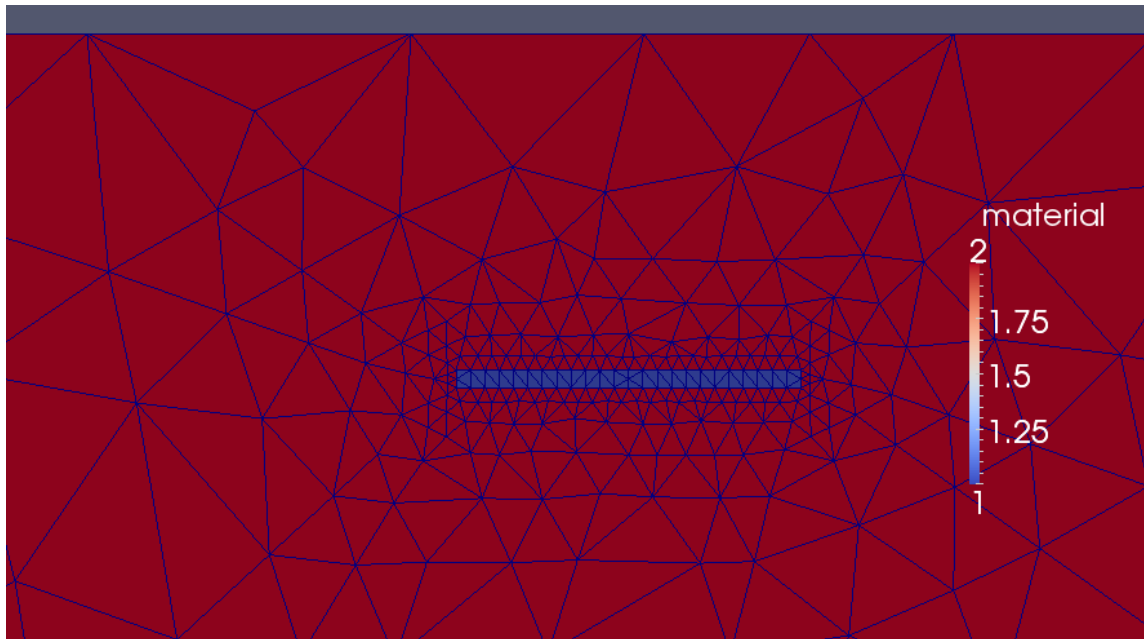


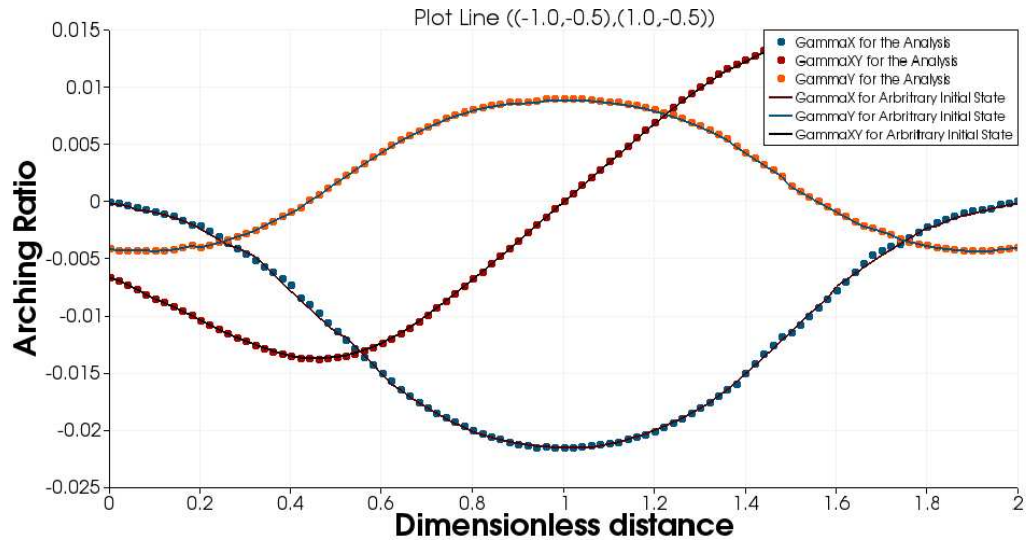
Table 5.1: Parameters for rectangular reservoir and side rocks with similar elastic moduli. All these parameters are in SI units. The model geometry has been normalized by R_D .

Mat	λ	μ	λ_u	α	ΔP_D^{ex}	r^1	r^2	ξ	Δt_D
Reservoir	$8.1 \cdot 10^9$	$5.4 \cdot 10^9$	$1.0 \cdot 10^{10}$	0.8	-1.0	3	2	0.5	0.0001
Side rocks	$8.1 \cdot 10^9$	$5.4 \cdot 10^9$	$1.0 \cdot 10^{10}$	—	0.0	3	2		

R_a	R_b	SBR_a	SBR_b
0.05	1.0	10.0	20.0

It is important to point out that the formulation here is linear and the initial static state is a solution that can be separated from the stress and pore pressure excess changes. Figure 5.3 shows the calculations given in this section (dotted lines) compared with calculations including an arbitrary initial state, by subtracting this initial state from the current solution at one specific time t , the same response is obtained, assuming zero initial conditions at the same specific time; *i.e.* the initial state is important to place the problem in a specific physic situation, but the stress and excess pore pressure changes determine the essential part of the reactivation in linear analysis. It is clear that for non-linear formulations and no static initial conditions, this is not possible. Nevertheless, following equation 2.79, the sign τ depends on the faulting regime acting on (*e.g.* normal faulting or reverse faulting stress regimes) the initial condition (Hawkes, 2009).

Figure 5.3: Arching ratios obtained from arbitrary initial state compared with the zero initial state calculations. Arching ratios normalized by $\frac{(1-2\nu)}{(1-\nu)}$.



Figures 5.4, 5.5 and 5.6 show vertical horizontal and shear arching ratios calculated with LPA. From equation 2.77, please note that zero contour represents the change of sign in stress and, following the conventional sign in continuum mechanics, compression is negative, so the positive values of γ in this contours represents compression since $\Delta P^{ex} < 0$ as in Hawkes (2009).

Figure 5.4: Horizontal arching ratio for rectangular reservoir computed with LPA. Arching ratio normalized by $\frac{(1-2\nu)}{(1-\nu)}$.

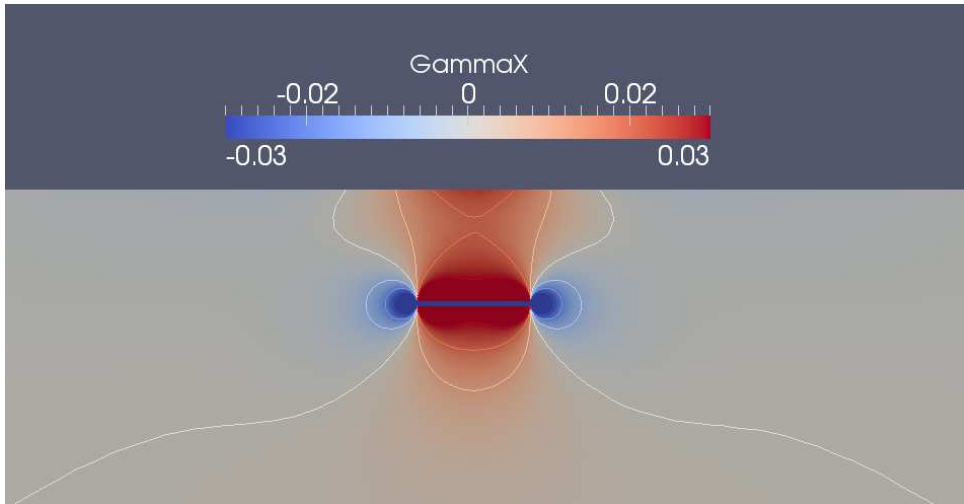


Figure 5.5: Vertical arching ratio for rectangular reservoir computed with LPA. Arching ratio normalized by $\frac{(1-2\nu)}{(1-\nu)}$.

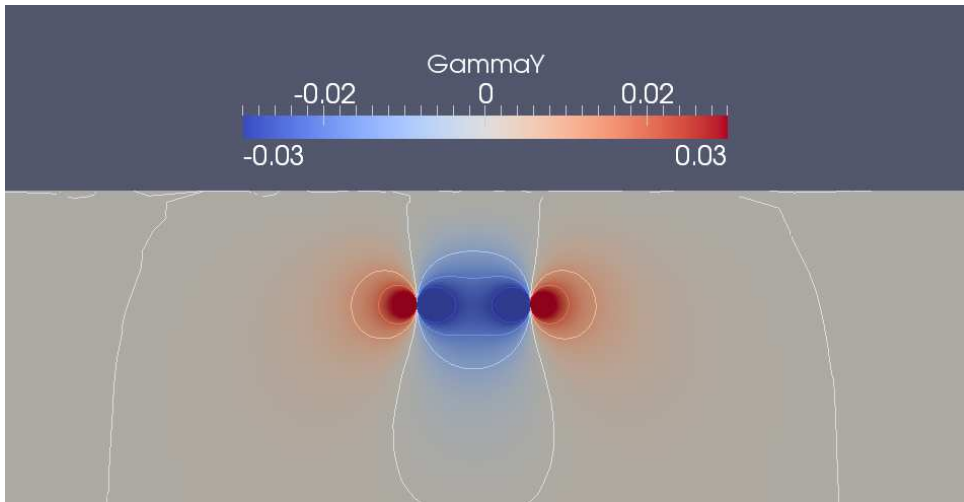
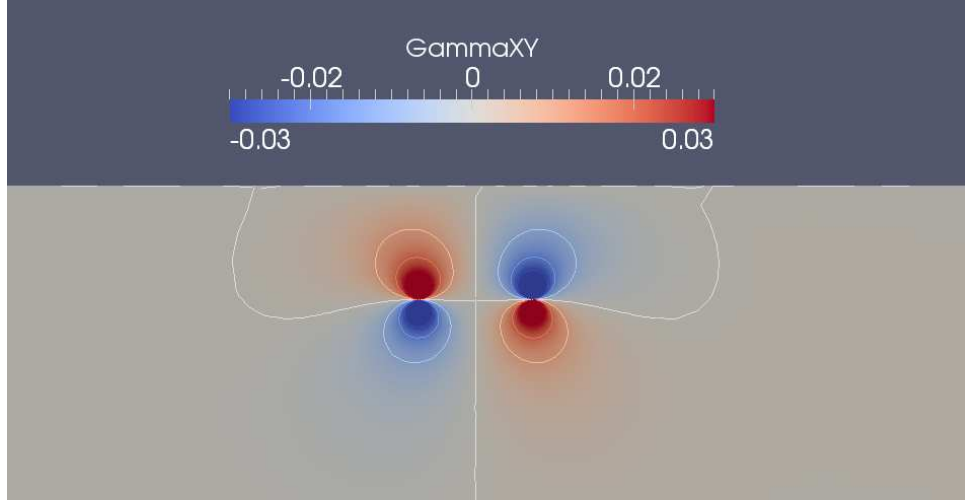


Figure 5.6: Shear arching ratio for rectangular reservoir computed with LPA. Arching ratio normalized by $\frac{(1-2\nu)}{(1-\nu)}$.



STARS Calculations

STARS is a coupled fluid flow and geomechanics simulator developed by Computer Modelling Group Ltd. (Calgary, AB, Canada) and used extensively by the petroleum industry worldwide. The fluid flow model is a multiphase, multicomponent reactive flow, that can simulate the injection and flow of gases, solvents, polymers, surfactants, and other chemicals. It can be run isothermally or not. The geomechanics module can simulate linear and non-linear elasticity, elastoplasticity and viscoelasticity behavior, as well fracturing effects.

The geometric mesh is composed of 301 cells in j direction and 321 cells in k direction with different cell dimensions near the reservoir. Please note that for this model, discussion about dimension are irrelevant since spatial data is scaled for comparison purposes. Thus, the relation between reservoir thickness - extension and its depth must be the same for comparison purposes.

In this example, there is one well producing from the centre of the reservoir during a given time and after this period, it is shut-in until a homogeneous excess pore pressure distribution is obtained. This final step is used to calculate the stress changes. Figure 5.7 shows the contours of σ_x that have the same shape that the contours in figure 5.4. It is important to point out that null contour is independent of how the variables are scaled, since the null contour is invariant after non-dimensionalization (*i.e.* the null contour shown in figure 5.4 has exactly the same shape of $\sigma_x = 0$ shown in figure 5.7).

Since the solution in Hawkes (2009) is in dimensionless forms, σ computed by STARS is

normalized with $\frac{(1-2\nu)}{\alpha\Delta Pex(1-\nu)}$ to obtain the same values. Permeabilities and fluid viscosities used in STARS are arbitrary, because a stationary solution at a determinate time (homogeneous change in pressure), after shut-in time, is obtained. Hence, elastic parameters and Biot's coefficient are required be the same. In addition, it is necessary to disable thermal and plastic calculations in STARS to compute a pure linear elastic response. Data generate by STARS are computed on center points and middle point between cells faces. This data is smoothed with CMG post-processing tool (Results 3D) and used to plot figures 5.9 and 5.8.

Figure 5.7: σ_x contour for rectangular reservoir geometry using STARS. Visualization with Results 3D.

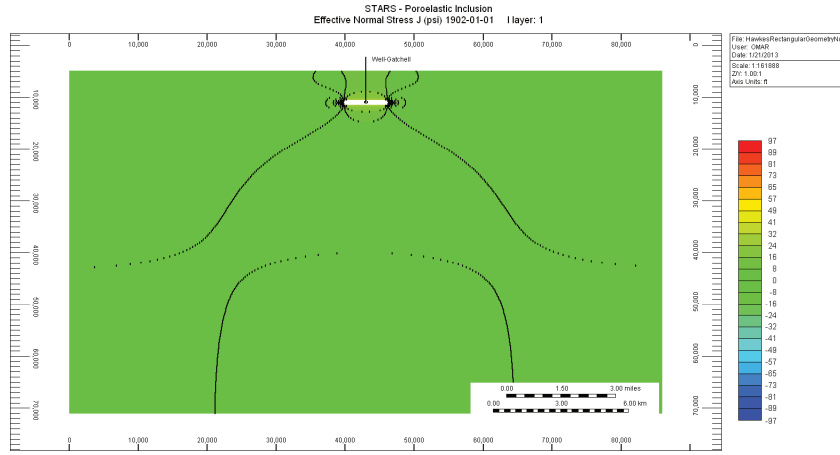


Figure 5.8 shows γ_x and γ_y along plot line $((0,0),(0,-2.0))$ with coordinates associated with figure 5.1. STARS results and LPA calculations fit Hawkes (2009) curves out of reservoir domain. However, STARS model is imprecise near to reservoir boundary (see figure 5.9) indicating that it is necessary to apply local refinement in this region as is illustrated in figure 5.2 for LPA geometric mesh.

Unfortunately STARS cannot use its mesh refinement tools when the geomechanics module is used. The natural way to improve the solution is to create a new grid with local refinement, increasing the number of DOF. On the other hand, LPA fits the curves, in and out reservoir domain.

For these models, the computational times do not exceed 3 minutes showing the accurate computations of LPA in comparison with commercial software STARS in terms of linear poroelasticity and mono-phasic flow. This example illustrates the validation of LPA in comparison with a commercial tool, modelling a rectangular reservoir as a poroelastic inclusion. Also, it is important to note that STARS is able to simulate more sophisticated and complex fluid flow models than hydromechanics problems.

Figure 5.8: γ_x, γ_y STARS solution comparison with LPA and Hawkes (2009) solution. Plot line $((0,0),(0,-2))$.

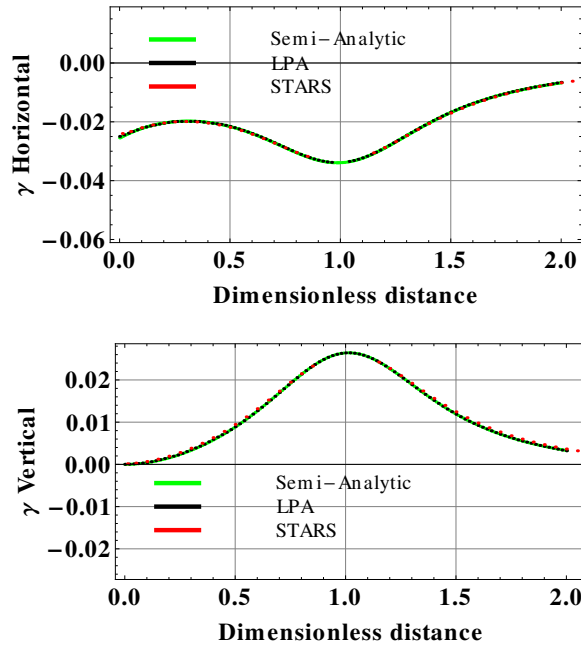
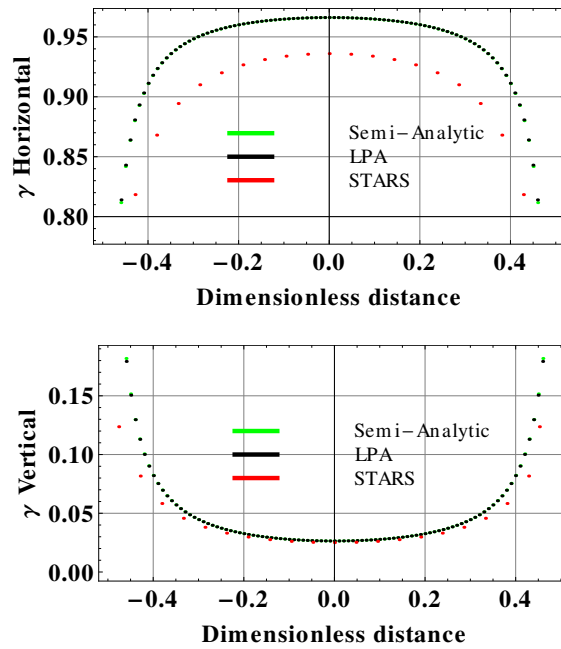


Figure 5.9: γ_x, γ_y STARS solution comparison with LPA and Hawkes (2009) solution. Plot line $((-0.5,-1),(0.5,-1))$.



Fault reactivation

Figures 5.10, 5.11 and 5.12 show λ_{FR} for faults inclined 60 degrees counter-clockwise from the positive x axis direction, at different offsets (offset represents the distance of the fault outcrop to the x axis origin, see Figure 5.1).

Figure 5.10: Fault reactivation factor for rectangular reservoir geometry, faults inclined 60 degrees. Bottom) λ_{FR} for far offset faults along fault planes. Arching ratio normalized by $\frac{(1-2\nu())}{(1-\nu)}$.

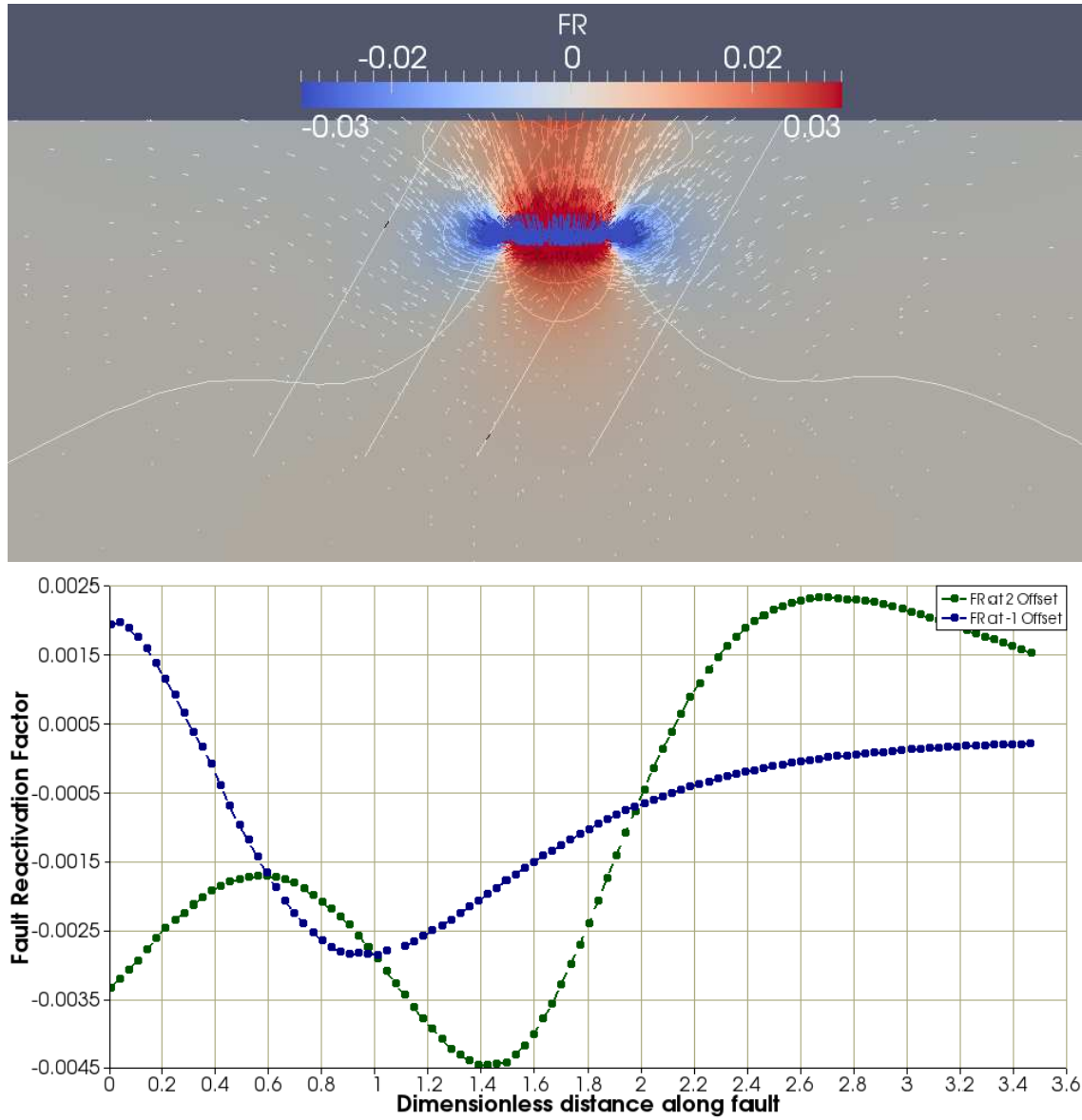


Figure 5.11: λ_{FR} along fault planes. Top) Fault at offset 0. Bottom) Fault at offset 1. λ_{FR} normalized by $\frac{(1-2\nu)}{(1-\nu)}$, ($\lambda_{FR} < 0$ tendency to reactivate).

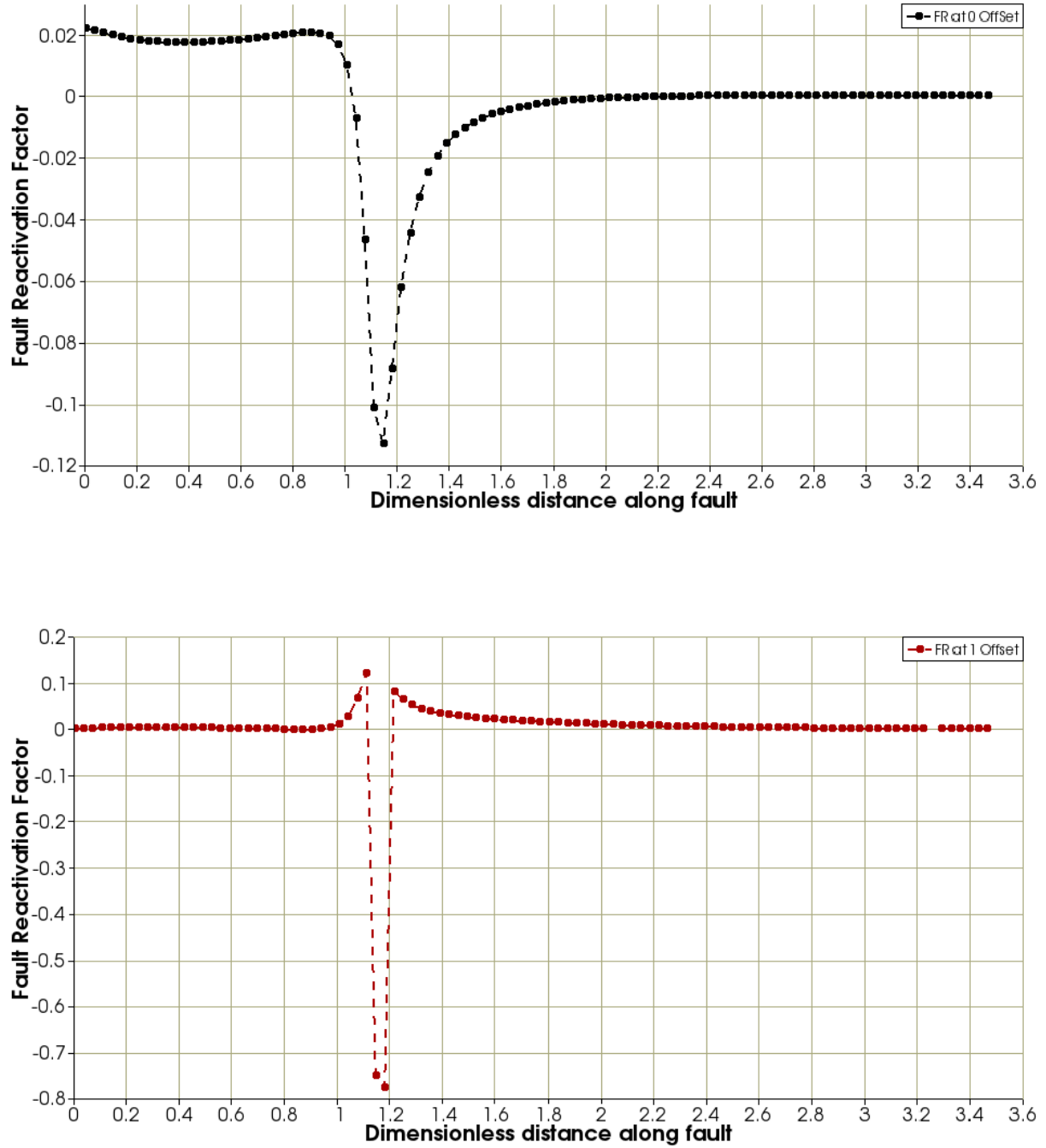
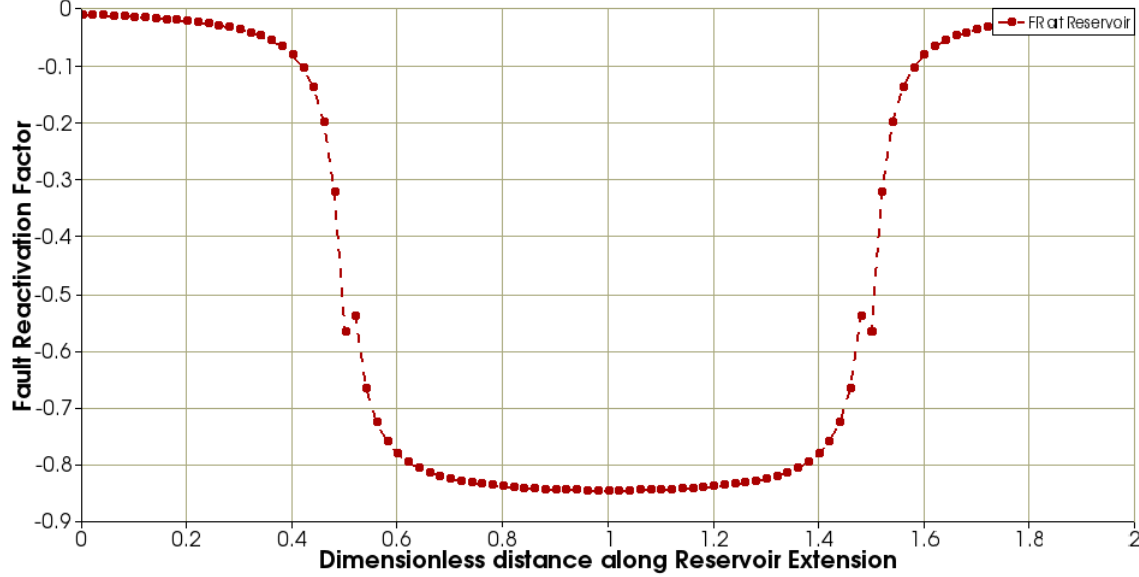


Figure 5.12: λ_{FR} along reservoir extension. λ_{FR} normalized by $\frac{(1-2\nu)}{(1-\nu)}$, ($\lambda_{FR} < 0$ tendency to reactivate).



The fault reactivation tendency analysis is based on mapping the null contour $\lambda_{FR} = 0$, since it represents the change in compression and tension stress state. Using the Table 2.2, any fault inclined at 60 degrees that is crossed by the null contour has a tendency to reactivate for negative values of λ_{FR} , and a tendency to stabilize for positive values λ_{FR} , when normal fault regime is assumed.

5.1.1 Fault reactivation threshold

Induced earthquake ΔCFS module as 0.1 MPa have been found to induce seismic activity in faulting settings where initial ΔCFS values are close to zero (Segall, 1992; Guyot and Volant, 1992; Rudnicki, 1999; Ferronato, 2008; Hawkes, 2009). If this value is assumed to be consistent with fault gouge in this example, it is possible to define a threshold value $\lambda_{FRt} = \frac{\Delta CFS_t}{\alpha \Delta p^{ex}} = \frac{0.1}{\alpha \Delta p^{ex}}$, and all negative values over this threshold strictly represent a strong tendency to reactivate. Thus, using $\alpha = 0.8$ and $\Delta p^{ex} = -10$ MPa, is equivalent to $\lambda_{FRt} = -0.0125$, and it can be interpreted in previously results as follows:

- Figure 5.10 shows that faults at far offsets, despite having negative values, the tendency to reactivate is null.
- Figure 5.11 shows that fault at offset 0 tends to reactivate at depths equivalent to the left reservoir flank.

- Figure 5.12 shows that any plane inclined 60 degrees crossing the reservoir reactivates along all reservoir extension. Consequently, the fault at offset 1 has a strong tendency in localized parts because it crosses the reservoir on the right flank.

5.1.2 Side burden dimensions

Another important question at this point is: which is the optimal size of the hosting material in order to avoid boundary effects?. According with Osorio (1992) it is important to minimize boundary effects is important in reservoir geomechanics modeling. This reduces the computational cost and makes reasonable solutions in regions possible near the reservoir rocks. Figure 5.13 shows dimensionless displacements computed with 2.72 for side burden rocks along depth and extensions. Displacements tend to zero but never reach this value for infinite behavior.

Table 5.2: Spatial ratios for different side burden dimensions with $\nu \approx 0.3$.

Ratio	$\frac{R_a}{SBR_a}$	$\frac{R_b}{RSBR_b}$	Line
Case1	$\frac{1}{40}$	$\frac{1}{4}$	Red
Case2	$\frac{1}{50}$	$\frac{1}{6}$	Green
Case3	$\frac{1}{100}$	$\frac{1}{5}$	Orange
Case4	$\frac{1}{100}$	$\frac{1}{10}$	Blue
Case5	$\frac{1}{200}$	$\frac{1}{20}$	Brown
Reference	$\frac{1}{400}$	$\frac{1}{40}$	Black

To illustrate the effect of boundaries, a reference model (Black line fitting Hawkes (2009) solution, figure 5.14) was used to evaluate differences between several hosting material dimensions presented in table 5.2. Based on figure 5.15 and table 5.2 the choice of case 5 has small errors (error was not quantified) in comparison with the reference model, but for practical modelling with the combination of case 2 with case 4, it is possible to capture infinite behavior with $\frac{R_a}{SBR_a} < \frac{1}{50}$, $\frac{R_b}{SBR_b} < \frac{1}{10}$. Thus, for a region defined by one rectangle with dimensions R_a and R_b , and hosting material with $\nu \approx 0.3$, it is modeled with small errors in displacements since γ is a secondary variable in LPA computations. If the interest is modeling regions near the reservoir, case 2 is a good option, because all cases in Table 5.2 were tested into reservoir domain without considerable differences in γ , but for brevity results are not shown here.

Figure 5.13: u_{Dy} , u_{Dx} dimensionless displacement as function of dimensionless depth and lateral extension. Plot line $((0,0)(0,20))$.

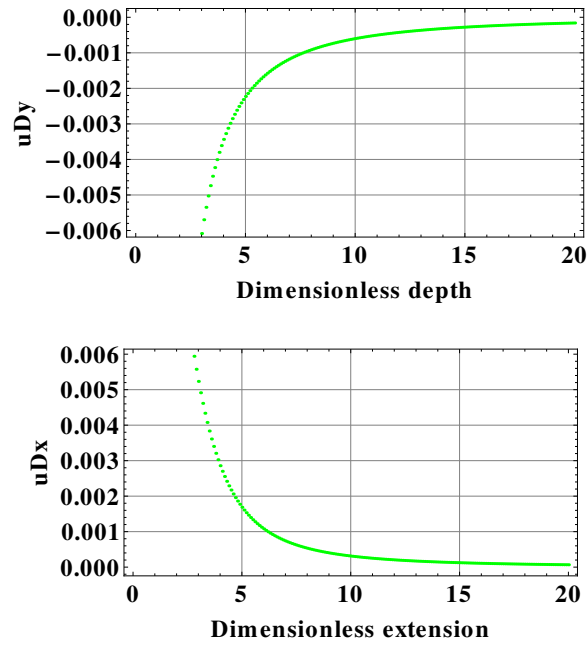


Figure 5.14: γ_x , γ_y arching ratios comparison with LPA reference solution (Black line in table 5.2). Plot line $((-2,-2)(2,-2))$.

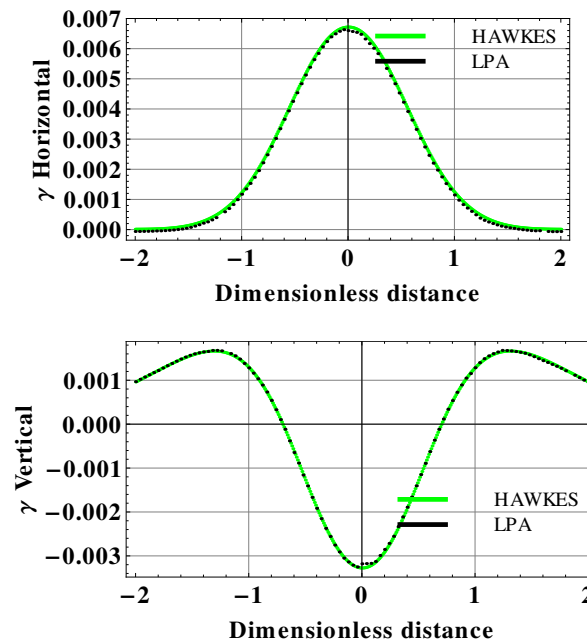
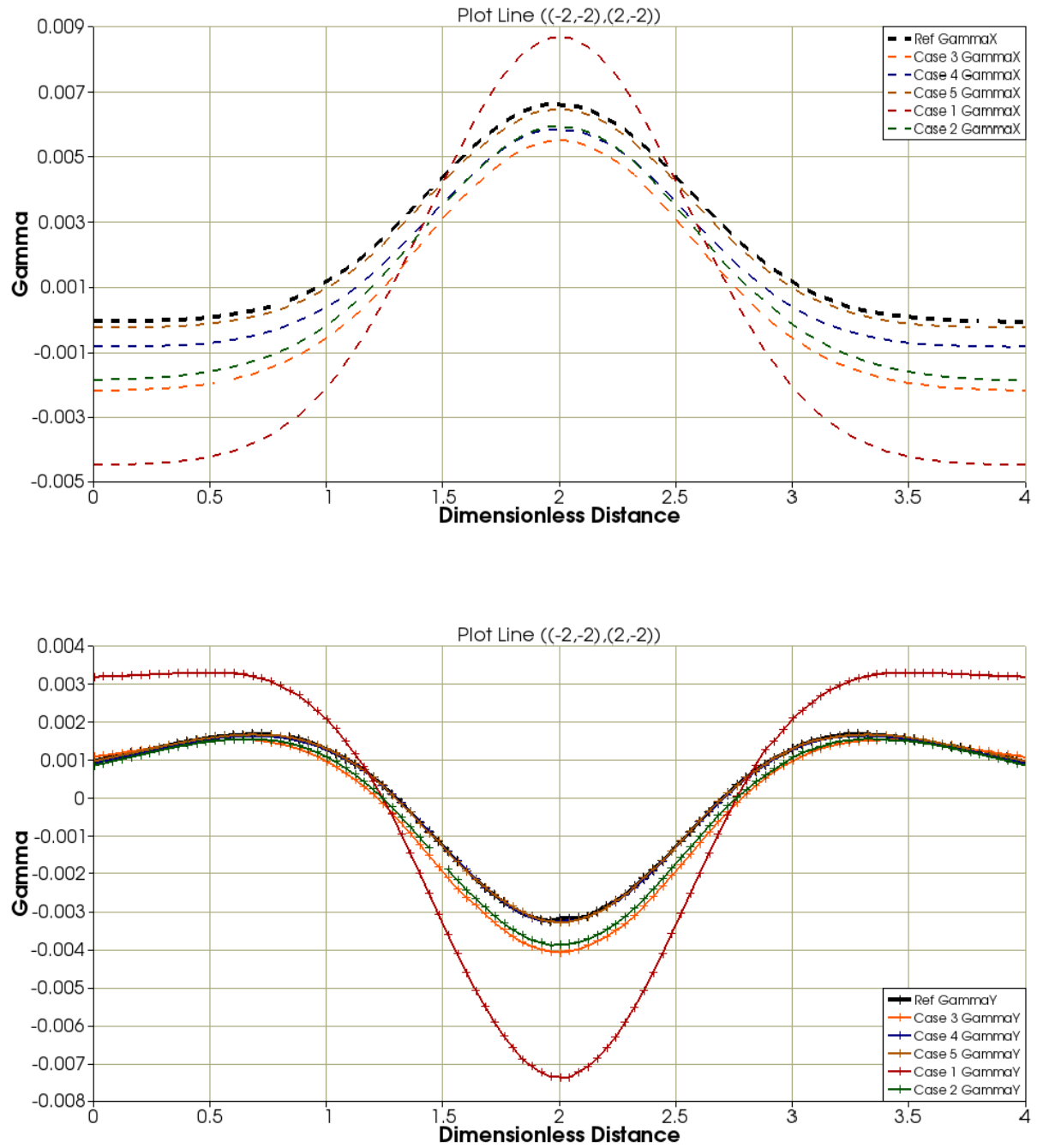
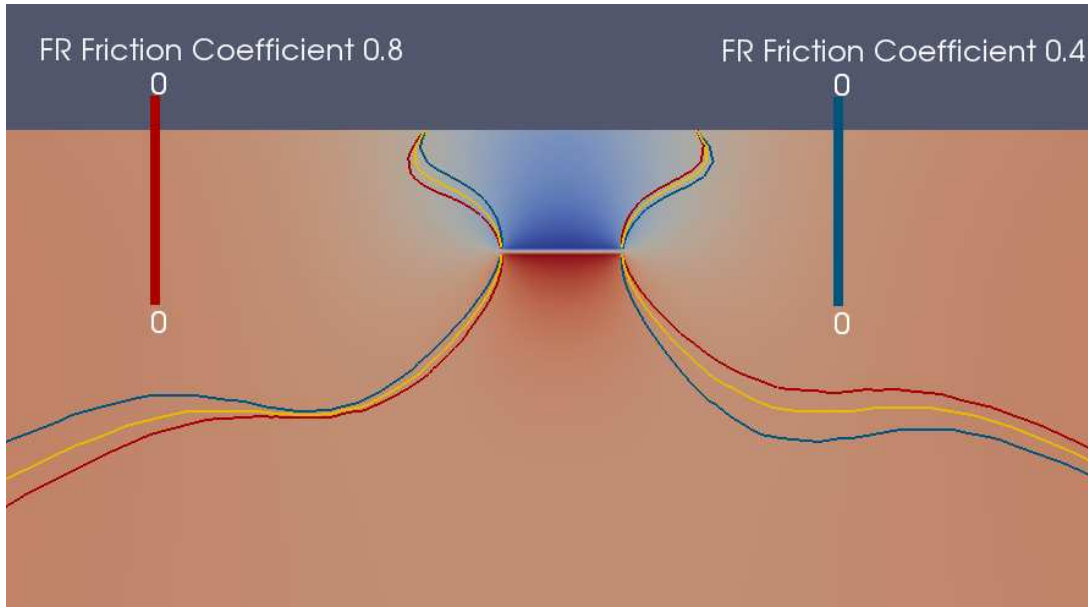


Figure 5.15: γ_x , γ_y lines for different hosting material sizes with $\nu \approx 0.3$.

5.1.3 Friction coefficient variation

Friction coefficient in most of rocks can vary from 0.4 to 0.8 for different brittle rocks materials (Hawkes, 2009; Germanovich, 2004). Figure 5.16 shows the effect of μ_s variation in the null contour, showing that for rectangular case there is no significant effect for faults inclined 60 degrees.

Figure 5.16: μ_s friction variation effect in zero λ_{FR} contour. Fault reactivation factor normalized by $\frac{(1-2\nu)}{(1-\nu)}$.



5.1.4 Material contrast

Material contrast is an important factor. In relation to initial case with similar elastic modules, two cases are presented:

- Case 1: soft side burden rocks with young modulus one tenth of the base case (*e.g.* $\lambda_{case1} = 0.1 * \lambda_{base}$ and $\mu_{case1} = 0.1 * \mu_{base}$).
- Case 2: rigid side burden rocks with young modulus ten times bigger (*e.g.* $\lambda_{case2} = 10.0 * \lambda_{base}$, $\mu_{case2} = 10.0 * \mu_{base}$).

Figure 5.17 shows that, with the same set of faults, soft side burden favors fault stability, and rigid side burdens favor fault reactivation, having a strong effect on fault reactivation factor. Please note that several negative regions are generated by soft reservoir compaction or contraction.

Figure 5.17: Stiffness effect on λ_{FR} . Top) Soft side burden. Bottom) Rigid side burden. Values normalized by $\frac{(1-2\nu)}{(1-\nu)}$.

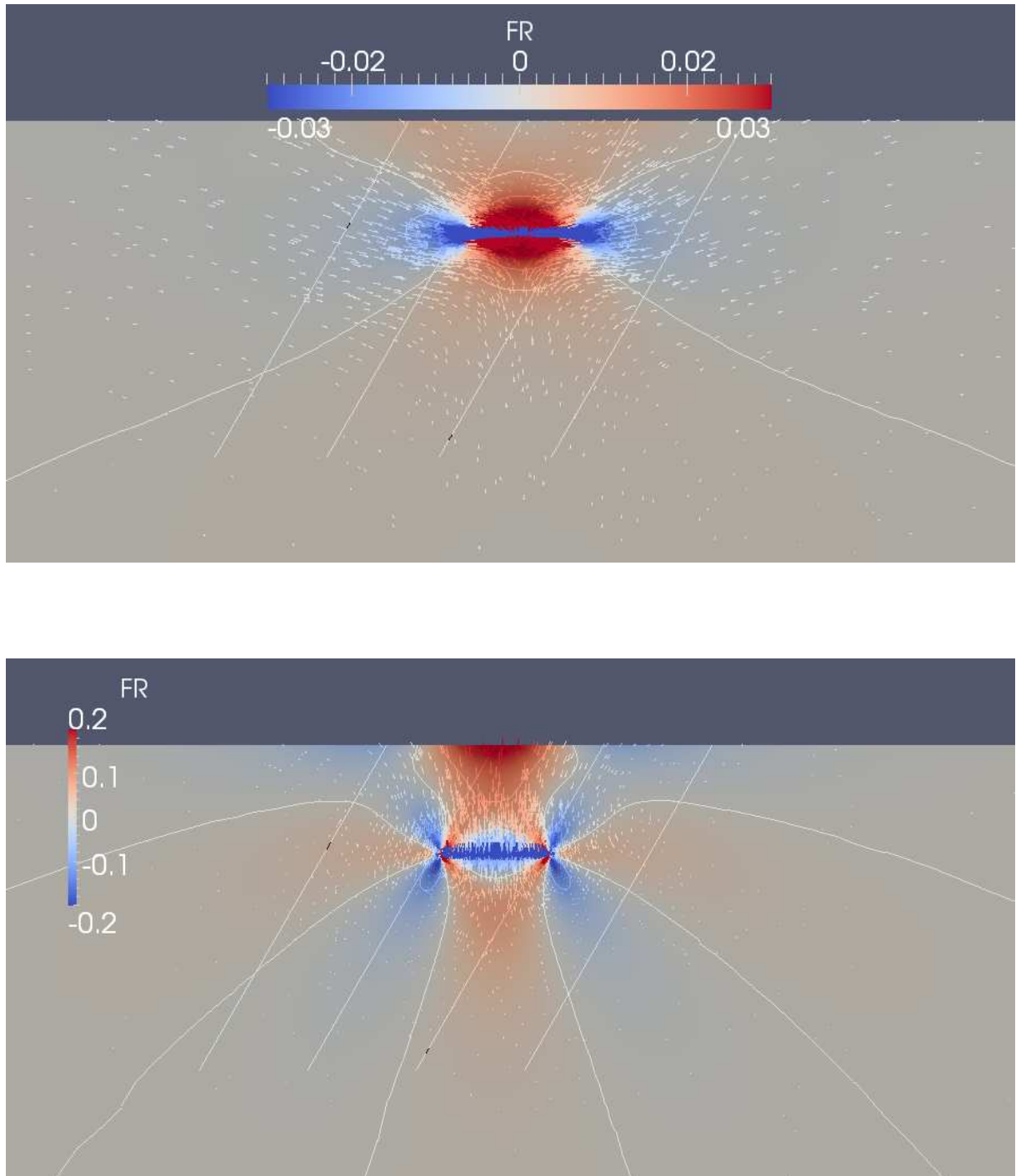


Figure 5.18: Reservoir inclination (45 degrees) effect on λ_{FR} . Fault reactivation factor normalized by $\frac{(1-2\nu)}{(1-\nu)}$.

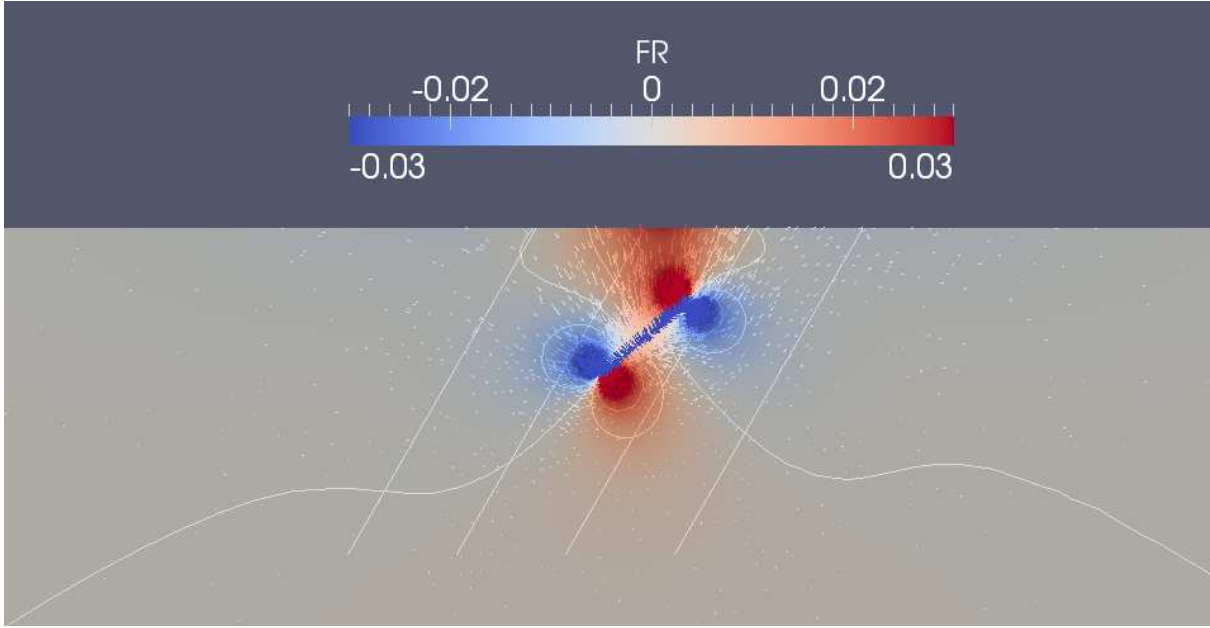
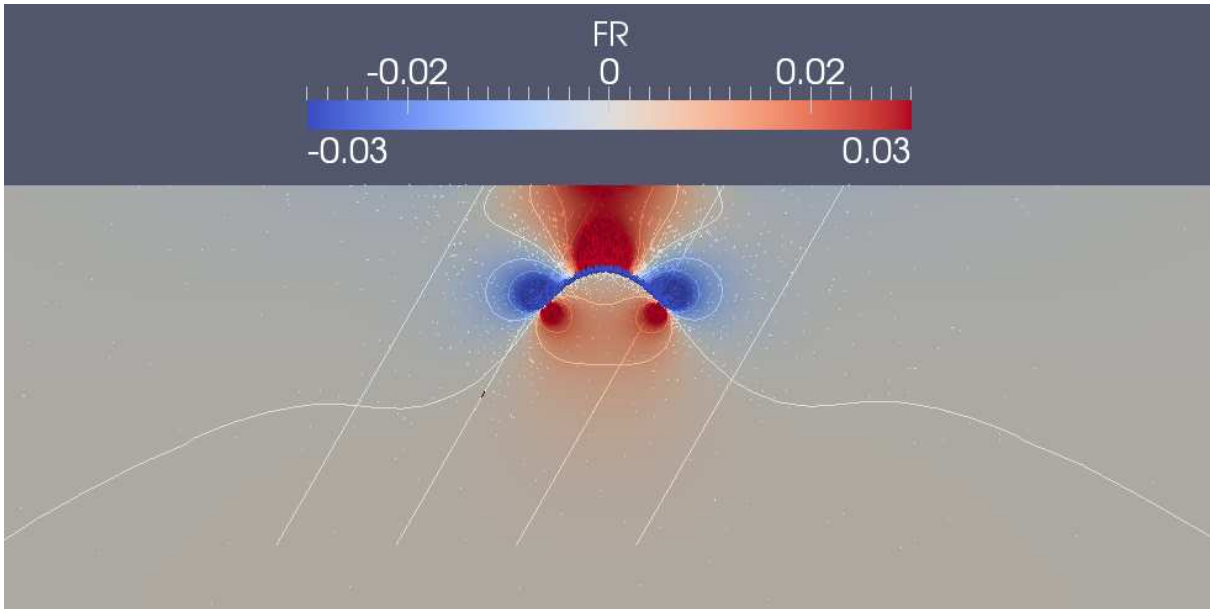


Figure 5.19: Anticline reservoir geometry effect on λ_{FR} . Fault reactivation factor normalized by $\frac{(1-2\nu)}{(1-\nu)}$.



5.1.5 Tilted reservoir

Reservoir inclination and geometry are important since they have a strong effect in λ_{FR} . Figure 5.18 shows that faults near the reservoir flanks have larger regions with tendency to reactivate than horizontal reservoir with the same depletion level.

5.1.6 Reservoir geometry

To analyze more complicated reservoirs, accounting for more realistic geometries, throughout this example the effect of reservoir shape is illustrated. Figure 5.19 shows that near the anticline flanks there are larger regions with tendency of reactivation in comparison with rectangular shape for the same depletion level.

All these effects represent changes in λ_{FR} null contour, but the pore pressure excess is not homogeneous and constant. However, it is possible to use previous solutions to obtain a rough approximation when the reservoir in general has a smooth change in pore pressure, thus the average pore pressure can be used to calculate γ and λ_{FR} factors. Nevertheless oil production programs represent no constant, no homogeneous pore pressure fields and they have an important effect on λ_{FR} distributions.

5.2 Reservoir with non-constant pressure distribution

In this section, fault reactivation analysis is used for different productions schemes, in order to evaluate the effect of reservoir depletion (non-constant pressure distribution) on fault reactivation tendency.

5.2.1 Reservoir depletion due to one well

Constant unit rate

One well producing at constant unit rate (*e.g.* $q_D = -1.0$) is draining the reservoir at different offsets in x direction, at a depth of one half of the reservoir thickness plus the reservoir top depth. All these cases use the same set of faults previously defined.

Figure 5.20: λ_{FR} for early times of unitary production at dimensionless time of $t_D = 0.06$. Bottom) Near offset fault planes. Well location at offset 0.

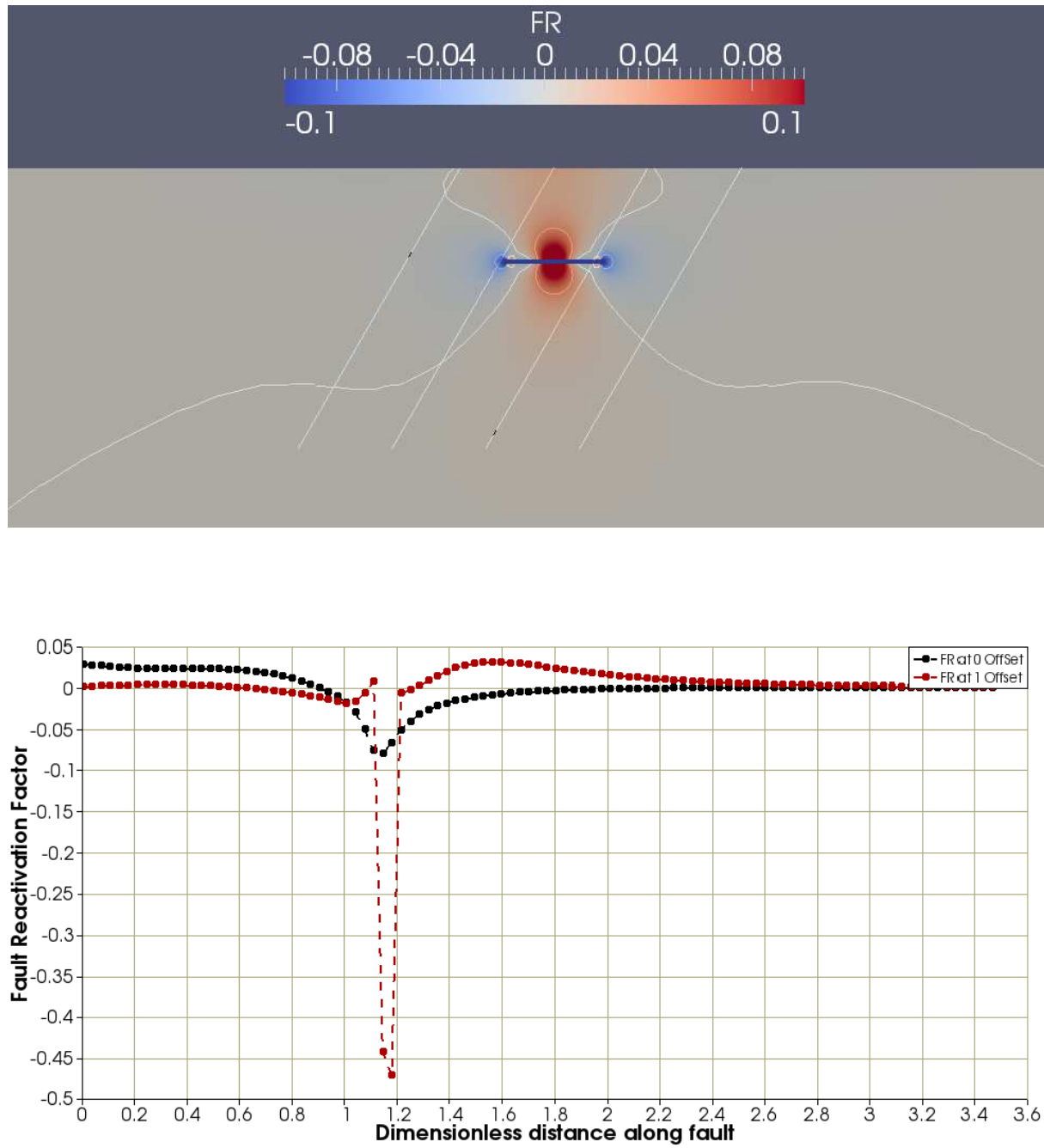


Figure 5.21: λ_{FR} for long times of unitary production, dimensionless time of $t_D = 0.09$. Bottom) Near offset faults planes. Well location at offset 0.

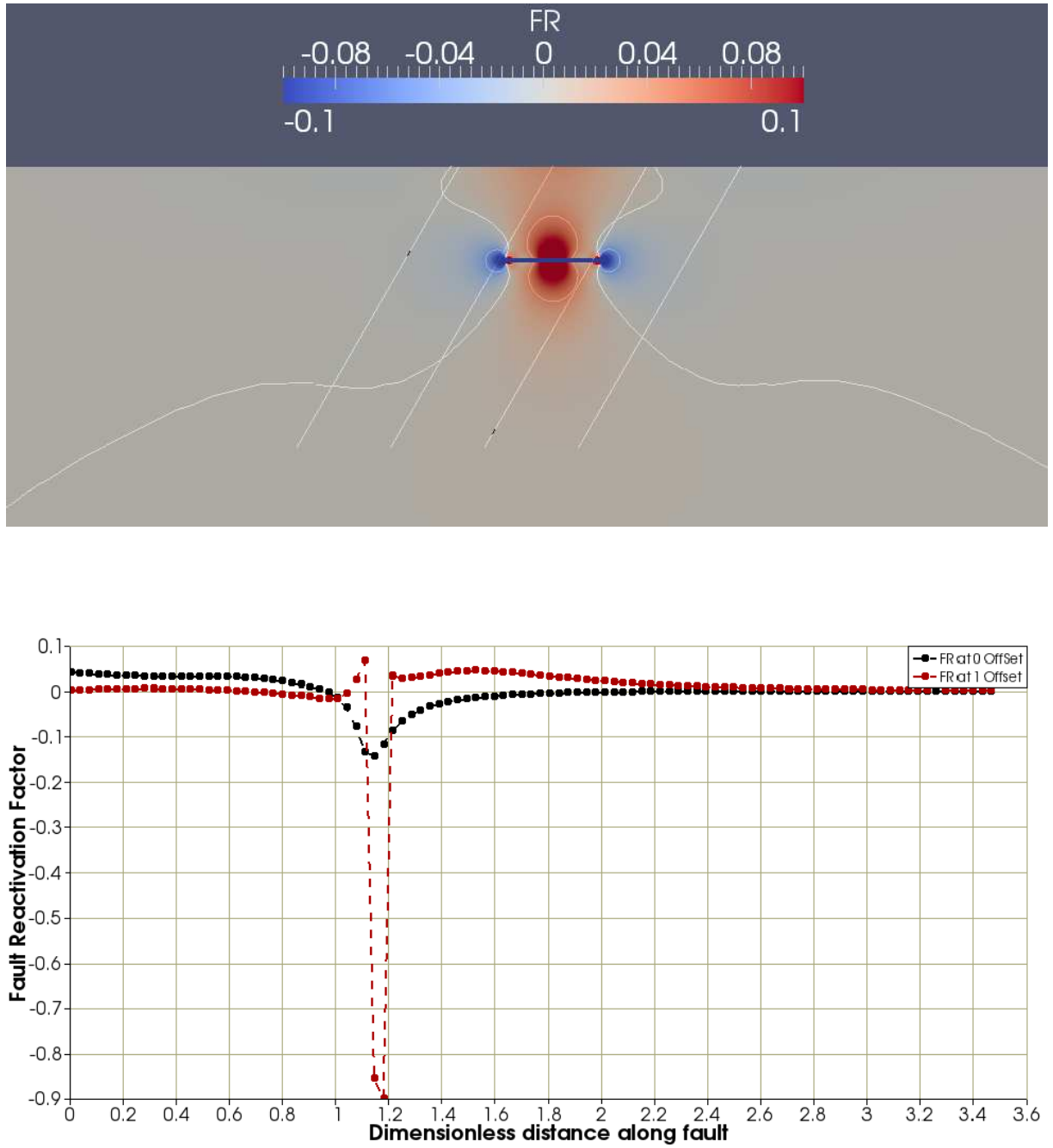


Figure 5.22: λ_{FR} for early times of unitary production at dimensionless time of $t_D = 0.06$. Bottom) Near offset fault planes. Well location at offset -0.4 .

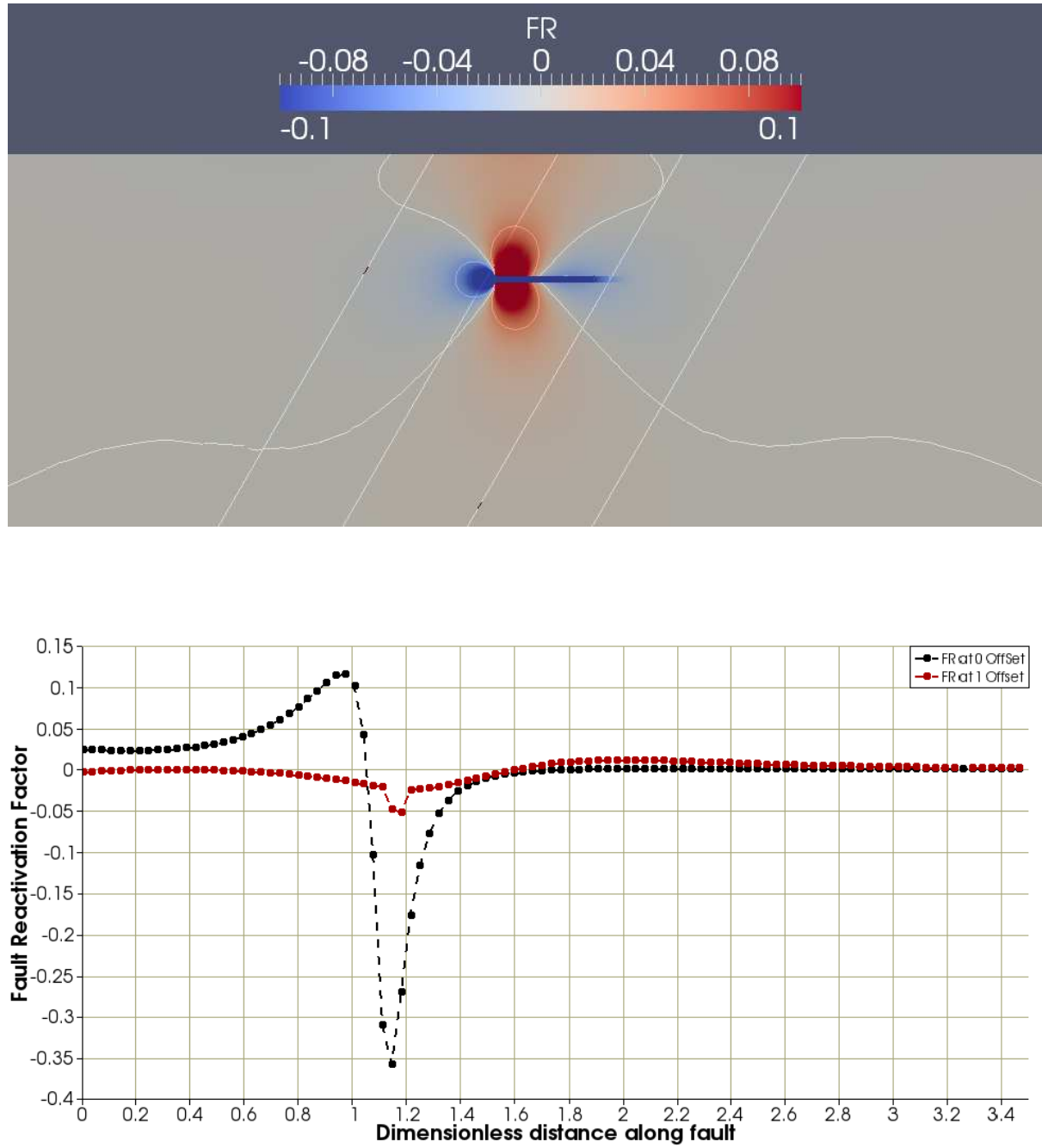
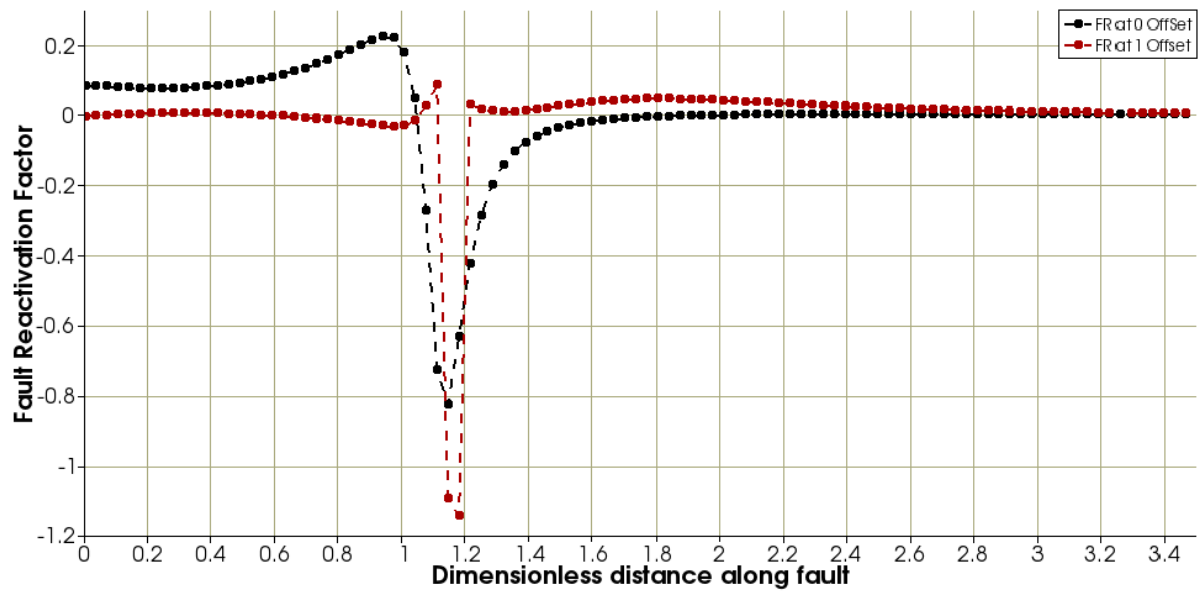
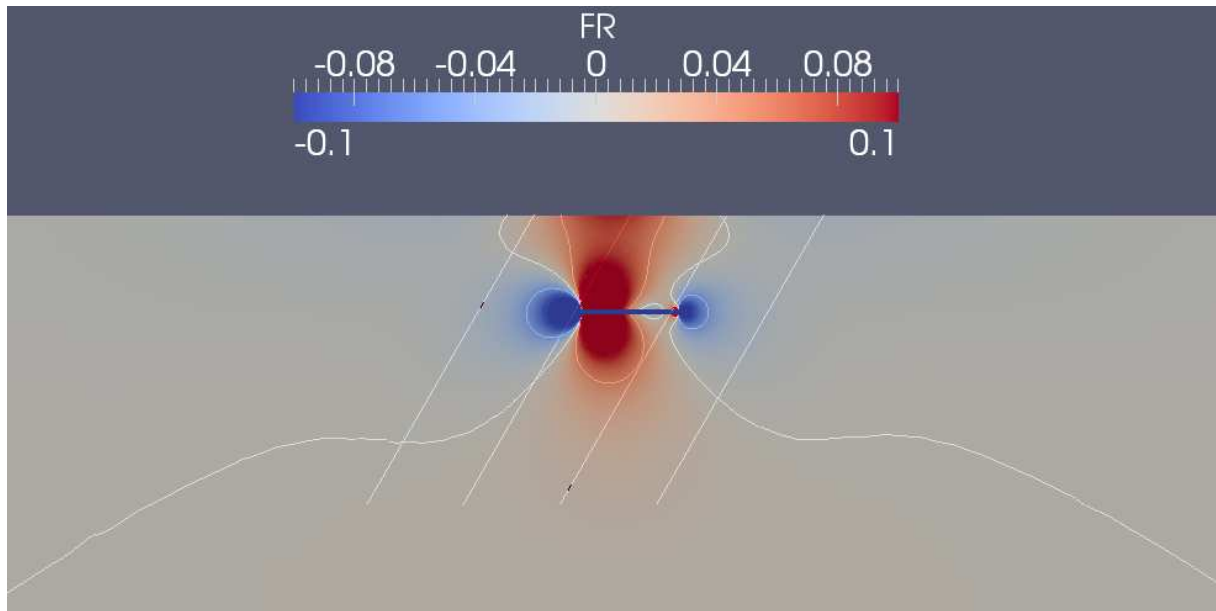


Figure 5.23: λ_{FR} for long times of unitary production at dimensionless time of $t_D = 0.2$. Bottom) Near offset fault planes. Well location at offset -0.4 .



Figures 5.20, 5.22 show that for initial times, null contour lies on the center of production,

faults near the reservoir well location have a tendency to reactivate in time. If the well location is near the reservoir flanks, the fault in this side increases its risk of reactivation since the production and stress changes are larger for this region in comparison to the opposite side.

To define which faults reactivate using $\Delta CFS_t = 0.1$ MPa, Table 5.3 is used to calculate the diffusivity $c = 0.269757$ m²/s and the excess pore pressure reference value for a source line of length $L_{line} = 1000.0$ m, $P_0^{ex} = \frac{q}{\rho_f \frac{\kappa}{\eta} L_{line}} = -0.125$ MPa. In terms of $\lambda_{FRt} = \frac{\Delta CFS_t}{P_0^{ex}} = -0.8$ MPa, this is the dimensionless threshold used to compare LPA computations based on Table 2.1.

Table 5.3: Model parameters for one well production scheme. SI units.

q [$\frac{kg}{s}$]	ρ_{fluid} [$\frac{kg}{m^3}$]	λ_u [Pa]	λ [Pa]	μ [Pa]	α	R_D [m]	$\frac{\kappa}{\eta}$ [$\frac{m^2}{Pa \cdot s}$]	P_0^{ex} [Pa]
-10.0	800.0	$10.0 \cdot 10^9$	$8.1 \cdot 10^9$	$5.4 \cdot 10^9$	0.8	$3 \cdot 10^3$	$1.0 \cdot 10^{-10}$	$\frac{q}{\rho_f \frac{\kappa}{\eta} L_{line}}$

Table 5.3 represents one specific situation for one well with rate of 1080 m³/d, perforated at a depth of 3075 m and producing oil with $\eta = 0.001$ Pa s from reservoir with thickness 150 m, reservoir extension 3000 m and average permeability $\kappa = 1.0 \cdot 10^{-13}$ m². This situation illustrates how it is possible to use the results for one production well at different rates with different λ_{FRt} values. For $\lambda_{FRt} = -0.8$ previous results can be interpreted as follows:

- Figure 5.20 shows that for far and near offset faults, despite having values with a negative trend, faults have a null tendency to reactivate at dimensionless time $t_D = 0.06$ after 23 d of constant production.
- Figure 5.21 shows that the fault at offset 0 does not reach the critical value of $t_D = 0.09$ (after 35 d), at depths equivalent to reservoir flanks. The fault at offset 1 reach the critical value of $t_D = 0.09$ (after 35 d).

When the rate is twice large, the threshold value turns to $\lambda_{FRt} = -0.4$, the scenario is different for 23 d of production and there is a strong tendency to reactivate the fault at offset 0.

In the case of the production well on the left flank under the same operating conditions, results can be interpreted as follows:

- Figure 5.22 shows that for far and near offset faults, despite having negative values, faults have a null tendency to reactivate at dimensionless time $t_D = 0.06$ after 23 d of constant production. Note that for fault at offset 0, the effect of production on the left side is relevant.

- Figure 5.23 shows that the fault at offset 1 reaches the critical value for $t_D = 0.2$ (after 77 d) of constant production.

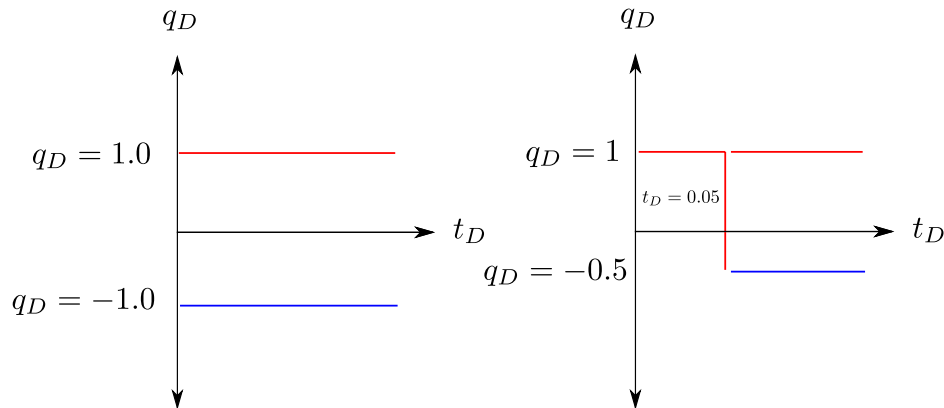
Thus it is possible to do a parametric analysis with these simulation results for different reservoir depths, permeabilities, fluid viscosities and well rates, as well as bhp pressures by setting this condition for line sources, since all these calculations are given in dimensionless forms. This explains, why despite linear poroelastic problem being well know, the use of dimensionless forms exploits poroelastic computations for simple problems in isotropic and homogeneous materials, obtained by solving one specific problem (“master problem”). Thus, it is possible to obtain different solutions with simple post-processing computations.

5.2.2 Reservoir depletion due to injection-production scheme

In this section, fault reactivation is analyzed in two cases when injection and production exist, at the same time, as shown in Figure 5.24.

- The first case is a simple unitary injection/production array on the left and right reservoir flanks respectively.
- In second case, the reservoir is depleted by single production well during 0.05 units of t_D , after this time, two injection wells on reservoir lateral flanks start the injection to maintain the reservoir pressure with one half of unitary rate (*i.e.* $q_D = -0.5$).

Figure 5.24: Production strategy to analyze the effect of depletion. Left) case 1. Right) case 2.



Case 1

Two mass sources at unitary rate $q_D = \pm 1.0$ (injection - production) with normal faulting regime. The situation represented by Table 5.4 ($c = 0.0269757 \text{ m}^2/\text{s}$, using $L_{line} = \text{km}$, the result is $\lambda_{FR} = -0.8$) is critic when the velocity has positive x axis direction (left-right direction). The fault at offset 1 for time $t_D = 0.01$ (*e.g.* 38 d) has a strong tendency because the production induces rock contraction and favors reactivation (see Figure 5.26 (Top)). If this flow occurs in the opposite direction negative x axis direction, the fault at offset 1 has a tendency to reactivate for constant injection twice as large, *i.e.* $\lambda_{FR} = -0.4$ (invert sign of λ_{FR}) at $t_D = 0.02$ (*e.g.* 77 d) (see Figure 5.26 (Bottom)).

Table 5.4: Model parameters for injection/production scheme. SI units.

$q \left[\frac{kg}{s} \right]$	$\rho_{fluid} \left[\frac{kg}{m^3} \right]$	$\lambda_u [Pa]$	$\lambda [Pa]$	$\mu [Pa]$	α	$R_D [m]$	$\frac{\kappa}{\eta} \left[\frac{m^2}{Pa \cdot s} \right]$	$P_0^{ex} [Pa]$
-10.0	800.0	$10.0 \cdot 10^9$	$8.1 \cdot 10^9$	$5.4 \cdot 10^9$	0.8	$3 \cdot 10^3$	$1.0 \cdot 10^{-11}$	$\frac{q}{\rho_f \frac{\kappa}{\eta} L_{line}}$

The fault at offset 0 after $t_D = 0.5$ (*i.e.* 5 years) does not attain the limit (see Figure 5.27 (Top)). However, for opposite flow direction, in the negative x axis direction, this fault reactivates for $t_D = 0.08$ (*e.g.* 308 d) (see Figure 5.27 (Bottom)) when the production rate is twice the one in table 5.4 (invert the sign of λ_{FR}).

Case 2

In this case, injection at reservoir flanks to maintain reservoir pressure is analyzed. Using the rate of production in Table 5.5, $c = 0.0269757 \text{ m}^2/\text{s}$, $L_{line} = 10 \text{ km}$, and the corresponding threshold value is $\lambda_{FR} = -0.4$. Figure 5.28 and 5.29 (Top) show that for time $t_D = 0.08$ (*i.e.* 308 d) fault at offset 1 is near to reactivation, since after $t_D = 0.09$ (*i.e.* 346 d) or 38 d of constant injection in flanks (see Figure 5.28 and 5.29 (Bottom)). The fault begins to stabilize, since injection expands the rock in favor of positive values of λ_{FR} .

Table 5.5: Model parameters for injection on flanks and production on middle region. SI units.

$q \left[\frac{kg}{s} \right]$	$\rho_{fluid} \left[\frac{kg}{m^3} \right]$	$\lambda_u [Pa]$	$\lambda [Pa]$	$\mu [Pa]$	α	$R_D [m]$	$\frac{\kappa}{\eta} \left[\frac{m^2}{Pa \cdot s} \right]$	$P_0^{ex} [Pa]$
-20.0	800.0	$10.0 \cdot 10^9$	$8.1 \cdot 10^9$	$5.4 \cdot 10^9$	0.8	$3 \cdot 10^3$	$1.0 \cdot 10^{-11}$	$\frac{q}{\rho_f \frac{\kappa}{\eta} L_{line}}$

Figure 5.25: λ_{FR} contours at different dimensionless times. Top) $t_D = 0.01$. Bottom) $t_D = 0.02$.

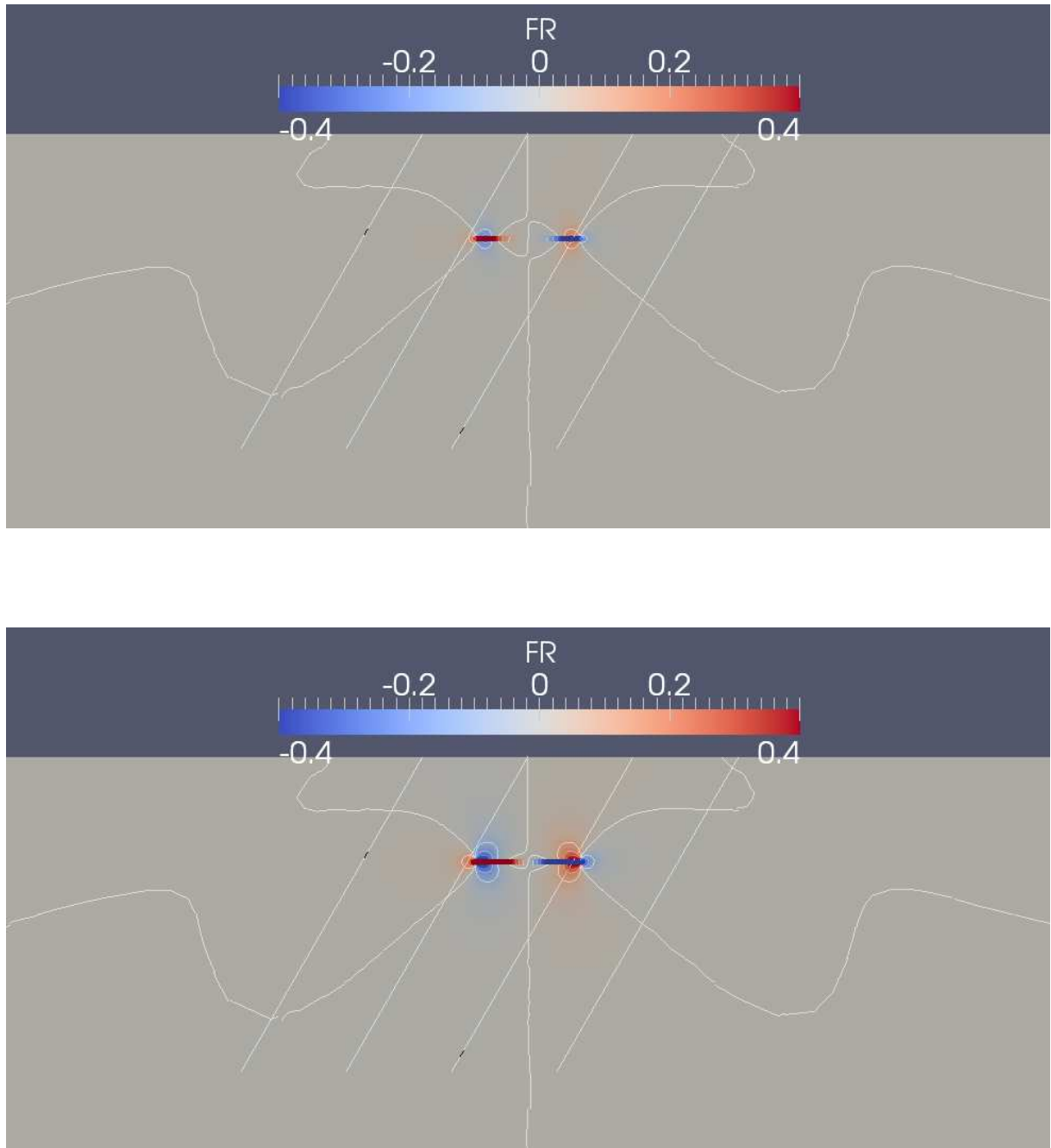


Figure 5.26: λ_{FR} for near offset faults at different dimensionless times. Top) $t_D = 0.01$. Bottom) $t_D = 0.02$.

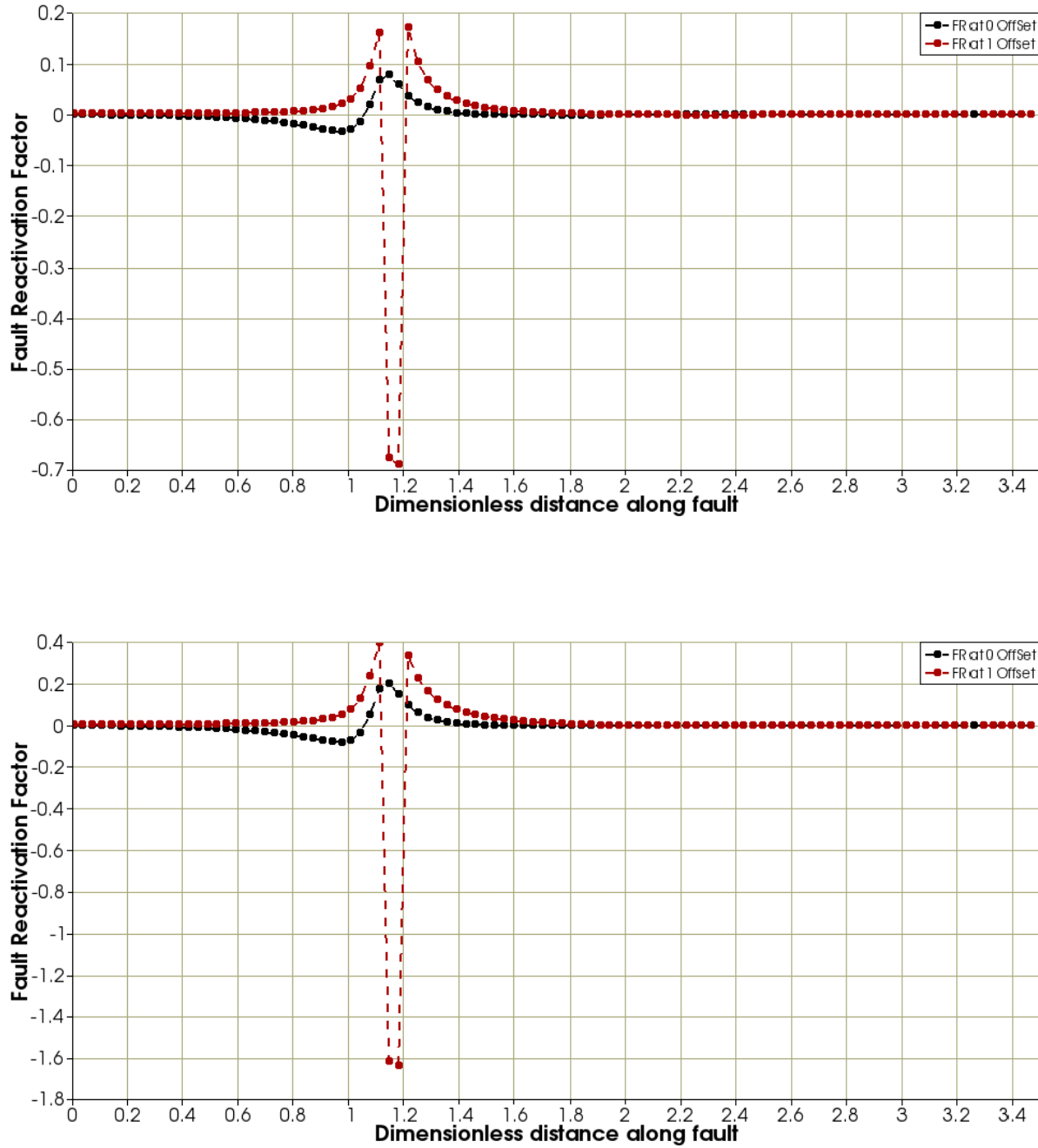


Figure 5.27: λ_{FR} for fault at offset 0 at different dimensionless times. Top) $t_D = 0.5$. Bottom) $t_D = 0.08$.

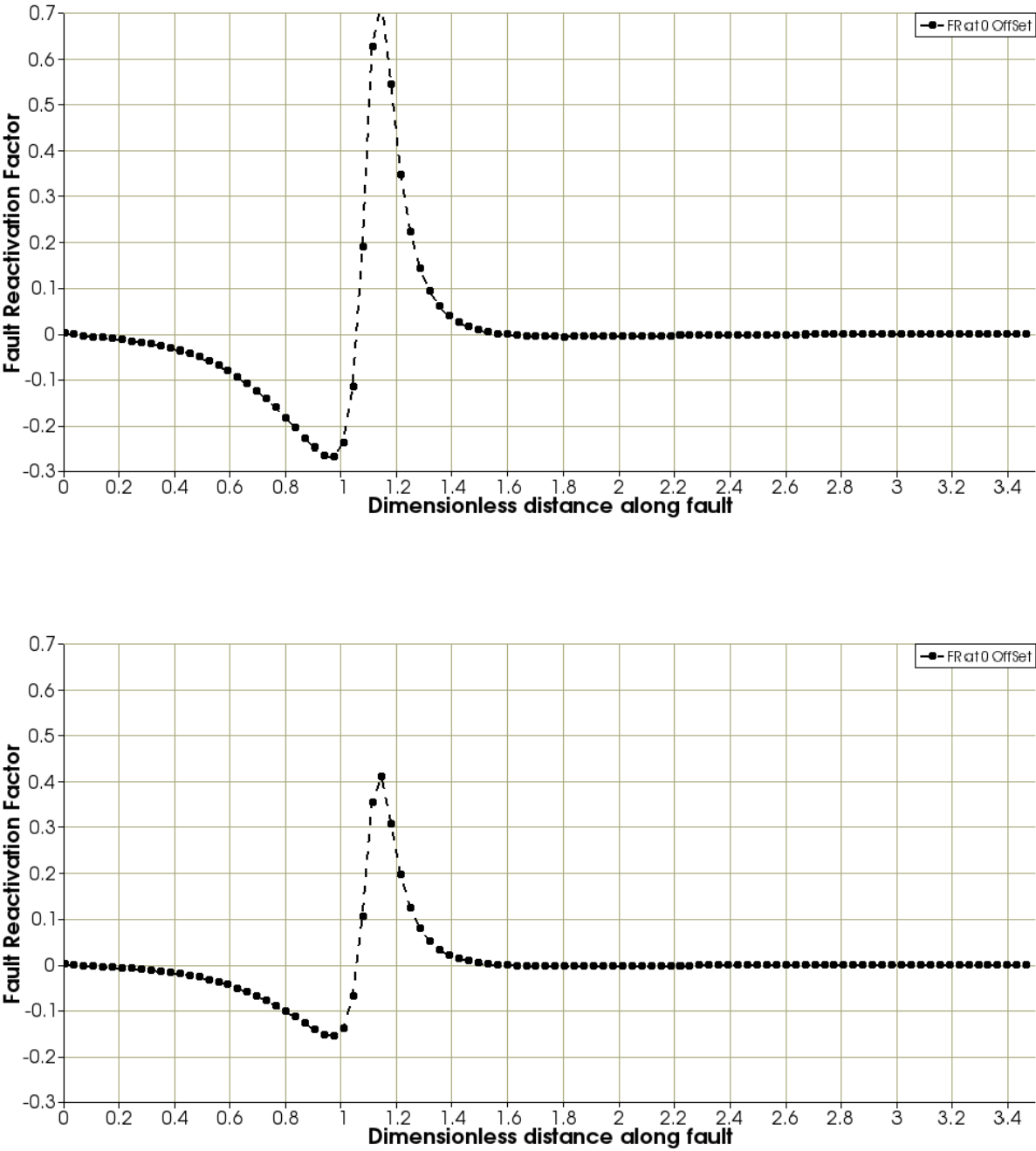


Figure 5.28: $\lambda_{FR} = -0.4$ contour at different dimensionless times. Top) $t_D = 0.08$. Bottom) $t_D = 0.09$.

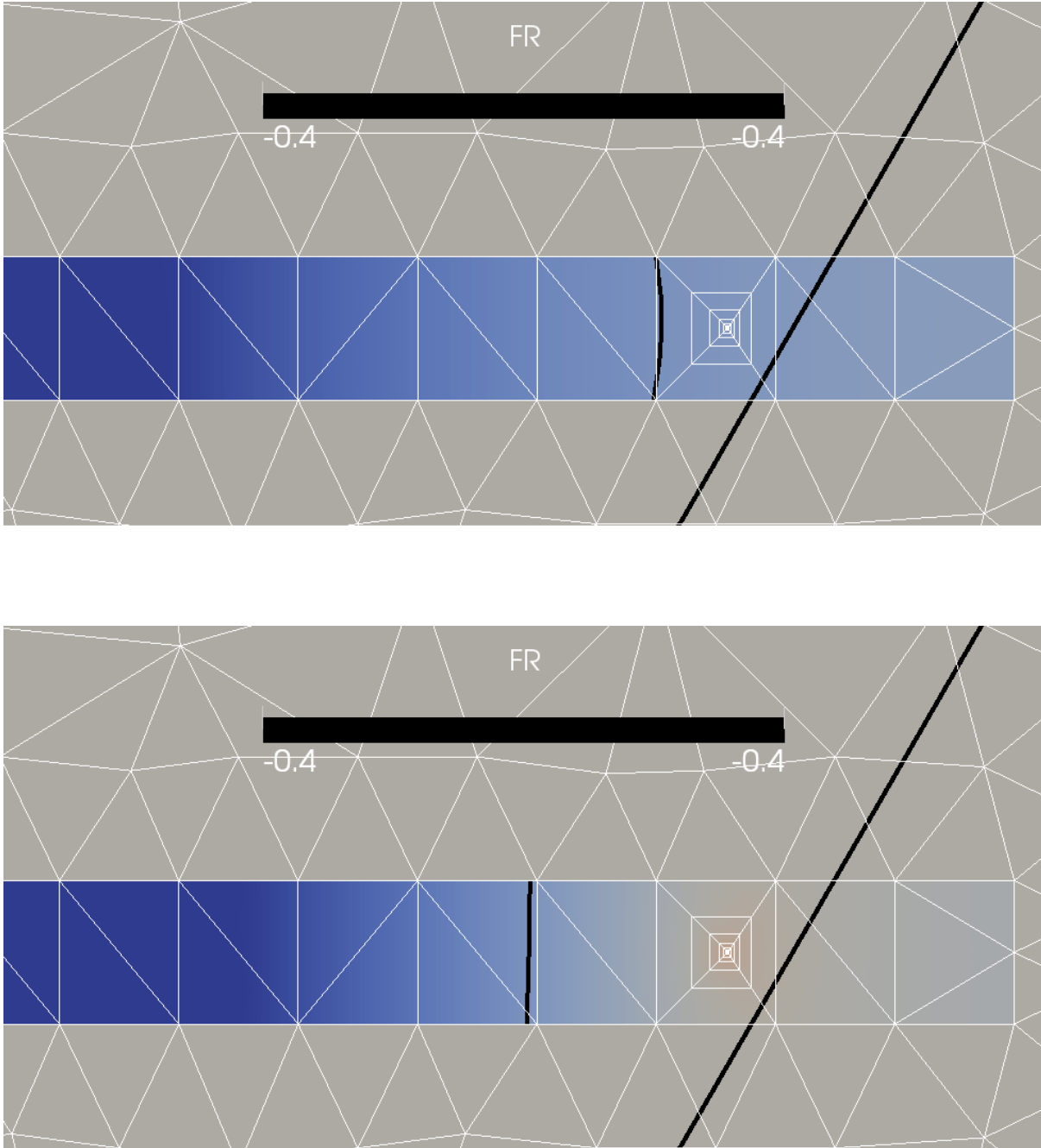
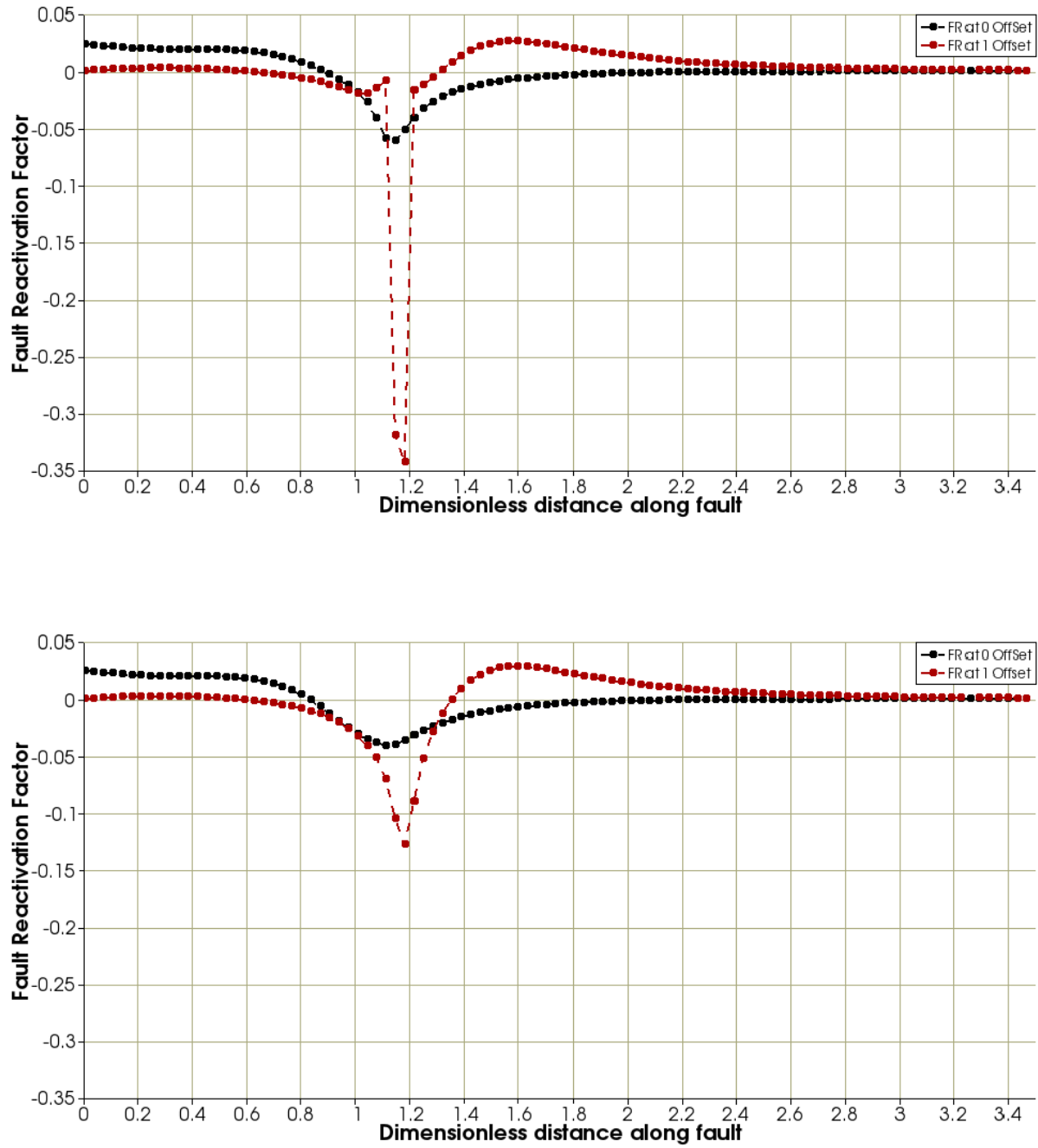


Figure 5.29: λ_{FR} for near offset faults at different dimensionless times. Top) $t_D = 0.08$. Bottom) $t_D = 0.09$.



5.3 Summary

Fault instability due to uniform depletion of a reservoir and due to various non-uniform depletion strategies has been analyzed by conducting an extensive parametric analysis using dimensionless LPA calculations. Computations have been compacted in charts for different reservoir geometries and depths using dimensionless parameters. Also, several interesting effects on fault stability were shown according to the literature.

6. Discussion

6.1 Main results

An implementation for fault reactivation analysis based on Biot's linear poroelasticity of cross-sections in half-space, under plane strain conditions, has been developed. LPA takes into account both traction and displacement continuity between the reservoir sides. The developed code allows considering the reservoir to have rather arbitrary shapes and non-uniform pressure distribution inside the reservoir by modeling diffusive mono-phasic flow, and different material properties of the reservoir and the surrounding medium. Using this program, redistributed stresses around a depleted, homogeneous reservoir with non-uniform pressure distribution have been calculated and the fault instability due to reservoir depletion has been analyzed.

6.2 Conclusions

From this work, it can be concluded that:

- Using numerical modeling it was corroborated that fault reactivation potential is dependent on reservoir geometry, dip angle, reservoir shape and material contrast. Hence, it is very important to consider the real reservoir geometry in the analysis of induced fault reactivation.
- Different reservoir depletion strategies affect the fault stability differently. Pore pressure gradients inside the reservoir have a greater tendency to reactivate and induce slip of the nearby faults. Direction of depletion is an important consideration in evaluating the fault zones prone to slip.
- The Coulomb failure stress change methodology is appropriate for settings where faults are relatively close to their frictional limits (*e.g.*, recently or currently active fold and thrust belts; recently or actively subsiding basins). However, in an absolute

sense, a positive ΔCFS value will not necessarily result in a significant risk of fault reactivation in settings where the shear stresses on existing faults are relatively low.

- In literature, it is common to find numerical hydromechanics models that not consider an reasonable side burden rocks size. In order to avoid boundary effects a series of computations are presented in charts to model regions near or far of reservoir domains with acceptable accuracy.
- An implementation using NeoPZ environment was developed. It can be used to analyse fault reactivation tendency by means of linear poroelasticity equations using or not dimensionless calculations. Dimensionless calculations allow LPA calculated thermoelastic problems in structural analysis. Also, a 3D extension of this computational implementation is trivial since it was developed in a generic environment to develop finite element programs.
- During the development of this work, several multiphysics classes in NeoPZ environment were created and their corresponding validation for linear poroelastic monophasic flow is shown in this dissertation. LPA computations compared several analytic and semi-analytic solutions presented in literature and the commercial software STARS.
- The fault reactivation analysis presented in this work applies to multiphase flow models since the pressure coupling of the equations is given for an average of the partial pressure of each phase, when linear poroelasticity is assumed.
- NeoPZ environment allows the quick development of complex finite element programs since it uses the paradigm of Object Oriented Programming.

6.3 Recommendations for future work

The developed approach provides a basis for a robust reservoir simulation accounting for the poroelastic effects on geologic faults. The following modifications/additions to this model are recommended for future work:

- Several LPA characteristics were not presented in this dissertation; modeling no conductive faults, modeling several reservoir with heterogeneous formations. Hence, it is recommended to evaluate these characteristics.
- LPA has not been adequately tested by back-analyzing case histories of production and injection-induced fault slip.

- Extension to three dimensions, multiphase flow and permeability-stress coupling.
- Model the mechanical interaction between fault blocks and the depleting reservoir, as well modeling fault slip to obtain a more accurate estimate of fault onset and slip. This implies non linear analyses.
- The current model assumes completely reversible, elastic rock mass response to both depletion and injection. However, especially in poorly consolidated rocks, the stress-strain response during compression can be very different from the response in extension. This implies the use of nonlinear models.

Bibliography

- M.A Addis. The influence of the reservoir stress-depletion response on the lifetime considerations of well completion design. *SPE/ISRM Rock Mechanics in Petroleum Engineering*, 1:9, 1998. doi: 10.2118/47289-MS.
- J. Bear. *Dynamics of fluids in porous media*. Number v. 1 in Environmental science series. American Elsevier Pub. Co., 1972. ISBN 9780444001146. URL <http://books.google.com.br/books?id=yrU-AQAAIAAJ>.
- M. A. Biot. General theory of three-dimensional consolidation. *Journal of Applied Physics*, 12(2):155–164, 1941. URL <http://link.aip.org/link/JAPIAU/v12/i2/p155/s1&Agg=doi>.
- John R. Booker. Time dependent strain following faulting of a porous medium. *Journal of Geophys Research*, 79(14):2037–2044, April 1974. doi: 10.1029/JB079i014p02037.
- M. Brezzi, F.; Fortin. *Mixed and hybrid finite elements methods*. Springer series in computational mathematics. Springer-Verlag, 1991. ISBN 9780387975825. URL <http://books.google.com.br/books?id=yYwZAQAAIAAJ>.
- M. P. Cleary. Fundamental solutions for a fluid saturated porous solid. *Journal of solids structures*, 13:785–806, 1977.
- M. P. Cleary. Rate and structure sensitivity in hydraulic fracturing of fluid-saturated porous formations. *20th U.S. Symposium on Rock Mechanics (USRMS)*, 1:16, June 1979. doi: 79-0127.
- H.D.C. Detournay, E.; Alexander. *Fundamentals of Poroelasticity*, volume 2. Pergamon Press, 1993.
- P. Devloo. Systematic and generic construction of shape functions for p-adaptive meshes of multidimensional finite elements. *Computer Methods in Applied Mechanics and Engineering*, 198:21–26, May 2009.

- Turgay Ertekin. *Basic Applied Reservoir Simulation*, volume 7 ISBN: of *SPE Textbook Series*. Society of Petroleum Engineers, Department of Mathematics Carnegie-Mellon University Pittsburgh, Pennsylvania, 2001. ISBN 978-1-55563-089-8.
- J. D. Eshelby. The determination of the elastic field of an ellipsoidal inclusion, and related problems. *Proceedings of the Royal Society of London. Series A, Mathematical and Physical Sciences*, 241(1226):pp. 376–396, 1957. ISSN 00804630. URL <http://www.jstor.org/stable/100095>.
- R. Feignier. Seismicity induced by gas production: I. correlation of focal mechanisms and dome structure. *pure and applied geophysics*, 134:405–426, 1990. ISSN 0033-4553. doi: 10.1007/BF00878740. URL <http://dx.doi.org/10.1007/BF00878740>.
- M. Ferronato. Numerical modelling of regional faults in land subsidence prediction above gas/oil reservoirs. *International Journal for Numerical and Analytical Methods in Geomechanics*, 32(6):633–657, 2008. ISSN 1096-9853. doi: 10.1002/nag.640. URL <http://dx.doi.org/10.1002/nag.640>.
- A. N. Galybin. Model of induced seismicity caused by water injection. *SPE/ISRM Rock Mechanics in Petroleum Engineering, 8-10 July 1998, Trondheim, Norway*, 1: 8, 1998. doi: 10.2118/47253-MS. URL <http://www.onepetro.org/mslib/servlet/onepetropreview?id=00047253>.
- J. Geertsma. The effect of fluid pressure decline on volumetric changes of porous rocks. *Published in Petroleum Transactions - AIME*, 210:331–340, 1957.
- J. Geertsma. Problems of rock mechanics in petroleum production engineering. *International Society for Rock Mechanics*, 1:10, 1966. URL <http://www.onepetro.org/mslib/servlet/onepetropreview?id=ISRM-1CONGRESS-1966-099>.
- L. N. Germanovich. Fault stability inside and near a depleting petroleum reservoir. *American Rock Mechanics Association*, 90:12, 2004.
- RidhaB.C. Gharbi. Dimensionally scaled miscible displacements in heterogeneous permeable media. *Transport in Porous Media*, 48:271–290, 2002. ISSN 0169-3913. doi: 10.1023/A:1015723329598. URL <http://dx.doi.org/10.1023/A%3A1015723329598>.
- J.R. Grasso. Mechanics of seismic instabilities induced by the recovery of hydrocarbons. *pure and applied geophysics*, 139:507–534, 1992. ISSN 0033-4553. doi: 10.1007/BF00879949. URL <http://dx.doi.org/10.1007/BF00879949>.
- Michael D. Greenberg. *Foundations of applied mathematics*. Prentice Hall, 1978. ISBN 0-13-329623-7.

- M.E. Gurtin. Variational principles for linear elastodynamics. *Archive for Rational Mechanics and Analysis*, 16:34–50, 1964. ISSN 0003-9527. doi: 10.1007/BF00248489. URL <http://dx.doi.org/10.1007/BF00248489>.
- Morton E. Gurtin. *An introduction to continuum mechanics*. Number 158 in Mathematics in Science and Engineering. Academic Press inc., Department of Mathematics Carnegie-Mellon University Pittsburgh, Pennsylvania, 1981. ISBN 0-12-309750-9.
- F. Guyoton and P. Volant. Interrelation between induced seismic instabilities and complex geological structure. *Geophysical Research Letters*, 19(7):705–708, 1992. ISSN 1944-8007. doi: 10.1029/92GL00359. URL <http://dx.doi.org/10.1029/92GL00359>.
- C. D. Hawkes. Assessing fault reactivation tendency within and surrounding porous reservoirs during fluid production or injection. *International Journal of Rock Mechanics and Mining Sciences*, 46(1):1 – 7, 2009. ISSN 1365-1609. doi: 10.1016/j.ijrmms.2008.03.008. URL <http://www.sciencedirect.com/science/article/pii/S1365160908000610>.
- Johannes B. Altmann. Tobias M. Müller. Birgit I.R. Müller. Mark R.P. Tingay. Oliver Heidbach. Poroelastic contribution to the reservoir stress path. *International Journal of Rock Mechanics and Mining Sciences*, 47(7):1104–1113, 2010. ISSN 1365-1609. doi: 10.1016/j.ijrmms.2010.08.001. URL <http://www.sciencedirect.com/science/article/pii/S136516091000136X>.
- P. Hsieh and J.D. Bredehoeft. A reservoir analysis of the denver earthquakes: A case of induced seismicity. *Journal of Geophysical Research: Solid Earth*, 86(B2):903–920, 1981. ISSN 2156-2202. doi: 10.1029/JB086iB02p00903. URL <http://dx.doi.org/10.1029/JB086iB02p00903>.
- A. N. Hubbert. Role of fluid pressure in mechanics of overthrust faulting. *Geological Society of America and Hubbert*, 1:91, 1959.
- D. S. Hughes. The effect of pressure on the reduction of pore volume of consolidated sandstones. *Geophysics*, 18:298, 1953.
- C. T. Hwang. On solutions of plane strain consolidation problems by finite element methods. *Canadian Geotechnical Journal*, 8(1):109–118, 1971. doi: 10.1139/t71-009. URL <http://www.nrcresearchpress.com/doi/abs/10.1139/t71-009>.
- C E Jacob. On the flow of water in an elastic artesian aquifer. *EOS Transactions of the American Geophysical Union*, 21:574–586, 1940. URL <http://dspace.sunyconnect.suny.edu/handle/1951/46300>.

- J. Korsawe and G. Starke. Finite element analysis of poro-elastic consolidation in porous media: Standard and mixed approaches. *Computer Methods in Applied Mechanics and Engineering*, 195(9–12):1096 – 1115, 2006. ISSN 0045-7825. doi: 10.1016/j.cma.2005.04.011. URL <http://www.sciencedirect.com/science/article/pii/S0045782505001532>.
- D. Kosloff and R.F. Scott. Finite element simulation of wilmington oil field subsidence: I. linear modelling. *Tectonophysics*, 65(3–4):339 – 368, 1980. ISSN 0040-1951. doi: 10.1016/0040-1951(80)90082-7. URL <http://www.sciencedirect.com/science/article/pii/0040195180900827>.
- F. Lahaie and E. Boyer. Production as a tool to control the efficiency of reservoir fracturing: The lacq case- study. *SPE/ISRM Rock Mechanics in Petroleum Engineering, 8-10 July 1998, Trondheim, Norway*, 1:8, 1998. doi: 10.2118/47318-MS. URL <http://www.onepetro.org/mslib/servlet/onepetropreview?id=00047318>.
- L.W. Lake. Scaling fluid flow through heterogeneous permeable media. *SPE Advanced Technology Series*, 3:525–536, 1990. doi: 10.2118/26648-PA. URL <http://www.onepetro.org/mslib/servlet/onepetropreview?id=00026648>.
- B. Maillot. Numerical simulation of seismicity due to fluid injection in a brittle poroelastic medium. *International Journal of Geophysics*, 1:10, 1999.
- N. Morita. Rock-property changes during reservoir compaction. *SPE Formation Evaluation (Society of Petroleum Engineers)*, 7:197–205, 1992. doi: 10.2118/13099-PA. URL <http://www.onepetro.org/mslib/servlet/onepetropreview?id=00013099>.
- T. Mura. *Micromechanics of Defects in Solids*. Monographs and textbooks on mechanics of solids and fluids: Mechanics of elastic and inelastic solids. Martinus Nijhoff, 1982. ISBN 9789024730056. URL <http://books.google.com.br/books?id=3l6dQgAACAAJ>.
- Craig. Nicholson and RobertL. Wesson. Triggered earthquakes and deep well activities. *pure and applied geophysics*, 139:561–578, 1992. ISSN 0033-4553. doi: 10.1007/BF00879951. URL <http://dx.doi.org/10.1007/BF00879951>.
- J. G. Osorio. Fully coupled fluid-flow and geomechanics simulation of stress-sensitive reservoirs. *Reservoir Simulation Symposium*, SPE 38023:7, 1992. doi: 10.2118/38023-MS. URL <http://www.onepetro.org/mslib/servlet/onepetropreview?id=00038023>.
- W. E. Pratt. Local subsidence of the goose creek oil field. *The Journal of Geology*, 34(7): 577–590, 1926.

- A. Rejeb. Mathematical simulations of coupled {THM} processes of fanay-augères field test by distinct element and discrete finite element methods. In Lanru Jing Ove Stephansson and Chin-Fu Tsang, editors, *Coupled Thermo-Hydro-Mechanical Processes of Fractured Media Mathematical and Experimental Studies*, volume 79 of *Developments in Geotechnical Engineering*, pages 341 – 368. Elsevier, 1996. doi: 10.1016/S0165-1250(96)80032-0. URL <http://www.sciencedirect.com/science/article/pii/S0165125096800320>.
- J. R. Rice. Some basic stress diffusion solutions for fluid-saturated elastic porous media with compressible constituents. *Reviews of Geophysics*, 14(2):227–241, 1976. ISSN 1944-9208. doi: 10.1029/RG014i002p00227. URL <http://dx.doi.org/10.1029/RG014i002p00227>.
- J.P.A Roest. Geomechanical analysis of small earthquakes at the eleveld gas reservoir. *Rock Mechanics in Petroleum Engineering*, 1:8, 1994. doi: 10.2118/28097-MS. URL <http://www.onepetro.org/mslib/servlet/onepetropreview?id=00028097>.
- J. W. Rudnicki. Fluid mass sources and point forces in linear elastic diffusive solids. *Journal of Mechanics of Materials*, 5:383–393, 1986.
- J. W. Rudnicki. Alteration of regional stress by reservoirs and other inhomogeneities: stabilizing or destabilizing? *International Congress on Rock Mechanics*, 3:1629– 1637, 1999.
- R. S. Sandhu. Numerical performance of some finite element schemes for analysis of seepage in porous elastic media. *International Journal for Numerical and Analytical Methods in Geomechanics*, 1(2):177–194, 1977. ISSN 1096-9853. doi: 10.1002/nag.1610010205. URL <http://dx.doi.org/10.1002/nag.1610010205>.
- P. Segall. Stress and subsidence resulting from subsurface fluid withdrawal in the epicentral region of the 1983 coalinga earthquake. *Journal of geophysical research*, 90:6801, 1987.
- P. Segall. Poroelastic stressing and induced seismicity near the Lacq gas field, southwestern France. *J. Geophys. Res.*, 99:15423–15438, 1994.
- Paul Segall. Induced stresses due to fluid extraction from axisymmetric reservoirs. *pure and applied geophysics*, 139:535–560, 1992. ISSN 0033-4553. doi: 10.1007/BF00879950. URL <http://dx.doi.org/10.1007/BF00879950>.
- K. Terzaghi. *Theoretical soil mechanics*. J. Wiley and Sons, inc., 1943. URL http://books.google.com.br/books?id=7_ogAAAAMAAJ.

- L. W. Teufel. Effect of reservoir depletion and pore pressure drawdown on in situ stress and deformation in the ekofisk field, north sea. *American Rock Mechanics Association*, 1:10, 1991. URL <http://www.onepetro.org/mslib/servlet/onepetropreview?id=ARMA-91-063>.
- P. A. Vermeer and A. Verruijt. An accuracy condition for consolidation by finite elements. *International Journal for Numerical and Analytical Methods in Geomechanics*, 5(1):1–14, 1981. ISSN 1096-9853. doi: 10.1002/nag.1610050103. URL <http://dx.doi.org/10.1002/nag.1610050103>.
- H. F. Wang. *Theory of linear poroelasticity: with applications to geomechanics and hydrogeology*. Number II in Princeton seires in geophysics. Princeton University Press, 2000. ISBN 0-691-037469.
- E. L. Wilson. Flow of compressible fluid in porous elastic media. *International Journal for Numerical Methods in Engineering*, 5(3):419–442, 1973. ISSN 1097-0207. doi: 10.1002/nme.1620050311. URL <http://dx.doi.org/10.1002/nme.1620050311>.
- S.M. Calisal; H.L. Wong. Computerized, interactive calculation of dimensionless variables. *Computers & Education*, 14(6):525 – 536, 1990. ISSN 0360-1315. doi: 10.1016/0360-1315(90)90111-J. URL <http://www.sciencedirect.com/science/article/pii/036013159090111J>.
- L. R. Wynne. *The finite element method in the static and dynamics deformation and consolidation of porous media*. John Wiley, second edition, 2000. ISBN 0-471-92809-7.
- M. D. Zoback and H.P. Harjes. Injection-induced earthquakes and crustal stress at 9 km depth at the ktb deep drilling site. *Journal of Geophysical Research: Solid Earth*, 102:18477–18491, January 1997. doi: 10.1029/96JB02814.

A. Dimensionless forms

A.1 Computation of dimensionless forms

Based on the proof of the *Buckingham* π theorem and the homogeneity theorem Wong (1990) gives the matrix relationships:

$$S_{par} = R_{par}P_{par} \quad (A.1)$$

where S_{par} is the secondary variable matrix, P_{par} is the principal variable matrix, R_{par} is the relationship matrix that contains the dimensionless groups by choosing P_{par} and S_{par} , from the complete set of parameter involved in the problem. R_{par} is computed as in Wong (1990) using:

$$R_{par} = S_{par}P_{par}^{-1} \quad (A.2)$$

the dimensionless form of the equations in question are obtained by inserting the dimensionless groups calculated in the original expressions.

Step load direct dimensionless formulation

The analysis is based on length [m], mass [Kg] and time [s] as fundamental units. The object of this part is to determine from the next set of variables the corresponding dimensionless form of the equations given by Wang (2000) for Semi-infinite column problem.

- $cm \left[\frac{m \cdot Kg}{s^2} \right]$: Geertsma uniaxial poroelastic expansion coefficient.
- $P^\circ = P_o \left[\frac{s^2}{m \cdot Kg} \right]$: The initial pressure excess as reference pressure.
- $c \left[\frac{m^2}{s} \right]$: The hydraulic diffusivity.
- $L [m]$: Domain max dimension.
- $P \left[\frac{s^2}{m \cdot Kg} \right]$: The initial pressure excess as reference pressure.

- z [m] : The column depth as positive value.
- \mathbf{u}_z [m] : Z-direction displacement.
- t [s] : Time.

The parameters matrix \mathbf{MP} , \mathbf{P} (independent parameters) and \mathbf{S} (dependent parameters) matrices are defined as

Table A.1: Step Load one dimensional consolidation matrices. \mathbf{MP} matrix of rank 3, \mathbf{P} , \mathbf{S} set of principal and secondary variables.

\mathbf{MP}	[m]	[Kg]	[s]
cm	1	-1	2
P_o	-1	1	-2
c	2	0	-1
L	1	0	0
P	-1	1	-2
z	1	0	0
\mathbf{u}_z	1	0	0
t	0	0	1

\mathbf{P}	[m]	[Kg]	[s]
P_o	-1	1	-2
c	2	0	-1
L	1	0	0

\mathbf{S}	[m]	[Kg]	[s]
P	-1	1	-2
z	1	0	0
\mathbf{u}_z	1	0	0
t	0	0	1
cm	1	-1	2

The matrix \mathbf{R} is computed as $\mathbf{R} = \mathbf{SP}^{-1}$ Wong (1990) is obtained \mathbf{R} matrix, that contains the relationship between the secondary and dimensionless variables as follow:

Table A.2: Step Load one dimensional consolidation relationship matrix \mathbf{R} and definitions of dimensionless group of variables.

\mathbf{R}	P_o	c	L	Group	Equation
P	1	0	0	P	$P_D P_o$
z	0	0	1	z	$z_D L$
\mathbf{u}_z	0	0	1	\mathbf{u}_z	$\mathbf{u}_{Dz} L$
t	0	-1	2	t	$t_D \frac{L^2}{c}$
cm	-1	0	0	cm	$cm_D \frac{1}{P_o}$

By inserting the expressions of the Table A.2 into original expressions (Wang, 2000), and simplifying dimensionless forms are obtained as:

$$P_D(z_D, t_D) = \text{erf} \left(\frac{z_D}{2\sqrt{t_D}} \right) \quad (\text{A.3})$$

$$\mathbf{u}_{\mathbf{D}z}(z_D, t_D) = cm_D \left(\frac{2 \exp\left(-\frac{z_D^2}{t_D}\right) \sqrt{t_D}}{\sqrt{\pi}} - z_D \operatorname{erf}\left(\frac{z_D}{2\sqrt{t_D}}\right) \right) \quad (\text{A.4})$$

Note that z-direction displacement is redefined as $\mathbf{u}_z = \mathbf{u}_{\mathbf{D}z} Lcm_D = \mathbf{u}_{\mathbf{D}z} LcmP_o$, the material parameters are eliminated from the equations A.3, A.5 that can characterize any group of material parameters.

$$\mathbf{u}_{\mathbf{D}z}(z_D, t_D) = \left(\frac{2 \exp\left(-\frac{z_D^2}{t_D}\right) \sqrt{t_D}}{\sqrt{\pi}} - z_D \operatorname{erf}\left(\frac{z_D}{2\sqrt{t_D}}\right) \right) \quad (\text{A.5})$$

B. Contribute Method

B.1 Poroelastic Contribute Method

Since the matrix problem is associated with a weak statement, the approximation spaces can be changed, but here, CG modeling is used with H^1 Sobolev space with different polynomial orders. Algorithms 1, 2, 3 and 4 calculate the matrices contribution at the element level. All these element contributions are calculated and assembled to obtain the global stiffness matrix, mass matrix and vectors presented in 3.73 and 3.74.

Let's introduce the expanded forms of the matrices and vectors 3.60, 3.61, 3.62, 3.63, 3.65, 3.66 in terms of shape and test functions 3.53, 3.54, 3.55, 3.56, using plain strain conditions, where mathematical operators are expanded in terms of spatial derivatives

Linear strain operator

$$\begin{aligned}
 K_{elasticity} \bar{\mathbf{u}} &= \left[\sum_{i=1}^{nodes} \left(\sum_{j=1}^{nodes} ([K_{ij}]) \right) \right] \bar{\mathbf{u}}_i \\
 [K_{ij}] &= \begin{aligned} &\int_{\Omega} (\lambda_D + 2\mu_D) \frac{\partial \Psi_i^u}{\partial x_D} \frac{\partial \Psi_j^v}{\partial x_D} + \mu_D \frac{\partial \Psi_i^u}{\partial y_D} \frac{\partial \Psi_j^v}{\partial y_D} \partial \Omega & \int_{\Omega} \left(\lambda_D \frac{\partial \Psi_i^u}{\partial x_D} \frac{\partial \Psi_j^v}{\partial y_D} + \mu_D \frac{\partial \Psi_i^u}{\partial y_D} \frac{\partial \Psi_j^v}{\partial x_D} \right) \partial \Omega \\ &\int_{\Omega} \left(\lambda_D \frac{\partial \Psi_i^u}{\partial y_D} \frac{\partial \Psi_j^v}{\partial x_D} + \mu_D \frac{\partial \Psi_i^u}{\partial x_D} \frac{\partial \Psi_j^v}{\partial y_D} \right) \partial \Omega & \int_{\Omega} (\lambda_D + 2\mu_D) \frac{\partial \Psi_i^u}{\partial y_D} \frac{\partial \Psi_j^v}{\partial y_D} + \mu_D \frac{\partial \Psi_i^u}{\partial x_D} \frac{\partial \Psi_j^v}{\partial x_D} \partial \Omega \end{aligned}
 \end{aligned} \tag{B.1}$$

Coupling matrix

$$\begin{aligned}
 Q_c \bar{\mathbf{p}} &= \left[\sum_{i=1}^{nodes} \left(\sum_{j=1}^{nodes} ([Q_{cij}]) \right) \right] \bar{\mathbf{p}}_i \\
 [Q_{cij}] &= \begin{aligned} &\int_{\Omega} \left(-\alpha \Psi_i^P \frac{\partial \Psi_j^v}{\partial x_D} \right) \partial \Omega \\ &\int_{\Omega} \left(-\alpha \Psi_i^P \frac{\partial \Psi_j^v}{\partial x_D} \right) \partial \Omega \end{aligned}
 \end{aligned} \tag{B.2}$$

Force right hand term

$$\begin{aligned}
 F^u &= \sum_{i=1}^{nodes} ([F_i^u]) \\
 F_i^u &= \int_{\Gamma_{Neumann}} (T_x) \cdot \Psi_j^v \partial\Gamma + \int_{\Omega} b_{xD} \cdot \Psi_j^v d\Omega \\
 &\quad \int_{\Gamma_{Neumann}} (T_y) \cdot \Psi_j^v \partial\Gamma + \int_{\Omega} b_{yD} \cdot \Psi_j^v d\Omega
 \end{aligned} \tag{B.3}$$

For diffusion problem

$$\begin{aligned}
 Q_c^T \frac{d\bar{\mathbf{u}}}{dt_D} &= \left[\sum_{i=1}^{nodes} \left(\sum_{j=1}^{nodes} ([Q_{cij}^T]) \right) \right] \frac{d\bar{\mathbf{u}}}{dt_D} \\
 [Q_{cij}^T] &= \int_{\Omega} \left(\alpha \frac{\partial \Psi_i^u}{\partial x_D} \Psi_j^w \right) \partial\Omega \\
 &\quad \int_{\Omega} \left(\alpha \frac{\partial \Psi_i^u}{\partial y_D} \Psi_j^w \right) \partial\Omega
 \end{aligned} \tag{B.4}$$

Compressibility matrix

$$\begin{aligned}
 S \frac{d\bar{\mathbf{p}}}{dt_D} &= \left[\sum_{i=1}^{nodes} \left(\sum_{j=1}^{nodes} ([S_{ij}]) \right) \right] \frac{d\bar{\mathbf{p}}}{dt_D} \\
 [S_{ij}] &= \int_{\Omega} (S_{rD} \Psi_i^P \Psi_j^w) \partial\Omega
 \end{aligned} \tag{B.5}$$

Permeability matrix

$$\begin{aligned}
 H \bar{\mathbf{p}} &= \left[\sum_{i=1}^{nodes} \left(\sum_{j=1}^{nodes} ([H_{ij}]) \right) \right] \bar{\mathbf{p}} \\
 [H_{ij}] &= \int_{\Omega} \left(\frac{\partial \Psi_i^P}{\partial x_D} \frac{\partial \Psi_j^w}{\partial x_D} + \frac{\partial \Psi_i^P}{\partial y_D} \frac{\partial \Psi_j^w}{\partial y_D} \right) \partial\Omega
 \end{aligned} \tag{B.6}$$

Mass right hand term

$$\begin{aligned}
 F^P &= \sum_{i=1}^{nodes} ([F_i^P]) \Delta t_D \\
 F_i^P &= \int_{\Gamma_{Neumann}} (q_{normal}) \cdot \Psi_i^w \partial\Gamma
 \end{aligned} \tag{B.7}$$

Algorithm 1 Q_c matrix implementation.

```

1  // Matrix  $Q_c$ 
2  // Coupling matrix  $Q_c$ 
3   $\sum_{i=1}^{nodes}$ 
4  for(int in = 0; in < phru; in++)
5  {
6      // Derivative calculations for  $\Psi_i^v$ 
7      // Note that  $du(x_D \rightarrow 0, \Psi_i^v \rightarrow 1)$ 
8       $\frac{\partial \Psi_i^v}{\partial x_D}$   $du(0,1) = dphiu(0,jn)*axes(0,0)+dphiu(1,jn)*axes(1,0);$ 
9
10     // Note that  $du(y_D \rightarrow 1, \Psi_i^v \rightarrow 1)$ 
11      $\frac{\partial \Psi_i^v}{\partial y_D}$   $du(1,1) = dphiu(0,jn)*axes(0,1)+dphiu(1,jn)*axes(1,1);$ 
12
13      $\sum_{j=1}^{nodes}$ 
14     for(int jn = 0; jn < phrp; jn++)
15     {
16         //  $[Q_{cij}]_1 = \int_{\Omega} \left( -\alpha \Psi_i^P \frac{\partial \Psi_j^v}{\partial x_D} \right) \partial \Omega$ 
17          $ek(2*in, 2*phru+jn) += (-1.)*falpha*weight*(phip(jn,0)*du(0,1));$ 
18
19         //  $[Q_{cij}]_2 = \int_{\Omega} \left( -\alpha \Psi_i^P \frac{\partial \Psi_j^v}{\partial y_D} \right) \partial \Omega$ 
20
21          $ek(2*in+1, 2*phru+jn) += (-1.)*falpha*weight*(phip(jn,0)*du(1,1));$ 
22     }
23 }

```

Algorithm 2 Q_c^T matrix implementation.

```

1  // Matrix  $Q_c^T$ 
2  // Coupling matrix transpose  $Q_c^T$ 
3   $\sum_{i=1}^{nodes}$ 
4  for(int in = 0; in < phru; in++)
5  {
6      // Derivative calculations for  $\Psi_i^u$ 
7      // Note that  $du(x_D \rightarrow 0, \Psi_i^u \rightarrow 0)$ 
8       $\frac{\partial \Psi_i^u}{\partial x_D}$   $du(0,0) = dphiu(0,in)*axes(0,0)+dphiu(1,in)*axes(1,0);$ 
9
10     // Note that  $du(y_D \rightarrow 1, \Psi_i^u \rightarrow 0)$ 
11      $\frac{\partial \Psi_i^u}{\partial y_D}$   $du(1,0) = dphiu(0,in)*axes(0,1)+dphiu(1,in)*axes(1,1);$ 
12
13      $\sum_{j=1}^{nodes}$ 
14     for(int jn = 0; jn < phrp; jn++)
15     {
16         //  $[Q_{cij}^T]_1 = \int_{\Omega} \left( \alpha \frac{\partial \Psi_i^u}{\partial x_D} \Psi_j^w \right) \partial \Omega$ 
17
18          $ek(2*phru+jn, 2*in) += (-1.)*falpha*weight*du(0,0)*(phip(jn,0));$ 
19
20         //  $[Q_{cij}^T]_2 = \int_{\Omega} \left( \alpha \frac{\partial \Psi_i^u}{\partial y_D} \Psi_j^w \right) \partial \Omega$ 
21
22          $ek(2*phru+jn, 2*in+1) += (-1.)*falpha*weight*du(1,0)*(phip(jn,0));$ 
23     }
24 }

```

Algorithm 3 H matrix implementation.

```

1  // Diffusion Equation
2  // Compresibility and Permeability matrix
3  ΔtD
4  const REAL DeltaT = fTimeStep;
5  ∑i=1nodes
6  for(int in = 0; in < phrp; in++)
7  {
8      // Fp Vector Mass right hand term  $F_i^P$ 
9       $\int_{\Gamma_{Neumann}} (q_{normal}) \cdot \Psi_i^w \partial \Gamma$ 
10     ef(in+2*phru, 0) += weight*Qnormal[2]*phip(in, 0);
11
12     ∑j=1nodes
13     for(int jn = 0; jn < phrp; jn++)
14     {
15         // S Matrix  $S$ 
16         //  $[S_{ij}] = \int_{\Omega} (S_{rD} \Psi_i^P \Psi_j^w) \partial \Omega$ 
17
18         ek(in+2*phru, jn+2*phru) += (-1.0)*weight*fSe*phip(in,0)*phip(jn,0);
19         // H Matrix  $H$ 
20         for(int kd=0; kd<fDim; kd++)
21         {
22             //  $[H_{ij}] = \int_{\Omega} \left( \frac{\partial \Psi_i^P}{\partial x_D} \frac{\partial \Psi_j^w}{\partial x_D} + \frac{\partial \Psi_i^P}{\partial y_D} \frac{\partial \Psi_j^w}{\partial y_D} \right) \partial \Omega$ 
23
24             ek(in+2*phru, jn+2*phru) += (-1.0)*weight*(fk/fvisc)*DeltaT*ftheta*dhip(kd,in)*dhip(kd,jn);
25         }
26     }
27 }

```

Algorithm 4 $K_{elasticity}$ matrix implementation.

```

1  // Elastic equation
2  // Linear strain operator  Kelasticity
3   $\sum_{i=1}^{nodes}$ 
4  for(int in = 0; in < phru; in++)
5  {
6      // Derivative calculations for  $\Psi_i^u$ 
7      // Note that  $du(x_D \rightarrow 0, \Psi_i^u \rightarrow 0)$ 
8       $\frac{\partial \Psi_i^u}{\partial x_D}$     du(0,0) = dphiu(0,in)*axes(0,0)+dphiu(1,in)*axes(1,0);
9
10     // Note that  $du(y_D \rightarrow 1, \Psi_i^u \rightarrow 0)$ 
11      $\frac{\partial \Psi_i^u}{\partial y_D}$     du(1,0) = dphiu(0,in)*axes(0,1)+dphiu(1,in)*axes(1,1);
12
13     // Fu Vector Force right hand term  $F_i^u$ 
14      $\int_{\Gamma_{Neuman}} (T_x) \cdot \Psi_j^v \partial \Gamma$  +  $\int_{\Omega} b_{xD} \cdot \Psi_j^v d\Omega$ 
15     ef(2*in, 0) += weight*fTraction[0]*phiu(in,0) + weight*fb[0]*phiu(in, 0);
16
17      $\int_{\Gamma_{Neuman}} (T_y) \cdot \Psi_j^v \partial \Gamma$  +  $\int_{\Omega} b_{yD} \cdot \Psi_j^v d\Omega$ 
18     ef(2*in+1, 0) += weight*fTraction[1]*phiu(in,0) + weight*fb[1]*phiu(in, 0);
19
20      $\sum_{j=1}^{nodes}$ 
21     for(int jn = 0; jn < phru; jn++)
22     {
23         // Derivative calculations for  $\Psi_i^v$ 
24         // Note that  $du(x_D \rightarrow 0, \Psi_i^v \rightarrow 1)$ 
25          $\frac{\partial \Psi_i^v}{\partial x_D}$     du(0,1) = dphiu(0,jn)*axes(0,0)+dphiu(1,jn)*axes(1,0);
26
27         // Note that  $du(y_D \rightarrow 1, \Psi_i^v \rightarrow 1)$ 
28          $\frac{\partial \Psi_i^v}{\partial y_D}$     du(1,1) = dphiu(0,jn)*axes(0,1)+dphiu(1,jn)*axes(1,1);
29
30         /* Plain Strain State */
31         //  $[K_{ij}]_{11}$  =  $\int_{\Omega} \left( (\lambda_D + 2\mu_D) \frac{\partial \Psi_i^u}{\partial x_D} \frac{\partial \Psi_j^v}{\partial x_D} + \mu_D \frac{\partial \Psi_k^u}{\partial y_D} \frac{\partial \Psi_l^v}{\partial y_D} \right) \partial \Omega$ 
32
33         ek(2*in,2*jn) += weight*((flambda + 2*fmu)*du(0,0)*du(0,1)+(fmu)*du(1,0)*du(1,1));
34
35         //  $[K_{ij}]_{12}$  =  $\int_{\Omega} \left( \lambda_D \frac{\partial \Psi_i^u}{\partial x_D} \frac{\partial \Psi_j^v}{\partial y_D} + \mu_D \frac{\partial \Psi_k^u}{\partial y_D} \frac{\partial \Psi_l^v}{\partial x_D} \right) \partial \Omega$ 
36
37         ek(2*in,2*jn+1) += weight* (flambda*du(0,0)*du(1,1) + (fmu)*du(1,0)*du(0,1));
38
39         //  $[K_{ij}]_{21}$  =  $\int_{\Omega} \left( \lambda_D \frac{\partial \Psi_i^u}{\partial y_D} \frac{\partial \Psi_j^v}{\partial x_D} + \mu_D \frac{\partial \Psi_k^u}{\partial x_D} \frac{\partial \Psi_l^v}{\partial y_D} \right) \partial \Omega$ 
40
41         ek(2*in+1,2*jn) += weight* (flambda*du(1,0)*du(0,1) + (fmu)*du(0,0)*du(1,1));
42
43         //  $[K_{ij}]_{22}$  =  $\int_{\Omega} \left( (\lambda_D + 2\mu_D) \frac{\partial \Psi_i^u}{\partial y_D} \frac{\partial \Psi_j^v}{\partial y_D} + \mu_D \frac{\partial \Psi_k^u}{\partial x_D} \frac{\partial \Psi_l^v}{\partial x_D} \right) \partial \Omega$ 
44
45         ek(2*in+1,2*jn+1) += weight* ((flambda + 2*fmu)*du(1,0)*du(1,1) + (fmu)*du(0,0)*du(0,1));
46     }
47 }

```


C. GID Mat Template

C.1 GID Mat Template

GID template was used in order to associated materials identifiers with the geometric mesh. A extensive documentation for the use of templates can be found in GID web site.

Algorithm 5 Template to generate geometric grids for LPA.

```
1 // Define material domain properties
NUMBER: 1 MATERIAL: DReservoirRock
3 QUESTION: Rock_Density_(kg/m3)
VALUE: 2300.0
5 QUESTION: Fluid_Density_(kg/m3)
VALUE: 1000.0
7 QUESTION: Porosity_ref_(Fraction)
VALUE: 0.3
9 QUESTION: Permeability_(m2)
VALUE: 1.0e-12
11 QUESTION: Fluid_Viscosity_(Pa.s)
VALUE: 0.001
13 QUESTION: First_Lame_(Pa)
VALUE: 8.0e9
15 QUESTION: Second_Lame_(Pa)
VALUE: 5.0e9
17 QUESTION: First_Lame_Undrained_(Pa)
VALUE: 10.0e9
19 QUESTION: Biot_Constant_(none)
VALUE: 0.8
21 QUESTION: Bluid_Group_(none)
VALUE: 1
23 QUESTION: IsPoroelastic_(Flag)
VALUE: 1
25 END MATERIAL
// Define boundary material properties
27 NUMBER: 2 MATERIAL: Contour
QUESTION: Domain_Associated_ID_(IDNumber)
29 VALUE: 0
QUESTION: BC_Type_(BoundaryType)
31 VALUE: 000
QUESTION: Variable1_Value_(Value)
33 VALUE: 0
QUESTION: Variable2_Value_(Value)
35 VALUE: 0
QUESTION: Variable3_Value_(Value)
37 VALUE: 0
QUESTION: Bluid_Group_(none)
39 VALUE: 1
QUESTION: IsPoroelastic_(Flag)
41 VALUE: 1
END MATERIAL
```